UNIVERSITÀ
degli STUDI
di CATANIA

Dipartimento
di Fisica
e Astronomia
"Ettore Majorana"

PH.D. IN PHYSICS

CRISTINA ZAGAMI

THE CHIFAR EXPERIMENT @ LNS: DYNAMICAL AND ISOSPIN EFFECTS IN HEAVY ION COLLISIONS AT 20AMEV STUDIED WITH CHIMERA AND FARCOS

FINAL PROJECT

PH.D. COORDINATOR: PROF. L. LAMIA

TUTORS:
CHIAR.MA PROF.SSA F. RIZZO
DR. E. V. PAGANO

XXXVIII CYCLE: 2023-2025

La mente non ha bisogno, come un vaso,
di essere riempita, ma, come legna da ardere,
ha bisogno solo di una scintilla che la accenda,
che vi infonda l'impulso alla ricerca e il desiderio della verità.
[Plutarco, De recta ratione audiendi]

INDEX

INTRODUCTION

The Heavy Ion Collisions (HICs) at intermediate energy regime ($10\,MeV/A < E/A < 100\,MeV/A$) are an appropriate environment for the investigation of the features of the nuclear interaction in the matter. The CHIFAR experiment was carried out at INFN-Laboratori Nazionali del Sud: the main aims were the study of the reaction mechanisms, the Intermediate Mass Fragments (IMFs) emission probability and the isospin role in HICs. Some nuclear reactions were studied by the CHIMERA Collaboration. From the combinations of three different beams and as many targets, the following collisions were chosen to compare the trend of the emission products between neutron rich and neutron poor systems:

- $^{124}Sn+^{64}Ni$, also called "neutron-rich" system
- $^{112}Sn+^{58}Ni$, also called "neutron-poor" system
- $^{124}Xe+^{64}Zn$, also called "isobaric" system
- $^{124}Sn+^{64}Zn$
- $^{112}Sn+^{64}Ni$
- $^{124}Xe+^{64}Ni$.

All the above-mentioned nuclear collisions were studied at $20\,AMeV$ of beam incident energy, specially selected to extend the knowledge of the nuclear interactions and of the isospin role at lower energy range with respect to some previous experiments, such as REVERSE or InKiIsSy, where the same systems and physics cases were investigated at $35\,AMeV$ [DEF14, RUS20].

The CHIMERA multi-detector, mounted at INFN-LNS, permits to detect simultaneously all the charged particles emitted in the final

state of the HICs. In the studied semi-peripheral reactions, the reaction mechanism is typically binary, that means the Projectile-Like Fragment (PLF) and the Target-Like Fragment (TLF) are the main products of the process. The secondary emissions include the evaporation of neutrons, the emission of Light Charged Particles (LCPs) and of gamma rays from the excited PLF and TLF. Finally, in some cases, identified also such as “ternary events”, another class of massive particles must be considered to explain the full reaction pattern, because in the first phase of the interaction an overlap could be created from the connection region between the projectile and the target. It is a “neck” of the matter between the PLF and the TLF: the “neck rupture” gives rise to a third massive body, the so-called Intermediate Mass Fragment (IMF).

Although the IMFs production in the mid-rapidity region was investigated in many experiments still remains many open questions. We know that in this rapidity region the emission process of the IMFs is characterized by a velocity in the laboratory frame that is like (or slightly higher than) that of the center of mass in a broad distribution. If the process is dominated by statistical emission, the velocity distribution of the massive particles is determined by the Coulomb repulsion. In detail, the velocity of IMFs is isotropically centred around the one of the emitting source (PLF, TLF, compound nuclei, …). Instead, if the process is dominated by dynamical emission, the IMFs relative velocity distribution, with respect to the PLF and the TLF, shows an anisotropic trend. The dynamical transport model [BAR04] predictions are in agreement with the experimental results [DEF14, RUS20], which also highlighted the phenomenon of the isospin migration. In particular, in such dynamical events, the

production of the neutron richer fragments is favoured with respect to the ones produced in PLF/TLF evaporation/fission. This is the mechanism of the “dynamical neck fragmentation”.

The CHIMERA Collaboration paid attention to the features of the IMFs emission in semi-peripheral HICs since some previous experiments, such as REVERSE and InKiIsSy. The main goals were the observation of the ternary events – PLF, TLF, IMFs – and the correlated LCPs, thanks to the CHIMERA high granularity. At first, the REVERSE experiment studied the so-called “neutron rich” system $^{124}Sn+^{64}Ni$ and the “neutron poor” one $^{112}Sn+^{58}Ni$ at $35\ AMeV$ beam energy, in reverse kinematics. Then, the InKiIsSy experiment considered the “isobaric” combination between the two previous reactions, so the $^{124}Xe+^{64}Zn$ has an isospin contribute similar to the “neutron-poor” system and a mass like the “neutron-rich” one. In order to have a broad systematics and to compare more reactions as it possible, the $^{124}Xe+^{64}Ni$ was also studied. These four reactions were useful to highlight the enhancement of the dynamical fission probability in correspondence of the neutron rich configuration. The dynamical break-up and the IMFs emission probability follow the isospin N/Z contribute of both the projectile and the target of the colliding nuclei. The analysis of the REVERSE and InKiIsSy data demonstrated that the role of the isospin content is relevant in triggering the dynamical emission mechanism, while the influence of the mass system can be excluded.

The CHIFAR experiment, main topic of the present thesis, was proposed to investigate the features of the IMFs emission mechanisms (statistical and dynamical) at lower energy, with the final goal of comparing the new results with the previous ones.

The experimental setup will be described in more detail in the second chapter. Briefly, it was characterized by the coupling between the CHIMERA multi-detector and the new FARCOS (Femtoscope ARray for COrrelation and Spectroscopy) correlator. The choice of this apparatus permitted to benefits of the very high performances of the two detectors. In fact, CHIMERA provides a complete description of the reaction events, while a very precise identification of the fragments detected (IMFs and LCPs) in the solid angle coverage can be achieved thanks to the high energy and angular resolution of FARCOS [EVP16].

The experimental procedure, data analysis and results will be discussed in the second part of this thesis, starting from the third chapter and in the following ones. The procedures regarding the energy calibrations of the detectors and the evaluation of the energy resolution will be discussed. The data analysis was focused on the IMFs emission and their identification with the ΔE-E technique. The method of the so-called "pixelation" was implemented and applied in order to improve the reconstruction of the events: the correct position of each particle detected by the FARCOS correlator can be assigned without ambiguity.

The isospin dependence in Heavy Ion Collisions is still deeply investigated. In fact, the isospin degree of freedom plays a crucial role in understanding nuclear interactions (in vacuum and in the medium), thanks to its connection with the Equation Of State (EOS) of the nuclear matter. The merging of the data collected by FARCOS and CHIMERA was very important to select the global variables (e.g. total charged multiplicity, reaction plane, and so on) needed to characterize the emission process. In particular, the CHIFAR

experiment was focused on the physics about the dynamical emission process. The effects so far highlighted are in agreement with the theoretical previsions. Future perspective could concern an improvement of the experimental setup with the integration of a neutron hodoscope like NArCoS (Neutron Array for Correlation Studies), featuring high energy and angular resolution in the neutron signals, under construction at present days in Catania [EVP22].

The possibility of investigating HICs having extreme isospin asymmetry in the intermediate energy regime is also supported by the building of a new fragment separator FRAISE (FRAgment In-flight SEparator) at INFN-LNS [MAR22]. It is on its final construction phase, and it will deliver Radioactive Ion Beams (RIBs) with an intensity suitable for such studies (in a range between $10^5 - 10^7 pps$). Some nuclear reactions have already been proposed to be analysed with FRAISE beams, such as ^{68}Ni+^{124}Sn and ^{56}Ni+^{112}Sn in order to again compare "neutron-rich" and "neutron-poor" systems, respectively.

The last chapter of this work concerns the ASY-EOS II experiment, carried out at GSI-FAIR in Darmstadt, Germany [RUSprop]. It is aimed at the determination of the features of the EOS, putting new and more stringent constraints on the density dependence of the symmetry energy at supra-saturation densities. Simultaneous measurements of the elliptic flow of neutrons, protons and light charged particles are the key observables for this scope. They are investigated through the ^{197}Au+^{197}Au collisions, at four different energies, $280\,AMeV$, $400\,AMeV$, $600\,AMeV$ and $1000\,AMeV$. The experimental setup included various detectors of the R^{3}B Collaboration, such as NEULAND, KRAB, TOFD, LOS-

ROLU, and also four double rings of the CHIMERA multi-detector. The elliptic flow developed in relativistic HICs has been proven theoretically and experimentally to have a unique sensitivity in the characterization of the symmetry energy at supra-saturation density. The high-density regime, like the one tested in ASY-EOS II experiment, which according to the model should reach twice the saturation one, will provide important information for astrophysical predictions of the mass-radius relationship of neutron stars.

CHAPTER 1

Some investigations of the CHIMERA Collaboration on the Heavy Ion Collisions.

1.1. The CHIFAR experiment @ INFN-LNS: dynamical fission and IMFs production at 20 AMeV.

The CHIFAR (**CHI**MERA-**FAR**COS) experiment [DEFprop] was carried out at INFN-Laboratori Nazionali del Sud in Catania, in November 2019, by the CHIMERA Collaboration which involves numerous researchers from INFN-LNS, INFN-Sezione di Catania, INFN-Sezione di Milano, but also coming from Poland and Mexico. The main aim of the CHIFAR experiment was to examine the reaction mechanisms of the Heavy Ion Collisions (HICs), with special emphasis on the study of the Intermediate Mass Fragments (IMFs) emission, in particular at the lower boundary of the Fermi energy regime. The measure of the probability of dynamical and statical emission of IMFs and Light Charge Particles (LCPs) allows to understand the evolution of the reaction mechanism in the transition energy region from Coulomb to Fermi energies.

Another key objective of the CHIFAR experiment was to study the dependence of the symmetry energy on the density, in order to improve the knowledge of the features of the Equation Of State (EOS) of the nuclear matter. The role of the isospin degree of freedom ($i.e.$ the ratio N/Z between the neutron and proton numbers) of the colliding nuclei is the connection parameter with the symmetry energy. The phenomenon of the isospin migration can be observed in Heavy Ion Collisions (HICs) and manifests in two distinct

mechanisms. The first is the isospin diffusion, which arises due to the isospin gradient between the projectile and the target in asymmetric reactions. This process is sensitive to the symmetry energy $S(\rho)$ and reflects a form of the isospin equilibration that occurs during the dynamical evolution of the reaction. The second mechanism is the isospin drift, which is more sensitive to the density dependence of the symmetry energy, specifically the gradient $\partial S/\partial \rho$. Isospin drift occurs in the presence of a density gradient, such as in the low-density neck region formed between the quasi-projectile (QP) and quasi-target (QT) in semi-peripheral collisions, both, in isospin, symmetric and asymmetric. This mechanism leads to a neutron enrichment of the dilute nuclear matter, resulting in the formation of neutron-rich intermediate mass fragments (IMFs), particularly during the early dynamical emission phase [RUS15, DEF05, DEF12, DEF14].

In the previous years, the CHIMERA Collaboration analyzed the complex dynamics of the IMFs emission at Fermi energies in mass and isospin asymmetric nuclear systems. In the REVERSE [DEF14] and InKiIsSy experiments [RUS20], different nuclear reactions were studied at $35\ AMeV$ of beam incident energy. The CHIFAR experiment was planned to investigate the competition between dynamical and statistical emission of IMFs and LCPs as a function of the beam energy, and in particular the total six nuclear projectile and target combinations already observed in the previous two experiments, but at the lower incident beam energy of $20\ AMeV$. The choice of the same HICs is aimed at comparing the main distributions and the results from the data analysis for the two different energies.

The colliding reactions of the CHIFAR experiment are the following:

- ^{124}Sn+^{64}Ni, also called “neutron-rich” system
- ^{112}Sn+^{58}Ni, also called “neutron-poor” system
- ^{124}Xe+^{64}Zn, also called “isobaric” system
- ^{124}Sn+^{64}Zn
- ^{112}Sn+^{64}Ni
- ^{124}Xe+^{64}Ni.

It is clear that they were obtained from the combinations of three beams - ^{124}Sn, ^{112}Sn, ^{124}Xe - delivered by the Superconducting Cyclotron (CS) of INFN-LNS, and as many targets - ^{64}Ni, ^{58}Ni, ^{64}Zn. The chosen systems put emphasis on the isospin content to study its role in HICs, having selected neutron-rich/poor projectile and targets. In Table 1, the isospin value, calculated for each reaction, is reported.

	$I_P = \frac{N_P}{Z_P}$	$I_T = \frac{N_T}{Z_T}$	$I_{reaction}^{mean} = \frac{N}{Z}$
“neutron-rich” $^{124}Sn+^{64}Ni$	1.48	1.29	1.38
“neutron-poor” $^{112}Sn+^{58}Ni$	1.24	1.07	1.16
“isobaric” $^{124}Xe+^{64}Zn$	1.30	1.13	1.21
$^{124}Sn+^{64}Zn$	1.48	1.13	1.31
$^{112}Sn+^{64}Ni$	1.24	1.29	1.26
$^{124}Xe+^{64}Ni$	1.30	1.29	1.29

Table 1: Isospin values of nuclear reactions studied in the CHIFAR experiment.

The experimental setup was well suited according to the aims proposed. The main feature of the apparatus used was the coupling between the 4π CHIMERA multi-detector and the new correlator FARCOS. This configuration was thought to profit of the novel FARCOS array and its improved, with respect to CHIMERA energy

and angular resolution. In fact, CHIMERA is able to provide a complete characterization of the reaction events, FARCOS instead acts as a high-resolution detector giving a very precise description of fragments detected in its limited solid angle coverage (*i.e.* 13°-30° in the laboratory frame system). Furthermore, the coupling of the two detectors allows the study of new observables, such the IMF-IMF and LCP-LCP correlations, which provide information on reaction mechanisms, sources characterization and particles emission times.

The features of the two detection systems will be described in more details in the Chapter 2. Only a few aspects are mentioned in this paragraph in order to better understand how the experimental setup is useful for the physics motivations of the CHIFAR experiment.

The CHIMERA multi-detector, previously utilized in numerous experiments at INFN-LNS, is made by 1192 telescopes. Each telescope consists of a 300 μm thick Si-detector coupled with a CsI(Tl) scintillator (ranging from 3-12 cm in thickness). In its 4π configuration, CHIMERA covers a polar angular range of 1°-176°. Typical energy resolutions (FWHM), determined via elastic scattering, were approximately $\delta E/E < 1\%$ for the Si detectors and about 2% for the CsI(Tl) scintillators [DEF05]. The 4π detector has permitted to study different phenomena, such as the neck fragmentation in the so-called "ternary events" at Fermi energies. In typical semi-peripheral collisions, the reaction mechanism is usually binary, yielding a Projectile-Like Fragment (PLF) and a Target-Like Fragment (TLF) as the primary products at the end of the process. The secondary emissions from the excited PLF and TLF involve the evaporation of neutrons, LCPs and gamma rays. However, these

products alone aren't sufficient to explain the full reaction pattern. However, a third class of massive particles can be generated during the collision. In fact, in the initial phase of the interaction, the connecting region between the projectile and the target creates an overlap, such as a “neck” of diluted nuclear matter between the PLF and the TLF. The subsequent “neck rupture” gives rise to a third massive body, the IMF. If it is emitted in such a process, it will have a velocity in the laboratory frame similar to (or slightly higher than) the center of mass, in a broad distribution. This class of events belongs to the set of the so-called “ternary events” and involves PLF+TLF+IMF.

Thanks to the high performances of the CHIMERA multi-detector that is able to detect fragments up to the target region, in reactions of ^{124}Sn+^{64}Ni and ^{112}Sn+^{58}Ni, a significant cross-section for ternary reactions in non-central collisions was revealed, with the formation of the PLF, TLF as residues, accompanied by the IMFs emission. Light IMFs, with atomic number $Z < 10$, were preferentially emitted due to the neck rupture of the interacting zone between the PLF and TLF. These IMFs can be emitted on short timescales from neck rupture (according to the models within $100 - 200\ fm/c$ after the interaction) in the more dynamical reaction phase, or over longer periods during the sequential decay of either the PLF or TLF (more than $1000 - 1500\ fm/c$) [DEF05, DEF05b]. Experimental data confirmed the theoretical hypothesis: emission of light IMFs is prevalently correlated with the early stages of the reaction in its dynamical phase, and they are emitted from a dilute density region, with respect to the normal saturation density with an higher probability to be neutron enriched; instead, heavier IMFs,

with $Z > 9$, were found to be emitted in a later step of the neck expansion process, in an asymmetric mass splitting of the PLF with aligned three bodies configuration (TLF-IMF-PLF). This last phenomenon was identified as “dynamical fission” or “aligned break-up” because is typically both a symmetric or asymmetric binary splitting of a very exited and non-equilibrated PLF (that follows a DIC excitation) occurring within $1000 - 2000\ fm/c$ that is symilar to a more equilibrated and later stage occurring fission-like phenomenon. The process can be described as a two-step sequential mechanism: a fission-like emission following a deep inelastic collision. It had previously been observed in ^{84}Kr+^{166}Er and ^{129}Xe+^{122}Sn reactions, even at beam energies down to $12.5\ AMeV$ [RUS15, GLA83, BAR04].

Interesting studies as a function of the isospin of entrance channel have been done at $15\ AMeV$ [CAM15]. CHIMERA's results highlighted that the statistical-sequential emission exhibits a similar cross-section for both neutron-rich and neutron-poor Sn+Ni systems. In contrast, the dynamical emission for the neutron-rich system showed an enhancement factor of 1.5-2. This strongly evidenced the dynamical fission's high sensitivity to the entrance channel's isospin, [RUS15, RUS10].

The exciting scientific prospective was to investigate further the dynamical processes and the IMFs production at lower energies using the CHIMERA detector. So, the idea of studying reactions ^{124}Sn+^{64}Ni, ^{112}Sn+^{58}Ni and ^{124}Xe+^{64}Zn at $20\ AMeV$ is connected to explore the significance of one-body dissipation processes and their subsequent influence on the shapes, angular momentum and excitation energies of the systems. Additionally, understanding the

strong competition between fusion and binary channels is crucial for comparison with Stochastic Mean Field predictions [RIZ14]. At these energies, the mechanism of neck evolution respect to the symmetry energy is largely unknown, yet.

The CHIFAR experimental setup also included 10 telescopes of FARCOS correlator in its final configuration: they were grouped into 5 pairs, arranged in a ring-like configuration for better coupling with the sphere part of CHIMERA (see Fig. 1). In this way, a coverage of about ¾ of the 2π azimuthal range was guaranteed while the covering polar angle was in a range of 13°-30° in the laboratory frame. Regarding the identification of the particles, in this configuration FARCOS is able to reconstruct the ions impinging the two Silicon stages of the detector, 300 μm and 1500 μm thick.

FARCOS has a better granularity than CHIMERA. Besides, its energy resolutions and its resolving power permit to study more accurately the link with different time scales of the binary break-up of the projectile. One of the experimental aims was the improvement of the knowledge about the neck dynamics at the lower energy regime: at this moment the dynamics trend with respect to the isospin content behaviour is not clearly known.

FARCOS also gives the opportunity to perform interferometric techniques on LCP, to extrapolate information about emission time and size of the emitting sources [EVP16].

The CHIFAR experiment has given a good opportunity to understand the IMFs production mechanism in HICs, in the final perspective to extend the previous studied [DEF05, DEF05b, PAP07, RUS10, DEF12, DEF14, RUS15, RUS20, PAG20] toward the low energy regime. Finally, the 20 $AMeV$ beam energy is also a strategic

choice connecting to the physics research of the stable beams with SPES radioactive beams, at lower energies than $15\,AMeV$, at Laboratori Nazionali di Legnaro [MAR20].

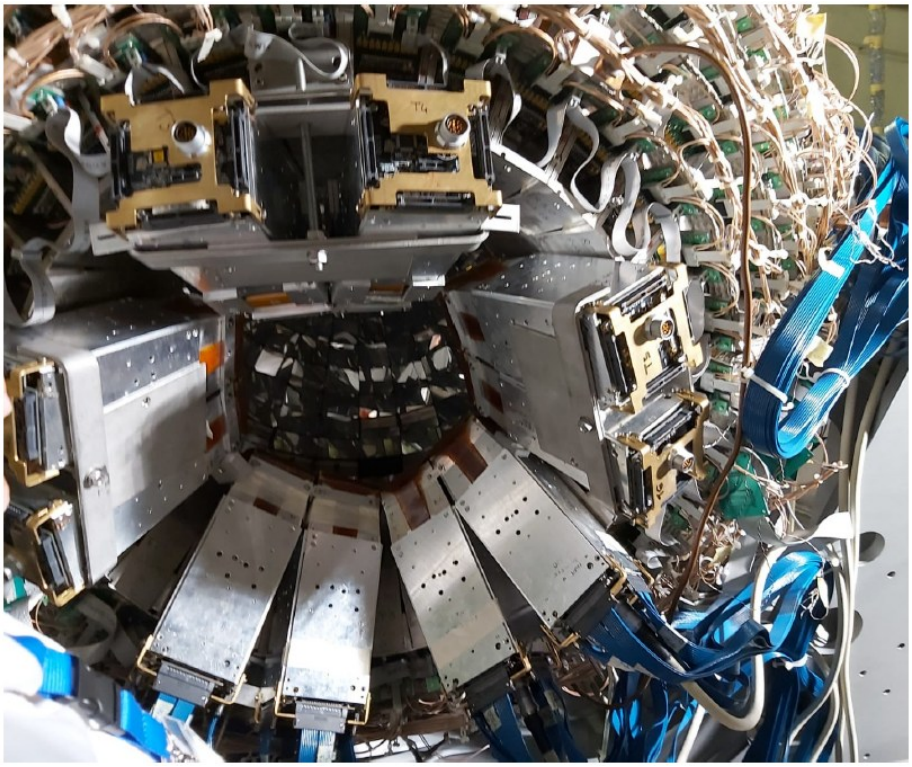

Figure 1: 10 FARCOS telescopes, coupled to the sphere part of CHIMERA, in the final configuration used in the CHIFAR experiment at INFN-LNS in November 2019 [EVP16, webCHI].

The data analysis, which will be discussed in the second part of this thesis, is focused on the six above-mentioned nuclear reactions, studied in the CHIFAR experiment at $20\,AMeV$ incident beam energy.

In the following chapters, a careful description of the work done will be reported, divided into several steps, such as:

i. energy calibration of the Silicon detectors of the new FARCOS correlator
ii. evaluation of the energy resolution of the front and back sides of the Si stages of FARCOS
iii. timing analysis and application of the "pixelation technique"

iv. procedure and achieved results concerning to the particle identification phase relative to the IMFs production
v. preliminary study and results of the isospin role in the HICs at the low beam energy of the CHIFAR experiment
vi. further preliminary studies of the physical cases highlighted by the data analysis, according to the main aim of better understanding the phenomenon of the isospin transport, in order to correlate it with the symmetry energy in the asymmetric nuclear matter and characterize the EOS.

1.2 The physics of Heavy Ion Collisions at intermediate energy regime.

One of the main objectives for the CHIMERA Collaboration is the investigation of Heavy-Ion Collisions (HICs) at intermediate energy regime. The CHIMERA and FARCOS detection systems, housed at INFN-LNS, represent a very useful tool to achieve this purpose.

The intermediate energy domain (and the Fermi one at $35\ AMeV$), is an area of interest for nuclear physics research. It covers the energy range between $10\ MeV/A < E/A < 100\ MeV/A$. It is mainly characterized by a transition behaviour in nuclear reaction mechanisms, as a function of the beam energy and the impact parameter [SCO83]. Within this energy regime and as a function of the impact parameter, phenomena including neck emission, projectile-like dynamical fission, massive ternary breakup, nuclear fragmentation and multi-fragmentation are observed. These events are key indicators of the remarkable evolution of the reaction

dynamics, exhibiting emission timescales that range from very fast (tens of fm/c, or prompt) to considerably slower (hundreds of fm/c, or sequential).

The main features of this transition behaviour can be identified in two aspects:

I. increased dispersion of Projectile-like Fragments: a greater spread in the reduced linear momentum of PLFs, which are created by a fast projectile fragmentation in semi-peripheral collisions, can be seen [GUE85].

II. "rise and fall" trend: the fragment multiplicity produced during multi-fragmentation in central collisions shows a so-called "rise and fall" inclination [LYN95].

Both the central collisions, where the two heavy nuclei collide in the most violent way, and the semi-peripheral ones, provide an ideal scenario for exploring the properties of the nuclear matter. In that sense, the nuclear Equation of State (EoS) [BAR05] and the phase transition in finite nuclear matter [POC95] can be studied.

In the Fermi energies regime ($\approx 35\ AMeV$), nucleus-nucleus collisions permit to describe the dynamical transition from the mean field domain ($< 20\ AMeV$) to the short mean-free path one typical of nucleon-nucleon interactions ($E > 50\ AMeV$). The study of the semi-peripheral nuclear reactions is useful to evidence these effects when analysing the contact zone of the two colliding nuclei. At low incident energy in central collisions, the projectile and the target nuclei create a compound nucleus in the collision; but it is highly unstable. The fission or evaporation determines the final state of the reaction [BOW93, SAN95]. Increasing the excitation energy, and so the incident energy, until the binding one, many IMFs are emitted in

the multiple splitting, and the so-called “multi-fragmentation” becomes relevant at the increase of the incident energy. The multi-fragmentation in central collisions is the clear signal of a disassembling of an excited system.

The so-called “rise and fall” trend is typically observed in the multi-fragmentation phenomenon. It is directly linked to the increasing violence, *i.e.* to the centrality of a collision. Many previous experiments highlighted this correlation [LYN95, SOU90]. Figure 2 illustrates the mean multiplicity of IMFs, defined as fragments with an atomic number $Z \geq 3$, measured in the ^{84}Kr+^{197}Au and ^{197}Au+^{197}Au nuclear reactions, as a function of the beam energy and the impact parameter. These experiments were carried out at the Michigan State University (MSU) and at the GSI Helmholtzzentrum für Schwerionenforschung in Darmstadt. A large systematic of data were collected, the beams used had several energies and the collision products were detected with the Miniball/wall array detection system. In both cases, the principal highlighted result was the average IMF multiplicity peaks at around $100\ MeV/A$ incident energy. To better understand this phenomenon, the experimental data were compared with two theoretical models, for the ^{84}Kr+^{197}Au system (shown on the left panel of the Fig. 2): the Quantum Molecular Dynamic (QMD) simulates the dynamic phase of the reaction leading to the formation of a hot source, taking place in the first stage of the reaction, while the Statistical Multifragmentation Model (SMM) is used as after-burner to reproduce the emission of particles from the hot-source. A decrease at higher energies was expected and observed in the ^{197}Au+^{197}Au reaction, as can be seen in the right panel of the Fig. 2: the wide incident energy range of the examined data allowed

to roughly determine the energy value of the beginning of the decrease. Furthermore, it is accompanied by a shift of the multi-fragmentation process towards more peripheral collisions.

The aim was to propose a proper description of the multi-fragmentation nuclear process. It suggests that fragment production occurs after a fast compression and expansion phases, involving a transition from normal nuclear density ($\rho_0 \approx 0.17\, nuc/fm^3$) to a lower density ($\rho \sim 0.3\rho_0$). This density change leads to the creation of clusters, a state referred to as the "freeze-out configuration".

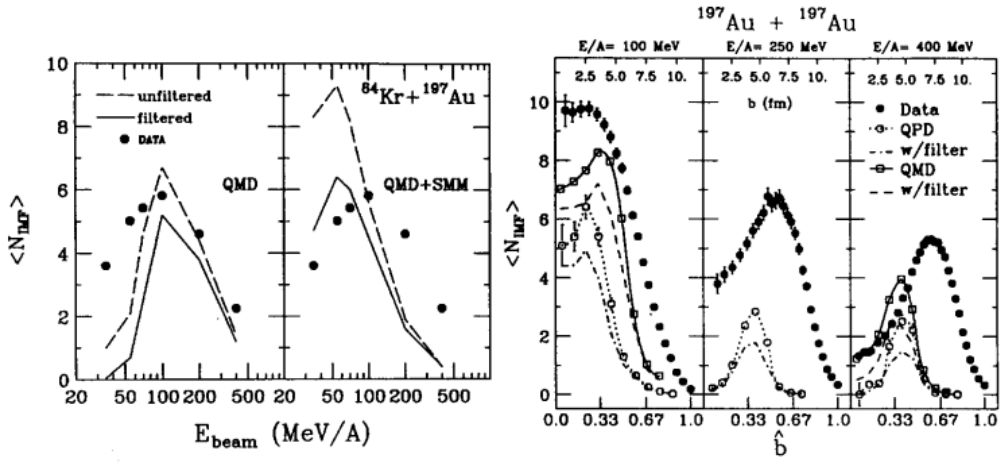

Figure 2: Mean IMF multiplicity measured in the $^{84}Kr+^{197}Au$ nuclear reaction, as a function of the beam energy, compared to QMD and QMD+SMM calculations (left panel); a decrease at higher energies was observed in the $^{197}Au+^{197}Au$ collisions, as a function of the impact parameter (right panel) [LYN95].

About the time scale of the multi-fragmentation phenomenon, analyses focusing on velocity correlation functions have consistently shown that multifragmentation is a very fast process, occurring on the order of $100\, fm/c$. This timescale is directly linked to the complete transfer of energy.

Several experiments [NAT81-RAM85] focused on the PLF emission at lower energies ($30 - 60\, AMeV$) with typical features, in semi-peripheral collisions. In the Fermi energies regime, nucleus-

nucleus collisions are characterized by the dynamic transition from the mean field domain to the short mean-free path one typical of nucleon-nucleon interactions. The investigation of the semi-peripheral nuclear collisions is useful tool in order to highlight these transition effects when analysing the contact zone of the two colliding nuclei.

In some events, the IMFs emission is observed to populates a so-called “mid-rapidity region”. This refers to the area where the component of the velocity parallel to that of the beam one (*i.e.* the parallel velocity) is intermediate between the PLF and the TLF rapidities. The IMFs relative velocity distribution, with respect to the PLF and the TLF, and their angular distributions do not follow the characteristic pattern due to the Coulomb repulsion observed in the statistical decay or evaporation. The IMFs emission tends to be anisotropic: this means that IMFs are specially aligned along the PLF and TLF separation axis; furthermore, their relative velocities, with respect to the PLF and TLF, are higher than what would be expected from Coulomb repulsion alone. Another key phenomenon observed in such events is the “isospin drift”, that considering neutrons flow from the PLF and TLF towards the dilute overlap region, linked to the symmetry energy of the asymmetric nuclear matter. This process leads to the production of neutron-richer fragments compared to those formed by the PLF/TLF evaporation or fission.

These observed properties are consistently explained by the dynamical phase of the reaction or neck fragmentation description and are further supported by predictions from dynamical transport models [COL93-PAP01, PAP07].

The CHIMERA collaboration has conducted crucial experiments providing detailed information on the timescale of IMF emission in semi-peripheral nuclear reactions. The CHIMERA detection system, housed at INFN-LNS, was specifically designed to simultaneously detect all three classes of reaction products, that means PLF+TLF+IMF. One of the nuclear reactions studied in reverse kinematics with CHIMERA multi-detector was ^{124}Sn+^{64}Ni at 35 $AMeV$ incident beam energy. The data analysis indicates a broad range of emission times, spanning from a few fm/c to hundreds of fm/c [DEF05, DEF05b, RUS10, RUS14, DEF16].

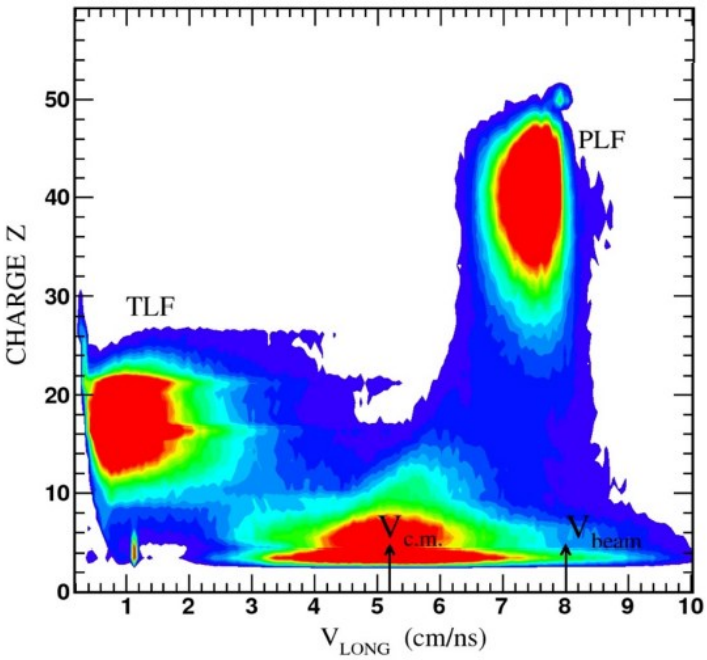

Figure 3: Charge distribution as a function of the parallel velocity for the ^{124}Sn+^{64}Ni nuclear reaction at 35 $AMeV$; three clearly separated regions individuate the emission of TLF, IMF and PLF [DEF05b].

From the data analysis, the two-dimensional charge distribution was studied as a function of the parallel velocity for the reaction ^{124}Sn+^{64}Ni at 35 $AMeV$ [DEF05b]. Conditions of the inverse kinematics greatly facilitated the detection and the identification of the final products. Three clearly separated regions are visible (see

Fig. 3). The first one can be associated to the TLF, in the area around $Z \approx 18$ and with a velocity lower than 2 cm/ns. The PLF instead covers the region corresponding to heavy and relatively fast fragments with atomic number close to that of the Sn projectile (*i.e.* $Z_{proj} = 50$) and moving with velocities of about 7.5 cm/ns, therefore slower than the beam velocity (~8 cm/ns). Finally, the particles distributed in the range of the center of mass velocity (~5 cm/ns) are correlated to the IMF production. The distribution highlights that IMFs are mostly light fragments, up to $Z \approx 15$. The longitudinal velocity spectra of PLFs, TLFs, and IMFs was studied for some selected values of $Z_{IMF} = 4, 8, 12$ and 18 (see Fig. 4). The good separation between PLFs, TLFs and IMFs is also observable in the two-dimensional distributions of the transverse velocities of the ternary events, as a function of the longitudinal velocities (see Fig. 5). In particular, the main characteristics of the IMFs production can be highlighted: they are emitted with parallel velocities intermediate between those of the PLF and TLF; furthermore, the average longitudinal velocity of IMFs does not correspond to the velocity of the center of mass and not even to half of the beam velocity. This means that the IMFs velocity is rather correlated to the mid-velocity, from the average of the two contributes of PLF and TLF:

$$v_{mid} = \frac{1}{2}[\langle v_{long}^{PLF} \rangle + \langle v_{long}^{TLF} \rangle] \quad (1)$$

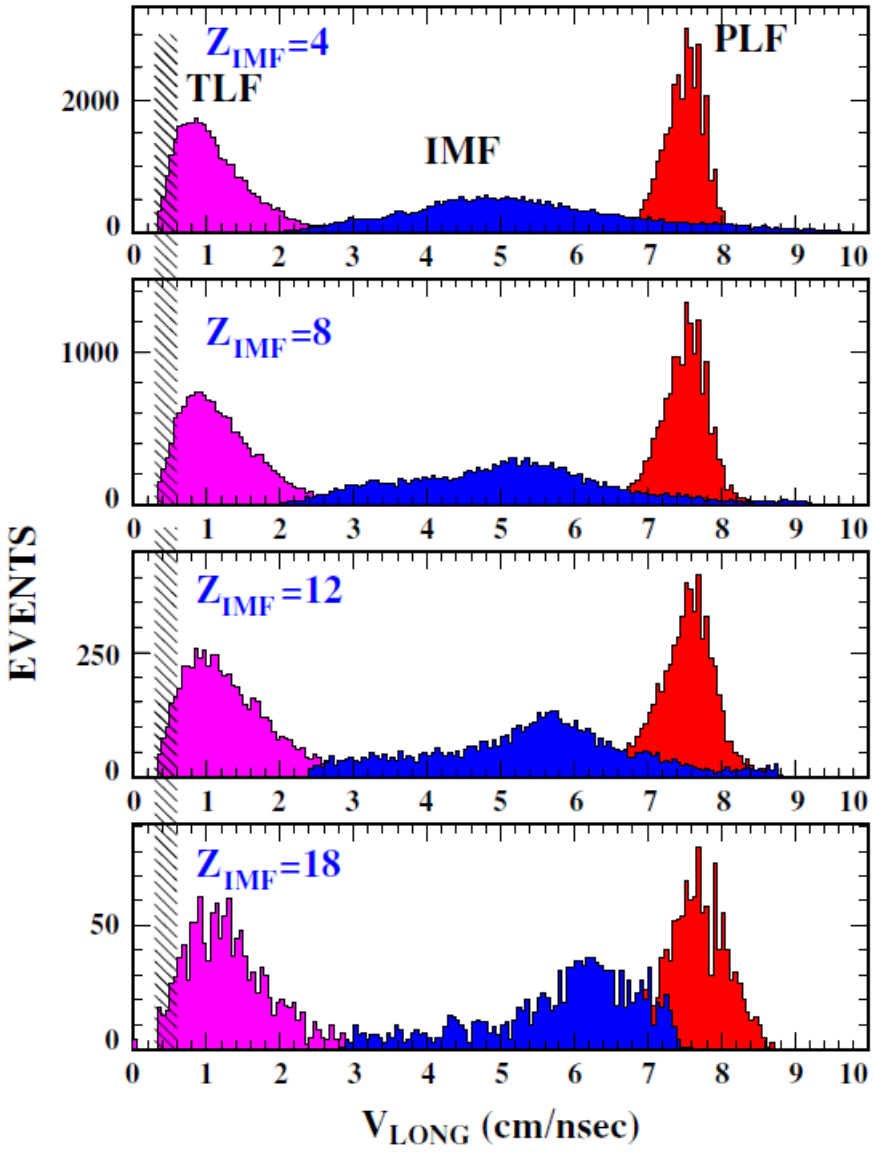

Figure 4: Longitudinal velocity spectra of PLFs, TLF, and IMFs for selected $Z_{IMF} = 4, 8, 12$ and 18; dasched area indicates detection thresholds [DEF05b].

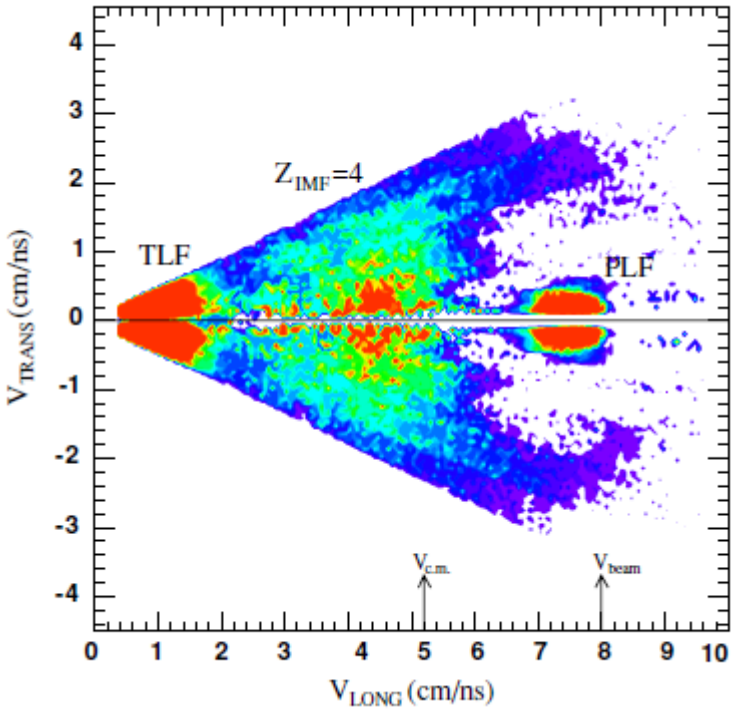

Figure 5: Two-dimensional distribution of the transverse velocities as a function of the longitudinal velocities, for selected ternary events with fixed $Z_{IMF} = 4$ [DEF95b].

All these spectra were compared with the theoretical simulations of the semi-peripheral ^{124}Sn+^{64}Ni collisions at 35 $AMeV$ beam energy, considering the stochastic dynamical model based on the Boltzmann-Nordheim-Vlasov (BNV) transport equations [BAR04]. Experimental results confirmed the theoretical predictions of the neck rupture: the IMFs emission comes from the neck connecting PLF and TLF, after the reseparation of these two fragments.

In the ternary emission, only one IMF is observable, beyond PLF and TLF as final products. Their behaviour is not influenced by some LCPs. In fact, in the analysis of the reaction here discussed, a total charged particle multiplicity less or equal than 7 was well enough to select semi-peripheral collisions.

In this type of reactions, it is very interesting to analyse the distribution of relative velocities of the reaction products, in order to extrapolate useful information on the mechanism of ternary reactions. Specifically, the relative velocity between IMF and PLF - $v_{rel}(IMF, PLF)$ - and then the one between IMF and TLF - $v_{rel}(IMF, TLF)$ - were studied and the correlation results were evidenced in some plots, as shown in Fig. 6. Selecting four groups of events, respectively with $Z_{IMF} = 4, 8, 12$ and 18, the two relative velocities are normalized to the Viola velocity, that corresponds to the kinetic energy expected for the Coulomb repulsion, according to the Viola systematic [VIO85]. The two-dimensional correlation spectra are very helpful in getting information related to the fragments' formation, also including the time of separation of the IMF from PLF or TLF, or also from both in the case of the instantaneous ternary split. The distributions shown loci of points in the $v_{rel}/v_{Viola}(IMF, TLF)$ vs. $v_{rel}/v_{Viola}(IMF, PLF)$ correlations, assuming that the IMF separated from the projectile or from target after a time interval of $40, 80, 120\ fm/c$, after the primary separation at zero time. Points along the first diagonal in that plot corresponds to the case where, both, the relative velocities of the pairs IMF-PLF and IMF-TLF present a significant deviation from what due to Coulomb repulsion, indicating a dynamical emission mechanism well described by the neck-emission scenario. In this case the IMF is expected to be emitted at the beginning of re-separation between PLF and TLF. The time scale is, however, short, into the interval about $120 - 150\ fm/c$; however, in case of the most probable light IMFs, that means fragments with $Z_{IMF} \leq 8$, they are emitter in the so-called "fast two-step" process, within $40 -$

80 fm/c. Moreover, the dynamical emission in neck fragmentation is characterized by an anisotropic angular distribution with respect to the PLF emitting frame, instead sequential/equilibrated production is generally isotropic.

These results and their interpretations were confirmed by transport model simulations, such as Stochastic Mean Field (SMF) [BAR05] and Constrained Molecular Dynamical Model (CoMD-II) [PAP07].

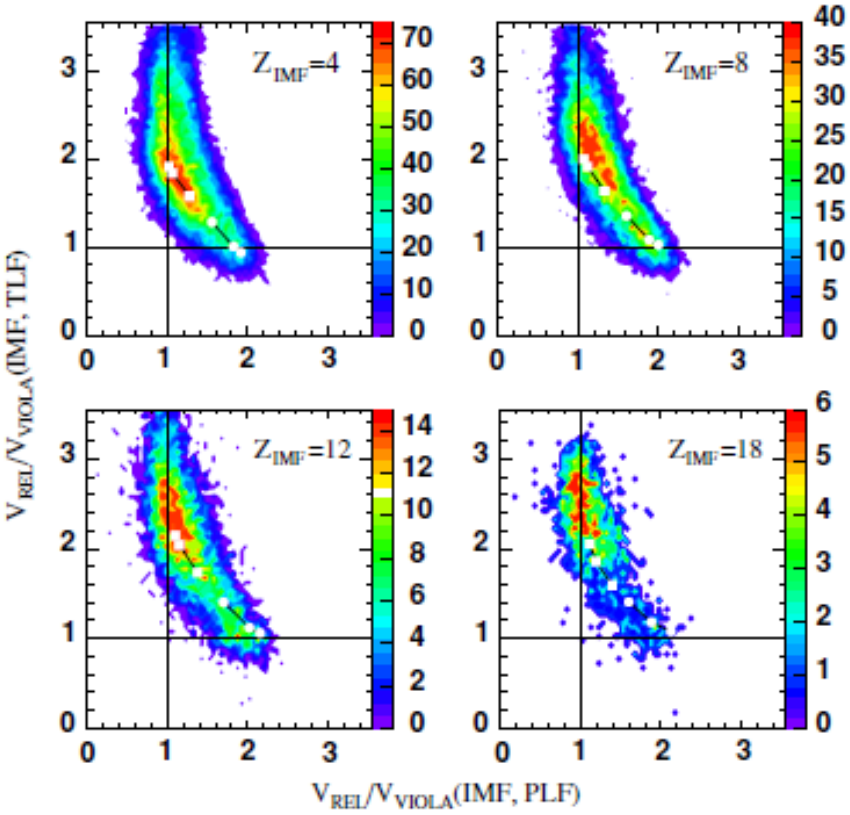

Figure 6: Correlation plots IMF-PLF and IMF-TLF relative velocities normalized according to the Viola systematic, selecting four $Z_{IMF} = 4, 8, 12, 18$, for the $^{124}Sn+^{64}Ni$ nuclear reaction at 35 $AMeV$. Colour scale indicates the number of events. The experimental distributions were compared with model calculations, assuming that the IMF emission is a two-step neck rupture process, in the time interval of 40, 80, or 120 fm/c after the primary reseparation. The shortest separation times correspond to the location near the diagonal $v_{rel}/v_{Viola}(IMF, PLF) = v_{rel}/v_{Viola}(IMF, TLF)$ [DEF05b].

1.2.1. Dynamical fission: study of the emission process in the $^{124}Sn+^{64}Ni$ collision at $35\ AMeV$.

The CHIMERA Collaboration also focuses its physics nuclear research on the investigation of the properties of fast and non-equilibrated emission from projectiles. Using the 4π CHIMERA multi-detector at INFN-LNS, the analysis involved the ^{124}Sn+^{64}Ni reaction at incident beam energy of $35\ AMeV$.

While fast and non-equilibrated fission of projectile-like fragments (PLFs) has been observed previously in heavy ion deep inelastic scattering at both low and high energies [DEF05, STE95, BOC00], the results from these two energy domains show clear differences.

For the equilibrated/statistical fission of the PLF, the angular distribution of the fragments results forward/backward in the PLF reference system. Instead, if the heavier of the two fission fragments is preferentially the faster one, then we are observing a nonequilibrium fission, with the lighter fission fragment located between the heavier one and TLF. This mechanism was highlighted in the study of the PLF de-excitation in the ^{124}Sn+^{64}Ni reaction [DEF05], in the cases of less mass asymmetric PLF splitting, corresponding to $A_H/A_L < 4.6$ and $Z_L > 9$ (A_H and A_L are mass number of the two fission products and Z_L is the atomic number or charge of the light fragment) for that reaction and was called "dynamical fission" (DF).

In order to analyse better the fission of projectile-like fragments in semi-peripherical collisions, it was necessary to pay attention to the two heaviest fragments, accompanied by at most four other

charged particles, taken in coincidence: so, it was imposed $M_{tot} < 7$, as the total charged particle multiplicity condition. In the REVERSE experiment (^{124}Sn+^{64}Ni and ^{112}Sn+^{58}Ni at $35\ AMeV$), the forward part of CHIMERA has a much lower efficiency for TLF: this means that the coincidence condition between PLF and TLF was not set in order to maintain a higher statistic. Instead, a total of 8.5×10^6 events satisfy the requirement of total detected charge $30 < Z_{tot} < 80$ and of the sum of two heaviest charges $Z_{2F} > 15$. Other constraints concerned the kinetic energy loss during the collision and the mass range's fragments.

In order to investigate the DF of PLF, events of interest were selected according to the mass ratio of the two heaviest fragments, so in the range of $1.0 < A_H/A_L < 4.6$. The Fig. 7 illustrates Z_{2F} vs. the lightest fragment parallel velocity v_L^{par} distributions on logarithmic scale, for three different mass asymmetries A_H/A_L and for three ranges of total kinetic energies of the two heaviest fragments E_{2F}: colours indicate the increments of the cross sections, and the red corresponds to the highest one. The microscopic transport model calculations [BAR04] confirmed that the E_{2F} quantity can be used as an experimental measurement of the impact parameter during the collision step of the reactions. The beam velocity is equal to 8.2 cm/ns. Considering velocities distributions, two main components were highlighted: the first one is a very low velocity (about 1 cm/ns), instead the second one is close to the beam (for lower mass asymmetries) or center of mass velocity (for higher mass asymmetries). The first component corresponds to the events in which Z_{2F} is higher than Z-projectile. The low velocity is not

justified by the fusion, that requires higher velocities ($v_L^{par} > 5\ cm/ns$); it's much more likely that low velocities fragments come from targets, such as residues. On the other hand, the high energy group is observed with Z_{2F}~$45 - 50$ and $v_L^{par} > 4\ cm/ns$: it's clear that, in this case, the PLF undergoes splitting in two main fragments.

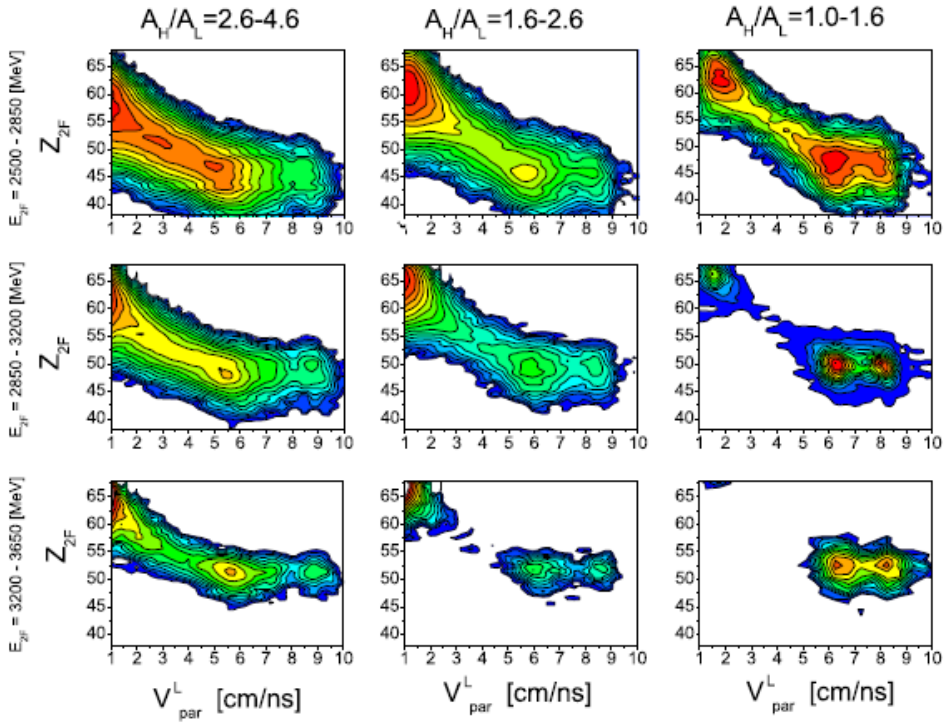

Figure 7: Plots of the sum of charges of the two heaviest fragments (Z_{2F}) vs. the lighter fragment parallel velocity, for three different mass asymmetries and for three ranges of kinetic energies (on a logarithmic scale) for the ^{124}Sn+^{64}Ni reaction at 35 $AMeV$: the red colour shows the highest cross section [DEF05].

These observations are even clearer if we consider the v_L^{per} versus v_L^{par} distributions (Fig. 8), obtained after imposing an additional condition on Z_{2F}: since the maximum Z_{2F} of the high-velocity group shifts downward for smaller values of E_{2F}, as can be seen in Fig. 7, the upper limits of Z_{2F} have been slightly modified. In this way, we can individuate structures of Coulomb rings, centred on the beam velocity (8.2 cm/ns). These suggest a well PLF source and highlight the probable scenario of two sequential reaction steps: the

scattering of the PLF, which then splits into two fragments. In particular, the light fragments are collocated in the low velocity sides of the rings. This is the signature of the "dynamical fission": the lighter fragments are preferentially emitted backward, in the PLF reference system, that means toward the target nucleus. Then, the forward/backward symmetry of the rings is the feature of the second step: it is a very fast process, with the time interval between the two steps shorter than the PLF rotation time; furthermore, the emission direction confirms the forward/backward symmetry. For these reasons, the process is considered a "fast sequential" one [DEF05, DEF05b, BAR04, PAG04].

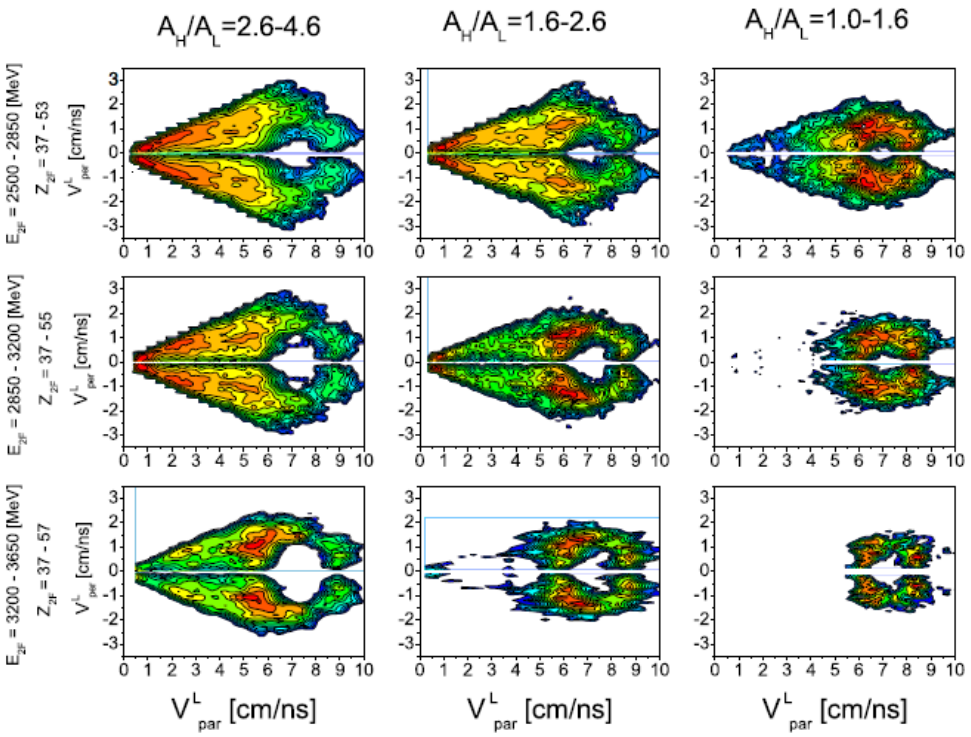

Figure 8: v_L^{per} versus v_L^{par} plots, for the lighter fragment, for different mass asymmetries and for three different kinetic energies (on logarithmic scale) for the $^{124}Sn+^{64}Ni$ reaction at 35 $AMeV$; colours indicate the cross-section's level. Structures of Coulomb rings are centred on the $v_{beam} = 8.2\ cm/ns$ [DEF05].

The reaction plane is defined by the beam axis and the PLF's velocity vector, reconstructed from the couple of the two fission fragments, and it is possible to describe the fission axis, the axis of relative velocity between the two fission fragments, by means of the in-plane angle Φ_{plane} and the out-of-plane angle Ψ_{out} (Fig. 9) [STE95].

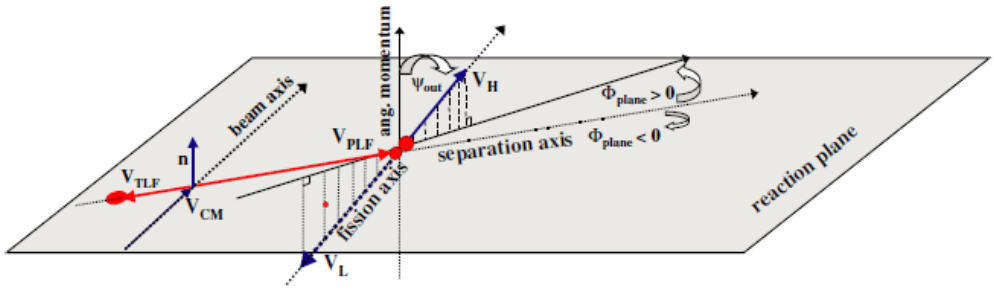

Figure 9: Schematic representation of the reaction plane, indicating the definition of the in-plane Φ_{plane} and out-of-plane Ψ_{out} angles [DEF05].

The direction of $\Phi_{plane} = 0°$ indicates that the heavier fragment is emitted in the forward direction, along with the PLF flight direction. According to a sign convention, $\Phi_{plane} > 0°$ indicates a deflection of the fragment toward the beam axis. From this starter point, the equilibrated (EQ) slow fission can be characterized by a flat in-plane distribution; instead, a peak in the distribution, close to 0° is a typical signal of dynamical (DYN) fast fission.

The Fig. 10 shows the in-plane angular distributions as obtained in the analysis of the reaction here discussed, after a proper selection of the PLF fission-like events. For moderately mass-asymmetric divisions, that means $A_H/A_L = 2.6 - 4.6$, the maximum overhanging the flat equilibrated component. The peak is the signature that the process is fast, and then it shows features that could be ascribed to a "dynamical" fission.

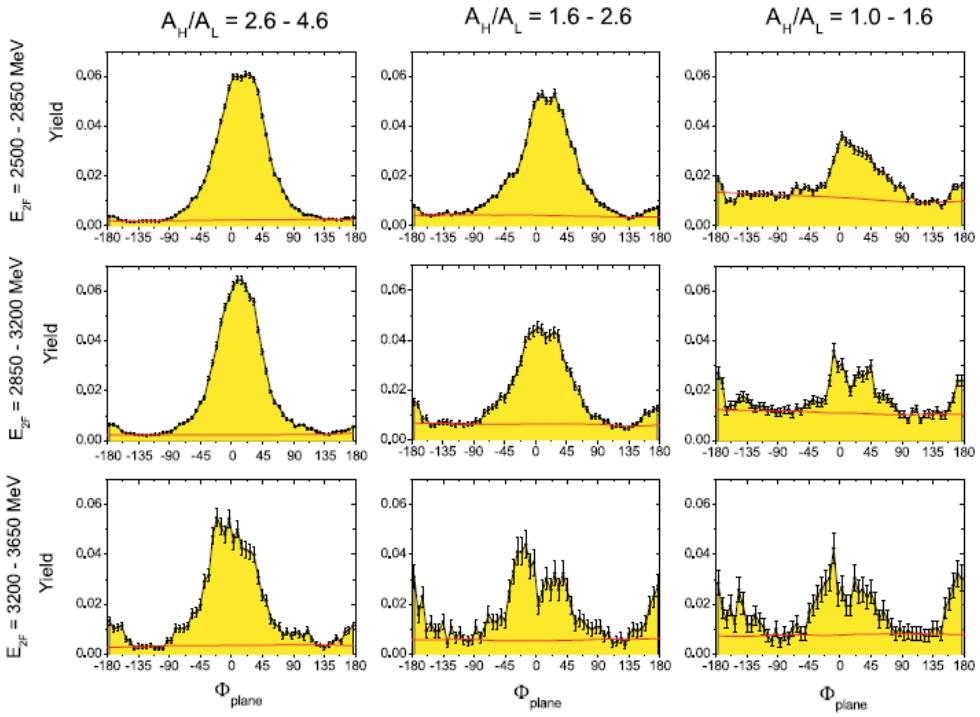

Figure 10: Normalized in-plane distributions of the heavier fragment from PLF splitting. $\Phi_{plane} = 0°$ corresponds to the forward emission in the PLF reference frame, positive angles indicate a deflection toward the beam axis. A second peak at ±180° indicates the forward emission of the lighter fragment. The red line highlights the equilibrated component of the fission, instead the peak is the signature of dynamical fission [DEF05].

The right-left asymmetry of the Φ_{plane} distribution around 0° permits to understand some properties of the dynamical process. The asymmetry can be determined by at least two sources: the angular momentum of the collision and the mass (or charge) asymmetry in the entrance channel, which generate the strong Coulomb repulsion. The first effect is the PLF rotation before its splitting, and then the fragment rotation; the second effect is connected to the neck fragmentation. The distributions are also affected by two other effects: the choice of the v_{par}^{L} condition and the efficiency of the detection system. Unfortunately, there is not adequate models that explain well dynamical fission for the range of asymmetry considered and at Fermi energies; so, we cannot compare experimental results with theoretical predictions. About CHIMERA

efficiency an event generator was used, assuming statistical fission of PLF after scattering on the target. The efficiency dependence on Φ_{plane} is generally flat, except some dips caused by the beam exit hole of the detector.

About the out-of-plane distributions, the out-of-plane Ψ_{out} angle is usually defined as an angle with respect to the normal to the reaction plane [VAN73]. For the in-plane emission, it should be $\Psi_{out} = 90°$. Calculating the Ψ_{out} distributions, separately for DYN ed EQ components, some features become evident. The out-of-plane distributions do not depend on the mass asymmetry, which means the distributions shown involved the sum of all data in the whole range $A_H/A_L = 1.0 - 4.6$. Differing from the dynamical part, the equilibrated part was found to do not depend on the kinetic energy loss. Experimental data under a unique energy range for the equilibrated component ($E_{2F} = 2500 - 3650\, MeV$) are analyzed (Fig. 11), but for three energy intervals in the case of the dynamical contribution. According to the simulations, it was found that dynamical fission has a stronger tendency to populate the region $\psi_{out} = 90°$, corresponding to the emission into the reaction plane; the dependence on the E_{2F} is not an artifact and the width of the EQ emission is significantly larger (by about 70%) than that of the DYN one.

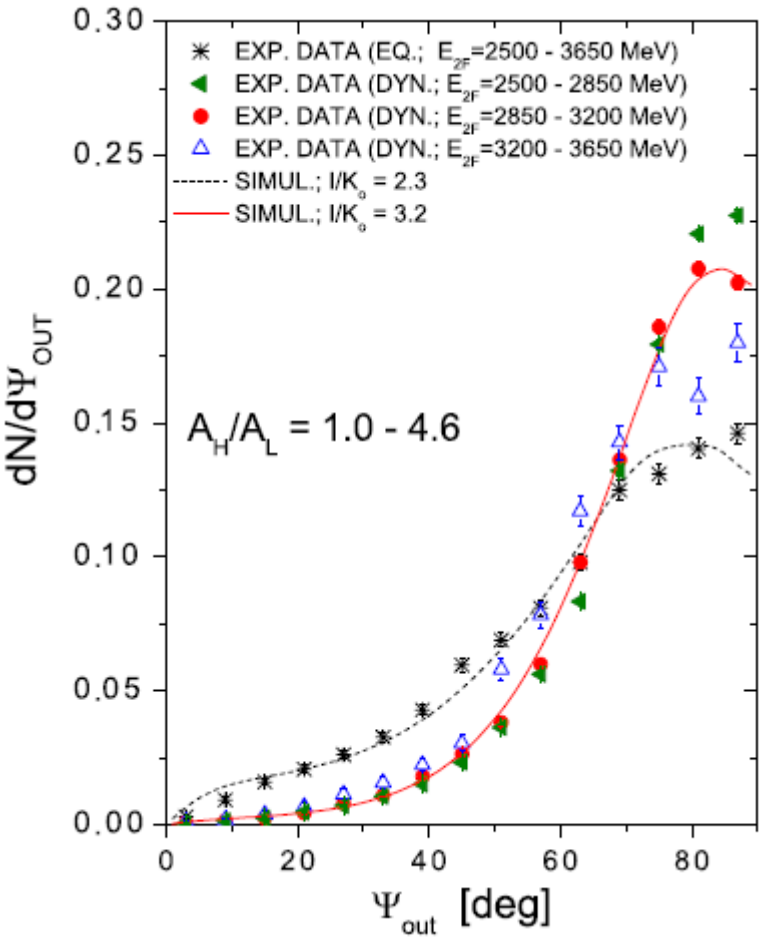

Figure 11: Normalized plot of out-of-plane distributions of fission fragments, for $A_H/A_L = 1.0 - 4.6$ and given E_{2F} intervals, for dynamical and equilibrated components. Dashed lines indicate the statistical model according to the experimental results [DEF05].

The DF phenomenon was also characterized in terms of the relative velocities of the two heaviest fragments. The ring-like structure of the v_L^{per} versus v_L^{par} plots are not circular but rather ellipses. The angular distribution of the relative velocities, normalized to the velocity given by the Coulomb repulsion $\langle v_{ratio} \rangle$, was studied as a function of the in-plane angle (see Fig. 12), taken event by event according to the Viola systematics for asymmetric reactions [HIL92]. For dynamical events, the mean relative velocities become larger by some 10-40% even for $A_H/A_L \sim 1.0$: this means that dynamical events are most probable for higher velocities (with

respect to the Coulomb value), but also the width of the distribution is larger. Even if it appears a sequential process, the angular dependence of the relative fragment velocity is emphasized at lower energy beam [STA96] and for $\Phi_{plane} \approx 0°$, probably also due to the influence of the target Coulomb field. Other significant results can be individuated in the spectra. The normalized relative velocity $\langle v_{ratio} \rangle$ attains a minimum value close to ±120°; furthermore, in more peripheral collisions, *i.e.* $E_{2F} > 2850\, MeV$, for near-symmetric splitting $\langle v_{ratio} \rangle \sim 1.0$ throughout the entire angular range, so the velocity gets equilibrated faster than the dealignment of the fragments. Finally, a small peak is visible around ±180°: now, the relative velocity is close to the condition of the equilibrated fission, so this peak is different with respect to the ones at 0°. The intensity of these two peaks is more comparable for nearly symmetric splitting, *i.e.* $\mathrm{A_H}/\mathrm{A_L} = 1.0 - 1.6$: the percentage of DF rises in a quite unexpected way for this class of events.

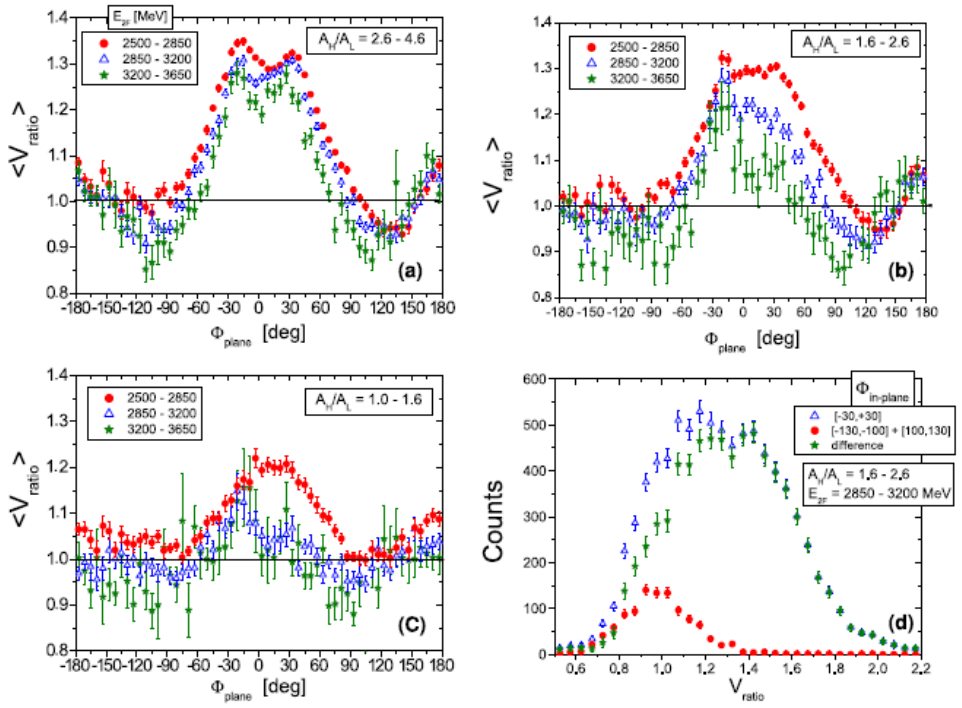

Figure 12: Distributions of the relative velocity of the PLF normalized by Viola systematics, as a function of the in-plane angle, for different centrality of collision and A_H/A_L ratios (panel a, b and c). Velocity spectra at the "dynamical" and "equilibrium" angular regions and their difference (panel d) [DEF05].

About the time scale estimation, the fragments emitted on the short time scale ($t < 100 - 150\ fm/c$) are collocated outside the Coulomb rings. An interpretation of the experimental data, based on rotation of the PLF before fission, gave a time interval between PLF scattering and fission of $12 - 120\ fm/c$, related to the mass asymmetry and the sum of the two energies E_{2F} [DEF05b]. According to the BNV transport model calculations [BAR04], immediately after collision, PLF are not rotating, but frozen in an aligned configuration and the transfer of the angular momentum to the PLF will take some time, corresponding to the centrality of the reaction. Dynamical simulations show a time scale of the order of $200\ fm/c$. According to the model, after this time, we can have some information about the PLF rotation. A time interval between collision and PLF splitting around of $100 - 300\ fm/c$ can be

estimated. In any case, this time is shorter than that typical of equilibrated fission (10-100 times upper). Thus, the fragments, originating from dynamical fission, are produced on the shorter time scale and they are more concentrated in the reaction plane than those from the equilibrated process [HIL92, GOL99].

Summarizing, the defining characteristic of the dynamical fission is the fast, two-fragments emission resulting from the binary splitting of PLF decay. A key aspect of this process is the strong velocity correlation between the two emitted fragments. Specifically, the heavier fragment typically moves faster, and it is ejected in the forward direction relative to the PLF's reference frame. Conversely, the lighter fragment is slower and emitted backward, orienting itself towards the TLF. This specific emission pattern leads to an aligned three-body configuration, often referred to as an “aligned breakup”. Observations in Au+Au collisions at $15\,AMeV$ have revealed similarly aligned, ternary and even quaternary breakup processes, with a time scale about $70-100\,fm/c$ [RUS10, COL03, WIL10, STE95, BOC00].

Experimental findings on neck fragmentation and dynamical fission have been corroborated by simulations performed with two distinct transport codes: CoMD-II [PAP07] and BNV [BAR04]. CoMD-II operates as a molecular dynamics model, employing a self-consistent N-body approach to solve the equations of motion. It incorporates crucial constraints from the Pauli principle and upholds the conservation of total angular momentum. BNV is a stochastic mean-field microscopic approach. It details the evolution of nuclear systems using a Boltzmann-Nordheim-Vlasov type transport equation, which includes a stochastic term to capture the dynamics

of fluctuations. When evaluating collision terms within BNV, particular attention is given to isospin effects, nucleon cross-sections, and Pauli blocking.

The relationship between dynamical and equilibrium PLF fission was thoroughly investigated through a quantitative comparison of absolute cross sections. Specifically, the statistical and dynamical emissions of heavy fragments from ^{124}Sn+^{64}Ni reaction were measured against those from ^{112}Sn+^{58}Ni collision, both conducted at the same $35\,AMeV$ beam energy [PAG01]. The experimental data revealed a compelling result: the dynamical process is twice more probable for neutron rich system than the neutron poor one, indicating a measurable difference into the reaction mechanism. The origin of the enhancement of the dynamical fission is due to the entrance-channel isospin N/Z term, different for the two systems analyzed. Therefore, theoretical simulations of this effect would be of great importance [RUS10].

1.2.2. The influence of the N/Z isospin entrance channel on the dynamical emission probability of IMFs.

In Heavy-Ion Collisions at Fermi energies, the creation of LCPs and IMFs is linked to reaction mechanisms that operate on different timescales. This was more evident in semi-peripheral collisions, where the coexistence of light IMFs emission from the neck rupture, PLFs massive break-up and equilibrated PLF fission-like emission can be observed within the same range of impact parameters. Considering the timescale parameter, the competition between reaction mechanisms is more evident. When emission occurs in a statistical or equilibrated scenario over a long timescale (*i.e.* $\gtrsim$

$1000\ fm/c$), it's generally categorized as “statistical emission”. In opposition, dynamical processes are characterized by a non-equilibrated emission that happens on a much shorter timescale (*i.e.* $\approx 50 - 500\ fm/c$) [RUS20, GLA83, DEF12, RUS10].

Works conducted by the CHIMERA collaboration have investigated the emission probability of IMFs in non-central collisions, for the two so-called “neutron-rich” ^{124}Sn+^{64}Ni and “neutron-poor” ^{112}Sn+^{58}Ni systems, at the beam energy of $35\ AMeV$, investigated in reverse kinematics [RUS10, BOC00, RUS15].

The initial properties of the colliding nuclei play an important role in the final outcome of the reaction; in particular, the role of the isospin degree of freedom and of the system size was studied. The previous results [RUS10, BOC00, RUS15] showed as binary statistical equilibrated PLF break-up was equally probable in the two investigated neutron rich/neutron poor Sn+Ni systems, while the fast dynamical emission was favoured for neutron rich system, especially for IMFs heavier than $Z = 7$. Since the atomic number are the same in the two studied systems, for the projectile and the target, the enhancement of the dynamical fission in the neutron rich one could be ascribed to the isospin ratio N/Z, that means the entrance channel isospin influence, but a possible influence of the mass difference could not be excluded at the beginning. For this reason, a new experiment was proposed, the InKiIsSy experiment [RUS20], including also the analysis of the ^{124}Xe+^{64}Zn nuclear reaction. It’s a combination that use the same mass of the previous neutron rich system (i.e. ^{124}Sn+^{64}Ni) and a N/Z content close to the isospin ratio of the neutron poor one (i.e. ^{112}Sn+^{58}Ni), at the same bombarding energy $35\ AMeV$. In addition, also ^{124}Xe+^{64}Ni was studied. The

choose of two targets is related to the difference of the atomic number Z and, consequently, of the isospin N/Z ratio. The respective isospin values of each reaction studied are already reported in the Table 1 of this thesis. The data of the InKiIsSy experiment were collected at the INFN-LNS in Catania; the experimental setup involved the 4π CHIMERA multidetector, and a small portion of the solid angle was covered by a first prototype of the FARCOS correlator, in order to collect IMFs with high angular resolution.

In order to study the probability of the dynamical or statistical IMFs emission, a complete reconstruction of the excited PLF* is mandatory. Event by event, two constraints were verified: i) the sum of the total detected charge greater than 35 (*i.e.* $Z_{tot} = \sum_i Z^i > 35$), ii) the sum of the total linear momentum along the beam axis greater than 60% of the projectile momentum (*i.e.* $p_{par}^{tot} = \sum_i p_{par}^i > 0.6\, p_{proj}$). The distributions of the atomic charge number as a function of the parallel velocity were studied for the two different Zn and Ni targets (see Fig. 13). For both systems, the PLF was individuated, as the heavy remnant of primary PLF* break-up or evaporation. The comparison between the plots highlighted a tendency to detect lighter PLF and a slightly broader velocity distribution for the ^{124}Xe+^{64}Ni collision. A probable reason of this trend is the enhancement of the probability of the PLF* fragmentation for the Ni target, which lead to a lighter PLF residue with a wider velocity distribution. A contribution of fragments also coming from the target is observable at low velocities. The most IMFs in coincidence with PLF were light, with $Z \leq 10$. In order to focus on the IMFs emission process from the PLF* source, a

condition on the parallel velocity was imposed: it had to be greater than 3 cm/ns. The TLF and consequently the IMFs it generates were discarded.

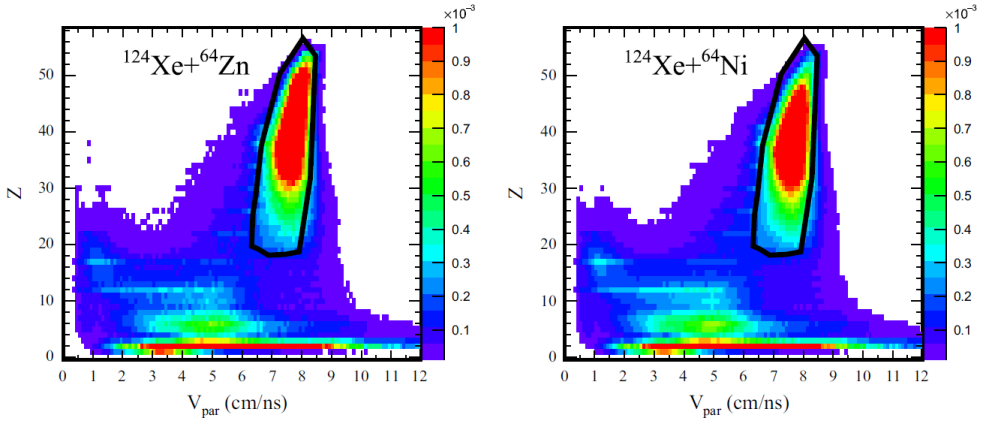

Figure 13: Parallel velocity distributions, as a function of the atomic number, for the ^{124}Xe+^{64}Zn (left panel) and the ^{124}Xe+^{64}Ni (right panel) systems; the graphical cut individuates the PLF residue [RUS20].

One of the aspects addressed in the analysis was the IMFs multiplicity distribution, normalized to the unit, originating from the excited PLF*, for the ^{124}Xe+^{64}Ni and ^{124}Xe+^{64}Zn systems. The experimental results were compared with the predictions of HIPSE+SIMON [LAC04] event generator code (see Fig. 14). The agreement appeared very good: no appreciable difference was expected between the two systems; but in contrast an enhancement of IMFs production probability was experimentally observed for the Ni neutron rich target. In order to understand the influence of the N/Z entrance channel, the comparison of the IMF multiplicity trend, shown in Fig. 15, was also extended to the "neutron-rich" ^{124}Sn+^{64}Ni and "neutron-poor" ^{112}Sn+^{58}Ni systems. A higher IMF emission probability for neutron rich configurations was expected and confirmed. By comparing the results with the ^{64}Ni target and ^{124}Sn and ^{124}Xe projectiles, an enhancement of dynamical IMFs emission probability was found for the neutron richer projectile ^{124}Sn, with no

sizeable differences concerning the probability of the statistical decay. This means the role of the projectile N/Z content in triggering of the IMFs dynamical production.

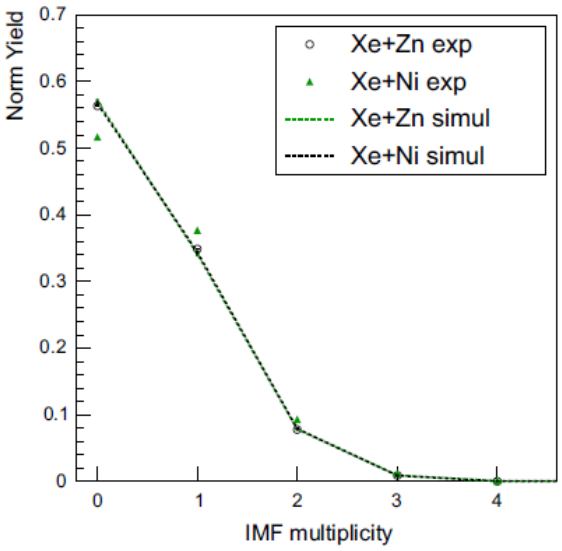

Figure 14: IMFs multiplicity distribution, normalized to the unity, for ^{124}Xe+^{64}Zn and ^{124}Xe+^{64}Ni systems; dotted lines indicate the predictions of HIPSE+SIMON event generator code [RUS20].

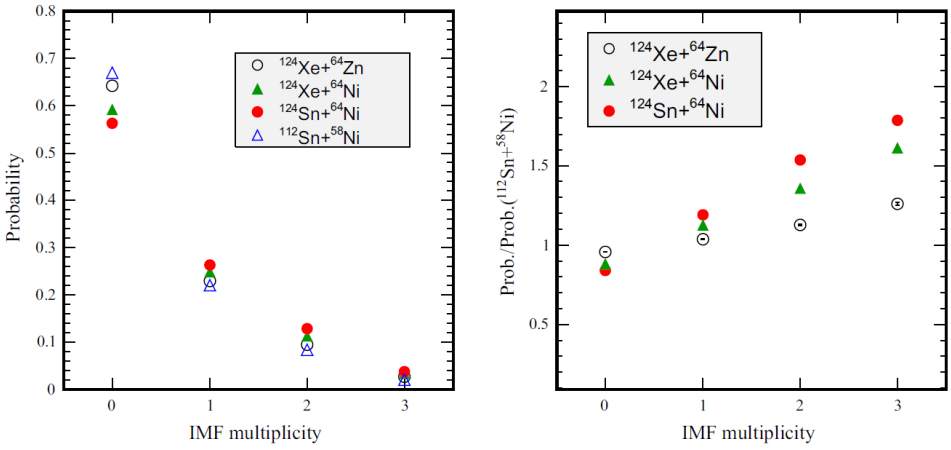

Figure 15: Comparison of IMFs multiplicity distributions, for ^{124}Xe+^{64}Ni, ^{124}Xe+^{64}Zn, ^{124}Sn+^{64}Ni and ^{112}Sn+^{58}Ni systems (left panel); ratios of probabilities, respect to the ones of ^{112}Sn+^{58}Ni system (right panel) [RUS20].

The first conclusion, that for the neutron-rich systems the dynamical fission is more probable, also provides some hints about the role of the target isospin N/Z ratio in early dynamical phases. The right panel of the Fig. 15 shows this enhancement of the production probability, according to the N/Z ratio: a bigger

difference was found when changing the target, from Ni to Zn, than when changing the projectile, from Xe to Sn (see Fig. 16). This implicates that the IMFs emission probability from PLF break-up shows a greater sensitivity on the target N/Z content rather than on the projectile itself.

The production of IMFs was then studied for those events with only one IMF emitted from the PLF. In this case the contributions of the dynamical and statistical emissions probabilities were studied. The ratio of the dynamical probability to the to the total one (statistical + dynamical), was determined for all IMFs, as a function of the atomic number Z of the IMFs. The results are plotted in Fig. 16.

The comparison between the couple of systems with Xe projectile allowed to observe an enhancement of the dynamical emission for the IMFs having $Z \gtrsim 7$, for the neutron rich Ni target. This fact permitted to affirm that, for isobaric targets, the IMFs dynamical emission probability from PLF* binary break-up is related to the increase of the target isospin N/Z. By comparing the data with the ^{64}Ni target, the dynamical emission probability increased in the case of the ^{124}Sn neutron rich projectile. Also in this case, a bigger enhancement of the dynamical fission probability was found changing the neutron rich target, from Zn to Ni, than when increasing the projectile isospin N/Z content, from Xe to Sn. We could affirm that the dynamical IMF emission probability in the PLF break-up is more sensitive on the target N/Z term rather than on the projectile one.

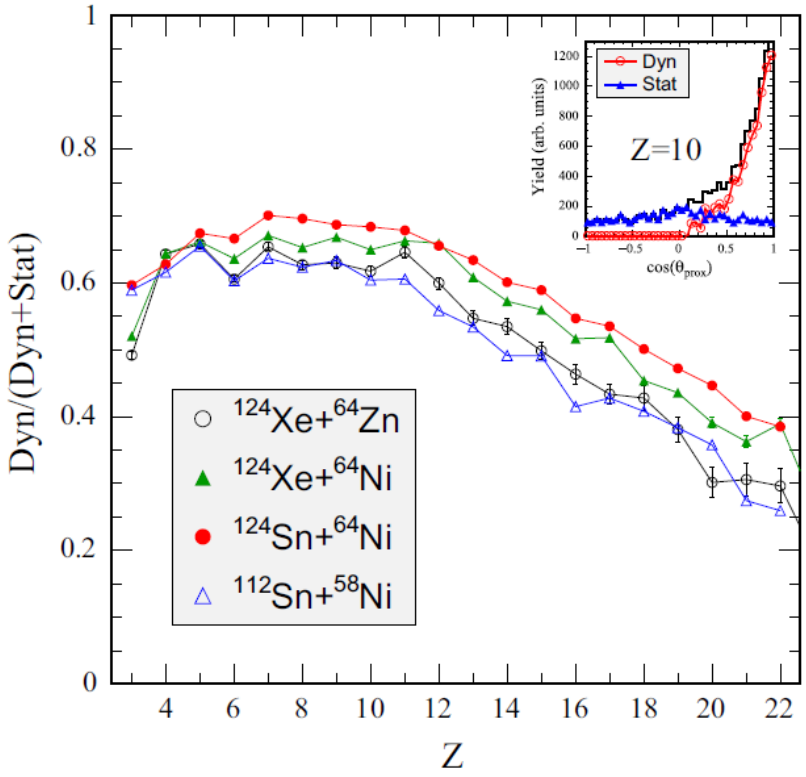

Figure 16: Ratio of dynamical component and total one, as a function of the IMF atomic number, for ^{124}Xe+^{64}Ni, ^{124}Xe+^{64}Zn, ^{124}Sn+^{64}Ni and ^{112}Sn+^{58}Ni systems; the inset shows the result extracted by the relative weights of dynamical and statistical emission, from $cos(\theta_{prox})$ distribution [RUS20].

At this point of the experimental data analysis [RUS20, BAR04, RUS15], the dynamical break up, that means the dynamical IMF emission probability depends specifically on the isospin N/Z ratio of both projectile and target; instead, the influence of the system size on the dynamical fission can be reasonably excluded.

CHAPTER 2

The experimental setup of the CHIFAR experiment.

1. The FARCOS detection system: a new correlator for spectroscopy and nuclear reactions.

The investigation of the dynamics of the HICs at intermediate energy regime ($10\,MeV/A < E/A < 100\,MeV/A$) is still a topic of interest in the perspective of characterizing some open questions in nuclear physics. The main focuses are:

i. the study of the density dependence of the symmetry energy, for the Equation of State of the nuclear matter.

ii. two-particle correlations at lower energies, in order to investigate the emission times of particles coming out from a compound nuclei with large isospin N/Z asymmetries, but also, at higher energies femtoscopy correlations in order to study the space-time properties of the emitting sources.

iii. spectroscopy and correlation among different particles: exotic nuclei are also produced in the HICs; the measurements of observables, such as linear momentum and energy, of the detected particles permit to reconstruct the parent nucleus and its spectroscopic features, in areas of interest also common to nuclear astrophysics.

iv. Direct reactions with stable and radioactive beams, in order to probe exotic nuclei in inverse kinematics.

v. Bose condensate states in nuclei, which can be identified by the emission of alpha particles.

In order to investigate these subjects of the nuclear physics, it is crucial to use a detection systems providing high energy and angular resolution and granularity. The main designed topology for studies of spectroscopy and particle-particle correlation is based on 'hodoscope' (from the Greek *οδός*, that means way or path, and *σκοπός*, that means observer). It is a combination of several stages of Silicon detectors and scintillators [ACO17, ACO19]. The final results would be a highly portable correlator arrays, coupled with other 4π detectors, in order to increase their physics reach. One of these arrays is the new generation correlator FARCOS (Femtoscope ARray for COrrelation and Spectrosopy) [EVP16], specifically designed to improve the knowledge of two/multi-particle and Intermediate Mass Fragments (IMFs) correlations in HICs at Fermi energies, using stable and radioactive beams.

The project of FARCOS was developed inside the CHIMERA Collaboration, operating at INFN-LNS, INFN-Sezione di Catania and INFN-Sezione di Milano. In its final configuration, the correlator consists of 20 telescopes. The modular structure of each telescope identifies a unique cluster of three detector stages. Two Double Sided Silicon Strip Detectors (DSSSDs) constitute the first two stages of the single telescope: they have a structure of 32 vertical strips in the front side of the detector and other 32 horizontal strips in the back side; the two stages differ only in thickness, 300 μm for the first one and 1500 μm for the second one, both having an active area of 6.4 x 6.4 cm^2. The last detection stage is a calorimeter composed by 4 CsI(Tl) troncopyramidal scintillator crystals of 6 cm thickness and active area of 3.2 x 3.2 cm^2; the output electronic signal is read by a Si photodiode of 18 x 18 mm^2 area and 300 μm thick silicon PIN

diode. Finally, the signals are processed by ASIC (Application Specific Integrated Circuit) preamplifiers [CAS18] and digitized with the GET electronic [POL18]. The structure of each telescope consists of 132 readout channels, and other four electronic pulser lines useful for test, calibration and monitoring out of the individual telescope. Therefore, the total number of readout channels for the final FARCOS configuration will be composed of the sum of:

- 32 channels for side x 2 sides (front and back) x 2 DSSSDs x 20 telescopes = 2560 readout channels.
- 1 Si photodiode signal x 4 CsI(Tl) x 20 telescopes = 80 readout channels.

The architecture of the cluster requires some specific interconnections, namely between the detector stages and the motherboard, then between the motherboard and the patchpanel, and the last one between the patchpanel and the backend, with the vacuum feedthroughs. The interconnections must minimize the resistance and the inductance of the power lines, because the main issue is to achieve the signal integrity. A custom-designed vacuum flange is used for two clusters (see Fig. 17), with a total of: 264 differential lines + 8 differential control signals for calibration + 20 bias lines + 4 lines for the slow control system [ACO17]. The Fig. 18 shows a schematic representation of the typical assembling of one FARCOS cluster. In the following paragraph, the front-end electronics of the correlator will be described.

FARCOS was designed with the aim to construct an array of detectors with high energy and angular resolution, focused on the study of Heavy Ions nuclear reactions at Fermi energies. One of the main features is the possibility to identify the particles that are

stopped even in the first detection stage, relying on silicon pulse shape analysis techniques. The energy resolution of FARCOS detection system should be less than 20 $keV\ FWHM$ at 5.5 MeV α-particles, the angular resolution better than 1°, the detection threshold around 1 MeV and the total counting rate of at least 1 kHz. The full-scale energy range is digitally selected, from 100 MeV up to 2 GeV. The main strength is the capability to improve the measurements of the correlation between IMFs and LCPs or even between several IMFs [ACO19].

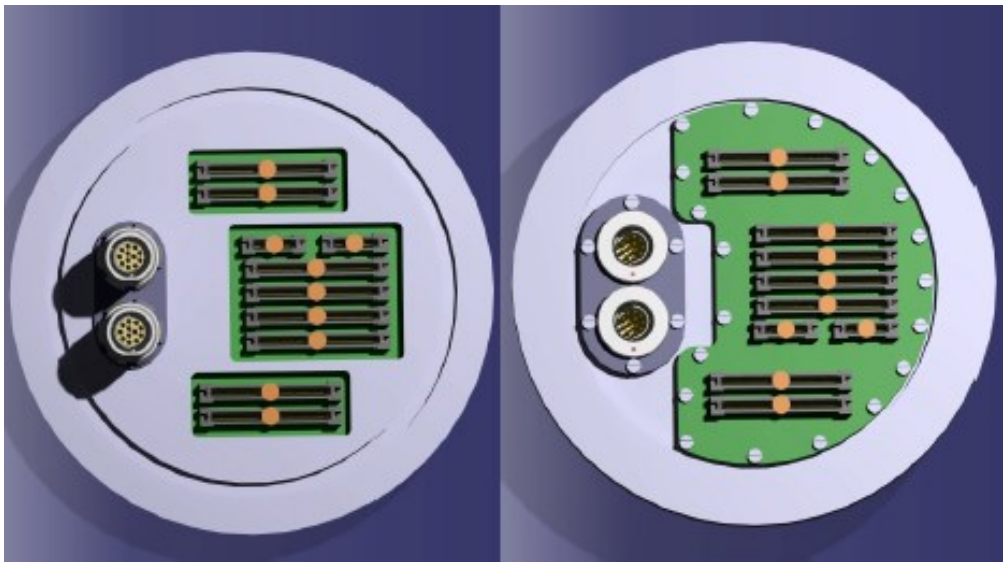

Figure 17: The custom-designed vacuum flange with interconnections for two clusters, for the vacuum side (on the left) and the air side (on the right) [ACO17].

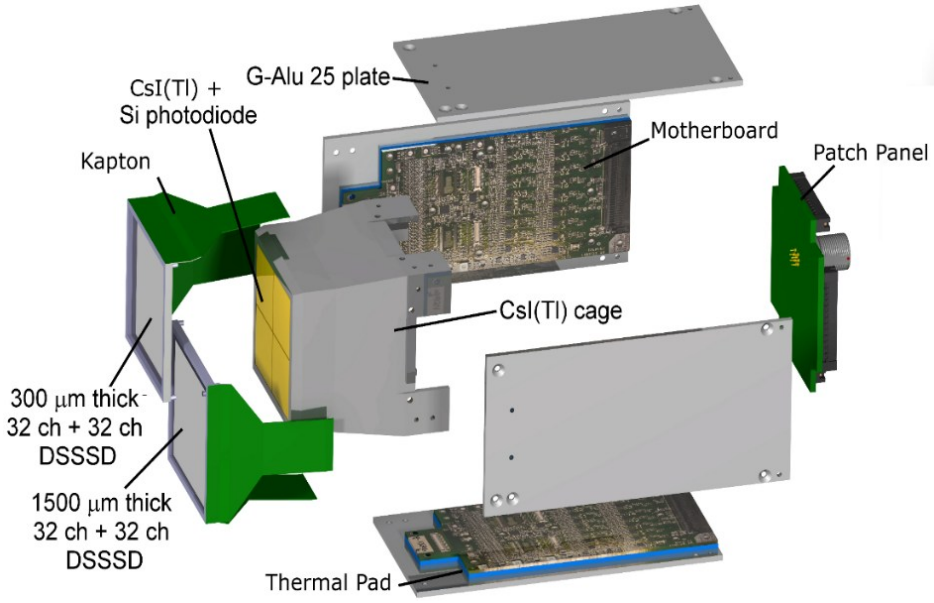

Figure 18: Schematic representation of a FARCOS cluster, with its own ASICs preamplifier mounted on a motherboard [webCHI][ZAG25].

The portability and modularity of the FARCOS structure allow the coupling with other 4π detectors, such as the CHIMERA multi-detector but also with other correlators and/or magnetic spectrometers. Furthermore, the new-generation of Radioactive Ion-Beam facilities (RIB), achievable after the upgrade of the heavy ions Superconducting Cyclotron (CS) at LNS (or alternatively from SPES at LNL, FAIR at GSI, SPIRALII at GANIL, FRIB at MSU) should increase the interest of the measurements of experimental observables with high resolution, such as the momentum and the energy of the detected particles [EVP16].

1.1 The first employs of FARCOS in some experimental tests.

A FARCOS prototype was tested at INFN-LNS in Catania in April 2013. For the first time, only 4 clusters were coupled with the 4π CHIMERA multi-detector, during the InKiIsSy (Inverse Kinematic Isobaric System) experiment [RUS15], using beams delivered by the CS of INFN-LNS. The $^{124}Xe+^{64}Zn$ and $^{124}Xe+^{64}Ni$

reactions were investigated at 35 $AMeV$, focusing on the dynamical emission probability. The 4 FARCOS telescopes covered the angular range of $\theta_{lab} \approx 16° - 44°$ and $\Delta\phi \approx 75°$ in the laboratory frame system. In this way, a portion of the CHIMERA's detectors were shielded from the FARCOS telescopes (see Fig. 19), and the detection of neutrons was encouraged by this configuration. The electronic chain included some preamplifiers to minimize the electronic noise, a signal processing stage (Shaper/Amplifier), and an analog-to-digital conversion phase, followed by data acquisition (DAQ). In the data analysis phase, the ΔE-E identification technique was applied on the two stages of DSSSDs, giving very good results about isotopic identification for IMFs with atomic number up to $Z = 10$. Besides, the PSD method applied to CsI(Tl) signals provided a good LCPs identification up to Li isotopes and ^{8}Be, and the alpha particles in the same telescope (see Fig. 20) [EVP16].

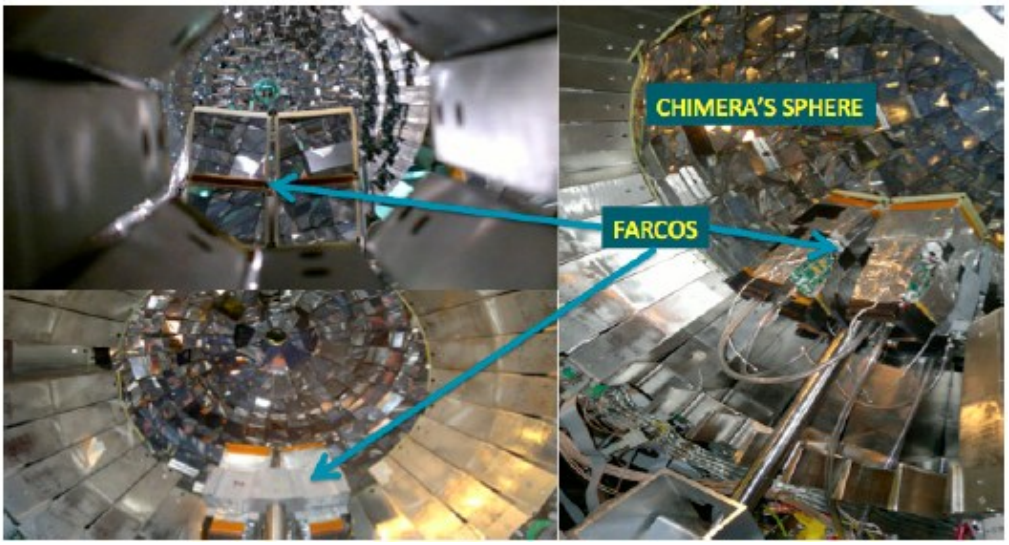

Figure 19: Some photos of the InKiIsSy experimental setup: ^{124}Xe+^{64}Zn and ^{124}Xe+^{64}Ni reactions were investigated at 35 $AMeV$ [EVP16].

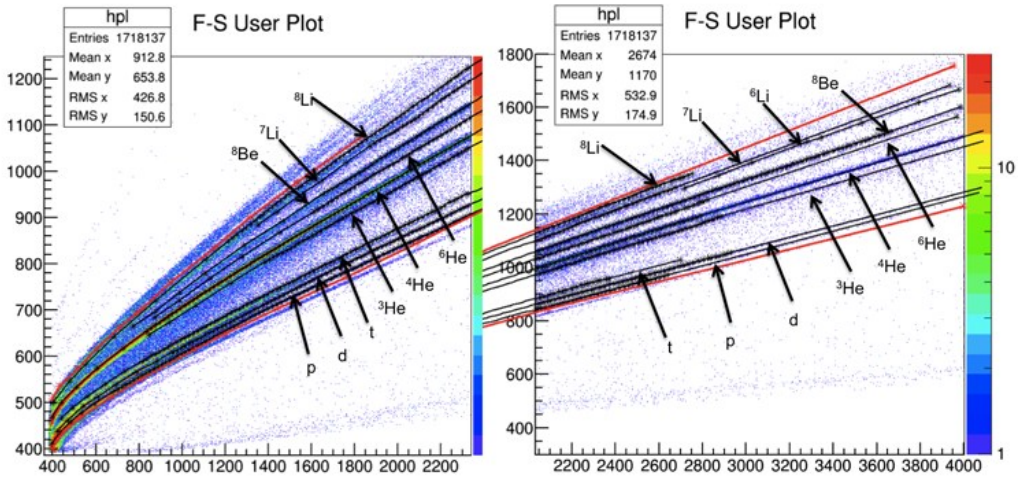

Figure 20: PSD identification in a CsI(Tl) crystal, from the analysis of the InKiIsSy experiment [EVP16].

During this preliminary use of the FARCOS correlator, the GET electronic for readout and DAQ was also tested. In the two-year period of 2015-16, GET system and the ASIC preamplifier were better developed, in collaboration with INFN and Politecnico di Milano. In the following years, other clusters were assembled, in order to obtain a final configuration of 20 telescopes by 2019: the CHIFAR experiment used 10 of them.

On 2015 the FARCOS prototype was used in other two experiments at LNS, that means CLIR for clustering in light exotic nuclei and SIKO for alpha clustering. The results of the identification of detected particles with FARCOS have always shown satisfactory results. So, it was evident the importance of FARCOS in the new generation correlators, for studying Heavy Ions reactions at intermediate energies and for the identifications of LCP and IMFs.

1.2 The FARCOS frontend electronics.

The FARCOS frontend electronics [GUA21] was designed in two releases: the first one has been specifically tested for the 10 telescopes used in the CHIFAR experiment.

Considering the final layout of the custom-designed facility, motherboards consist into 10-layer PCB that houses two FARCOS ASICs, that means 16 + 1 channel ASICs and reads out 32 + 2 detector channels (see Fig. 21). Each chip has 16-channel custom charge preamplifiers, with a full-scale energy digitally selectable following the steps: $100 - 200 - 350 - 500 - 2200\ MeV$, thus ensuring a wide dynamic range and a high electronical granularity. Then, in the second release the full-scale choice is increased with two more steps, $650\ MeV$ and $1700\ MeV$. This electronic facility covers the frontend electronic of the DSSSDs and of the CsI(Tl), but also few slow-control elements, such as on-chip pulser, channel-by-channel test signal injection system, temperature monitor.

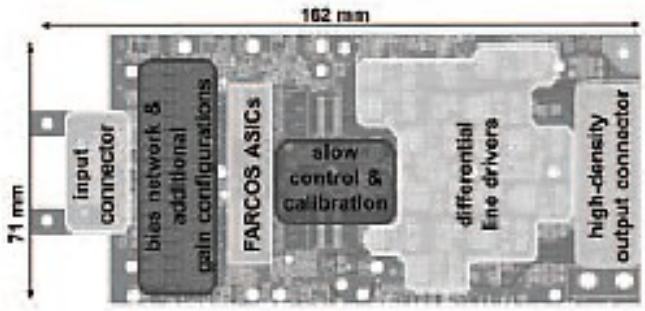

Figure 21: Layout of the 10-layer PCB that houses 2 FARCOS ASICS and reads out 32 + 2 detector channels [GUA21].

Some tests in the electronic laboratory have provided preliminary results about the energy resolution, for example: by coupling the frontend with a DSSSD (300 μm thick), the energy resolution results about $25\ keV\ FWHM$ using a three-pick alpha

source in a full-scale energy range of $100\ MeV$. Furthermore, about the rise time (in the interval of 20% - 80% of the time signal), it gives the following values: 10 ns for the 300 μm thick DSSSD, 6 ns for the 1500 μm thick DSSSD, 19 ns for the CsI(Tl) + photodiode system. The preamplifier is designed with a specific structure, in order to improve the noise performance and the stability. The calibration of the entire system is favoured by a dedicated circuit and a microcontroller placed on the slow-control board, in order to ease its mounting and the data acquisition.

During the CHIFAR experiment, in addition to the detectors, the experimental configuration also included other components, such as a custom-designed vacuum flange with interconnections for two clusters, for the vacuum side and the air side, the differential to single ended antialiasing amplifiers (256 channels per unit, for DSSSDs output signals), and finally the GET acquisition system. A schematic representation of this chain is shown in Fig. 22. The main power system was equipped with different bias boards: individual channels per telescope were used for the high voltages, while low voltages were jointly provided to two telescopes. The modular structure allowed a power air board driving four telescopes, *i.e.* bias and slow control. The FARCOS DAQ is based on GET electronic. This means that an ASAD (*i.e.* **A**GET **S**upport for **A**nalog to **D**igital) houses 4 AGETs (*i.e.* **A**SIC for **GET**, each includes 4 channels for noise measurement + 64 channels connected to external inputs); each COBO (COllection BOard) controls 4 ASADs, for a total of 1024 digital channels. The trigger (MUTANT) is based on three levels: multiplicity, trigger and time. Finally, the VME DAQ, VME-GET coupling, Data Analysis software for COBOs and VME, and the

general data merging were developed at INFN Sezione di Catania [ACO19]. A schematic overview of these GET components is shown in Fig. 23 [POL18].

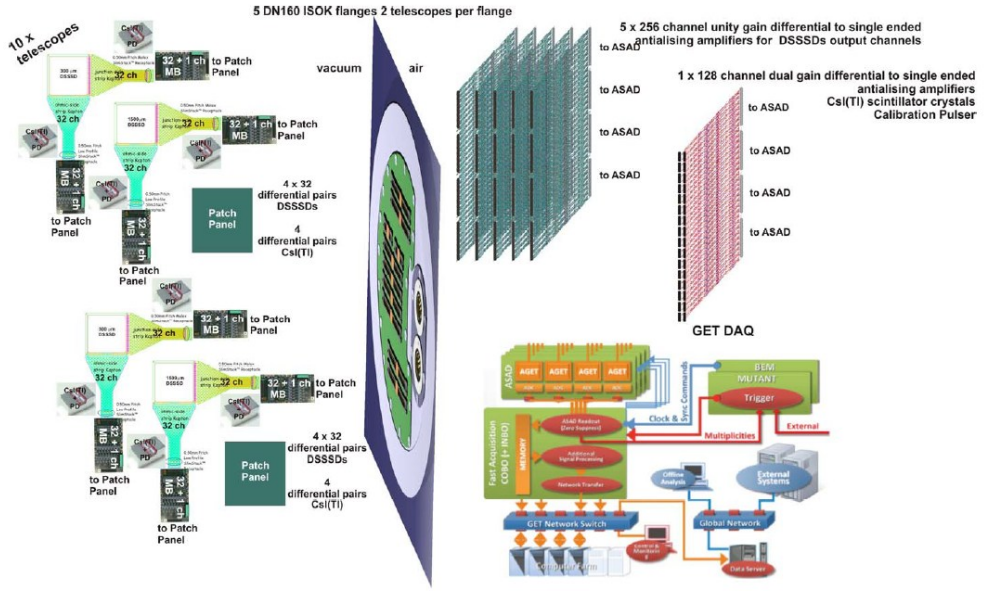

Figure 22: Schematic representation of the FARCOS configuration used in the CHIFAR experiment, including the array detectors, the frontend electronic, the differential to single ended antialiasing amplifiers, and finally the GET acquisition [ACO19].

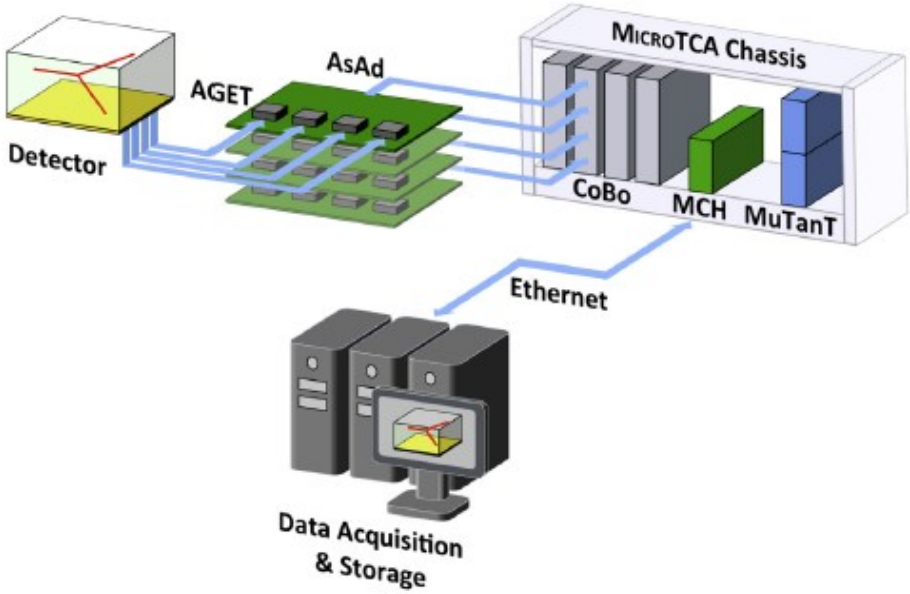

Figure 23: Schematic configuration of the GET system connections [POL18].

1.3 The GET electronic.

The FARCOS data acquisition is based on the GET electronic [POL18, POL12], featuring 12-bit resolution of the analog-to-digital conversion with a frequency up to 100 MHz, and a custom dual gain amplifier developed by INFN-Sezione di Catania that feeds the signals from the fronted motherboard to the GET system.

The General Electronics for TPCs (GET) was designed as a versatile and comprehensive electronic setup and data acquisition system for nuclear physics instrumentation of up to 33792 channels. The employment of radioactive beams has required the development of experimental methods in order to extract spectroscopic information and to study the reaction mechanisms of the nuclear collisions. The main aims focus on the reconstruction of the phase space with high energy and angular efficiency, and on the capability to identify the detected particles. The experimental setup is usually characterized by the use of different types of detectors around the target, placed in a vacuum chamber: this means that the number of channels must be increased. It is essential to realize a system featuring by portability and that allows calibration for the experiment in a few days/weeks. The GET architecture system is based on:

- a versatile ASIC with several modes of acquisition
- a 256-channel frontend card, including the analog-to-digital converter (ADC)
- a data concentration system, including the FPGA (Field Programmable Gate Array), which improves the rate of the data acquisition
- a 3-level trigger (MUTANT).

The frontend cards ASAD (ASIC and ADC) house four designed 64-channel AGET + ADCs. The ADC is in continuous read mode to trigger module MUTANT via the COBO (see Fig. 23). ASAD also permits to monitor the temperature, the power supply voltage, in case of malfunction.

Originally, GET was created for various types of TPCs, in their different configurations and employments, such as gas-filled detectors or gas amplifiers. In particular, a wide use of these detection tools concerns the physics of the Equation of State (EoS) and the nuclear particle spectroscopy. In recent years, the GET electronics has also been set up for the coupling with Silicon detectors, such as DSSSD, and scintillator, such as CsI(Tl).

The powerful of GET is the capability to sample the signals to reconstruct time, position and energy loss of the particles. The innovative performances, such as the high versatility and the compactness, make the GET system the ideal solution for FARCOS.

1.4 The DualGain amplifier technology.

A new high-frequency programmable multichannel amplifier technology is under improvement for the CHIMERA multi-detector and FARCOS correlator [SAC25].

Currently, the GET electronics allows to cover a dynamic range of $0 - 700\,mV$ and, as already explained, the input signals are digitized at 12 bits. Unfortunately, these features are no longer appropriate for the dynamic range covered by FARCOS telescopes. The main aim becomes to develop a more complex digital ACQ architecture, according to the high granularity and the high energy and angular resolution of the involved detectors.

The DualGain system was initially designed to process the CsI(Tl) signals readout by CHIMERA, then it was extended for the CsI(Tl) crystals of FARCOS. The offset input signal is adapted to the ASAD card and then the DualGain module duplicates it, with two independent gains for each copy of the signal. This means that the dynamic range can be chosen appropriately.

A single DualGain module consists of 64 channels digitally PGA (Programmable Gain Amplifier), with seven gain values available for a 16-channel group (see Fig. 24). Three microcontrollers check the slow control, the signal parameters setting and the user remote communications. The module can be used both as an amplifier and as an attenuator of the signal, and the offset can be adjusted in the range of $0 - 2000\ mV$. Thanks to the slow control, the temperature of the module can be monitored, and also the microcontrollers can turn off the PGAs in case of malfunctions.

In the configuration used for the CsI(Tl) crystals of CHIMERA, each ASAD card is connected to two DualGain modules, corresponding to 128 channels of the DAQ system. The DualGain system has been also tested for FARCOS arrays. The main advantage concerns the possibility to coupling FARCOS with other 4π detectors, also in other laboratories in the world. In fact, the DualGain allows to modify the dynamic range of the DAQ according to the nuclear physics investigations of one specific experiment.

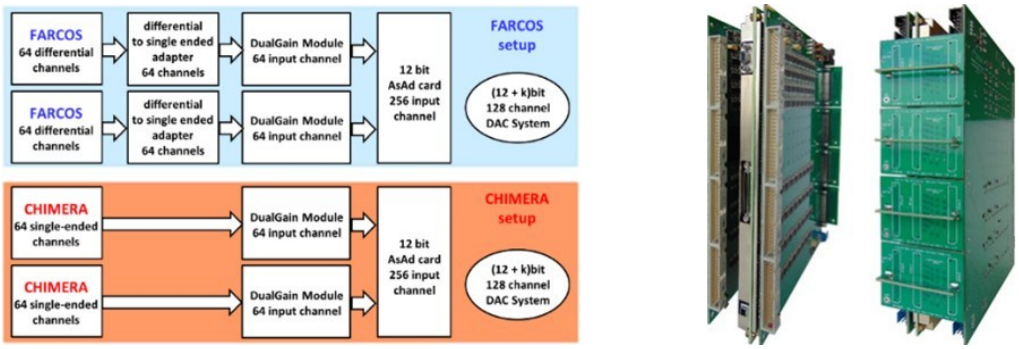

Figure 24: Schematic explanation of the DualGain structure for FARCOS and CHIMERA (on the left); DaulGain system with ASAD card connection (on the right) [SAC25].

2. *Features of CHIMERA multi-detector.*

In the CHIFAR experiment, carried out at INFN-LNS in November 2019, the setup consisted of the 4π CHIMERA multi-detector coupled to 10 telescopes of the FARCOS correlator. This coupling allowed to maximize the main features of the two detection systems:

- the high energy and angular resolution of FARCOS make it an appropriate tool for intended research, in particular for the identification of the IMFs produced in the HICs
- CHIMERA promotes the study of correlations among IMFs and light charged particles produced in the nuclear reactions, thanks to its high granularity and angular coverage, moreover, thanks to the high performances of CHIMERA is possible to characterize the reaction event by means of the global variable measurement.

The Charged Heavy Ion Mass and Energy Resolving Array (CHIMERA) [PAG04, PAG12] is engineered to provide a total charged particle energy and angular measurement from an HIC at Fermi energy having a complete 4π angular coverage surrounding the

target. This extensive array is composed of 1192 detector modules working in double energy dynamics. Each module operates as a telescope, coupling a 300 μm thick Si-detector with a CsI(Tl) scintillator; then, an integrated photodiode converts the light emitted by the crystal into an electronic signal, enabling data acquisition. The active area of each CsI(Tl) scintillators is about $50 \times 50\ mm^2$, while their thickness is not uniform; it decreases with the increasing of its polar angular position, becoming thinner at larger angles. For instance, the scintillator is 12 cm thick within the 1°-30° polar angle range, while it is reduced to a 3 cm in the 142°-176° polar range, the region where low energy particles are more expected. In fact, beside to measure their energies, the CsI(Tl) role is to fully stop the detected charged particles.

The first stage of the detection module employs Silicon (Si) detectors [PAG04, PAG12], chosen specifically for their features concerning to energy and time resolution and fast signal collection (approximately 10 ns in a 300 μm thick detector). These characteristics are connected to silicon's intrinsic material properties, including its high density (2.33 g/cm³) and the minimal energy required to generate an electron-hole pair (3.6 eV). In order to maximize the coverage of the 4π solid angle, each CHIMERA Si-detector has a trapezoidal shape. While their thickness remains a constant 300 μm, their specific geometry adjusts according to their placement within the device. Furthermore, a thin 300 Å layer of aluminium covers both the front and back sides, which serves to improve electrical contacts and thus optimize the detector's time response.

For the second stage of the detection unit, CsI(Tl) crystals are used [PAG04, PAG12]. Their front side was covered with a reflecting foil of aluminized Mylar. In order to ensure optimal charge collection, the crystals' lateral and rear sides were coated with a Teflon layer, while the front face received an aluminium foil coating: the crystals were wrapped in a Teflon layer $150\ \mu m$ thick and then coated with $30\ \mu m$ thick aluminium foil. These scintillators produce light when struck by particles, and this light is subsequently converted into a current signal by integrated photodiodes. The primary role of the CsI(Tl) is to fully stop and measure the residual energy of particles that pass through the initial Si-detector stage. The scintillation signal generated by the CsI(Tl) crystals has distinct "fast" and "slow" components. These components are valuable as they correlate with the specific energy loss, and consequently, the energy, charge, and mass of the incident fragments. The choice of CsI(Tl) was driven by its robustness against radiation damage, its positive light response, and the high density of the material (4.51 g/cm^3), which allows for a thinner detector design while still effectively stopping high-energy charged particles. A key property of these scintillators is their non-linear light response, meaning the light signal is not simply directly proportional to the energy loss but changes depending on the specific energy loss of the different nuclear species (quenching effect). Nevertheless, CsI(Tl) crystals are recognized as ideal detectors for achieving precise isotopic identification through the Pulse Shape Discrimination (PSD) technique. The photodiodes, measuring 300 μm in thickness and having an active area of $18 \times 18\ mm^2$, were coupled to the back side of the crystals by means of a thin silicon grease layer.

The 1192 telescopes used in the CHIMERA multi-detector are organized into 35 rings. These rings are divided into two main sections: the sphere and the forward part. The latter 17 rings are precisely coupled to form a sphere with a radius of 40 cm. The initial 18 rings, constituting the "forward part", are positioned in front of this sphere, in a cylindrical geometry along the beam axis.

The entire apparatus works inside a vacuum chamber and has a total length of 4 m. The forward part of CHIMERA covers a polar angle range of 1°-30°. The spherical section then extends the angular coverage from 30° to 176° (see Figs. 25-28).

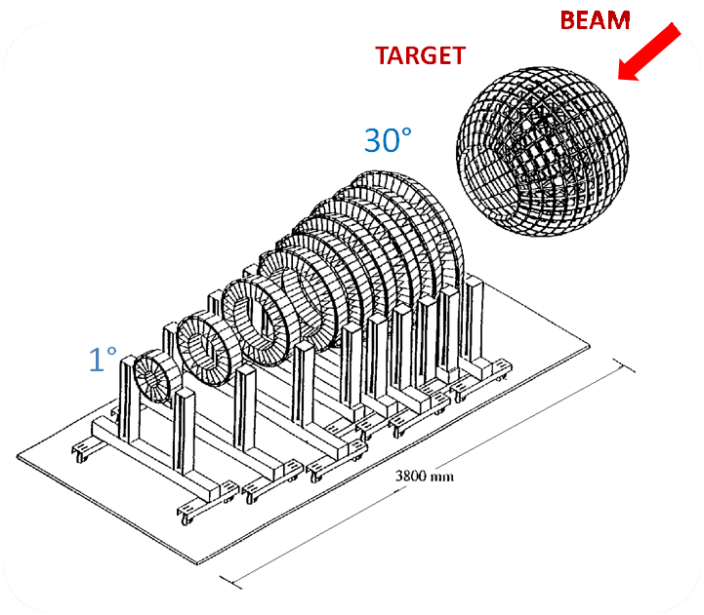

Figure 25: Schematic representation of the CHIMERA apparatus, with specification of its geometry and angular coverage.

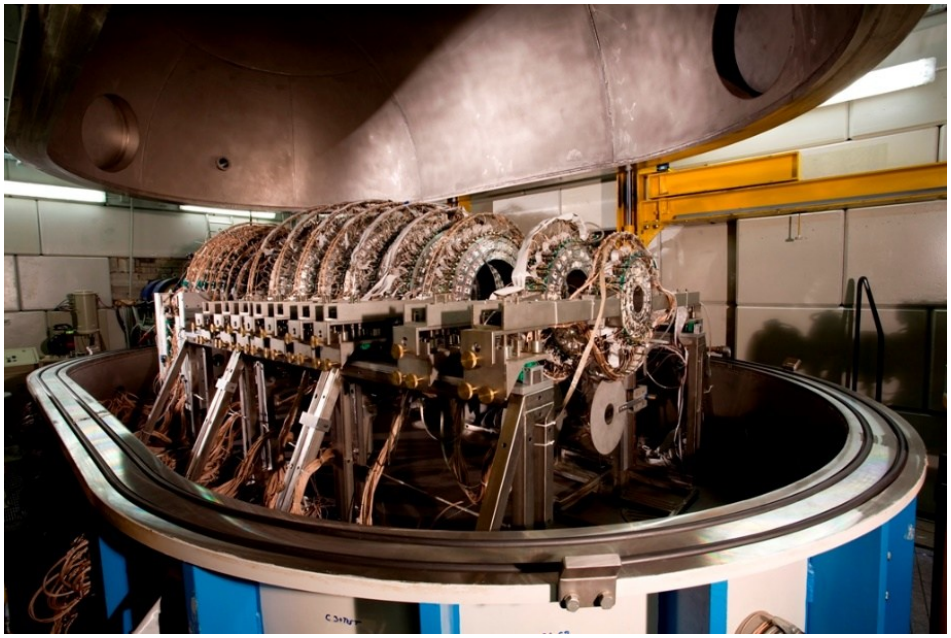

Figure 26: A photo of the forward part of the CHIMERA multi-detector, inside the vacuum chamber [webCHI].

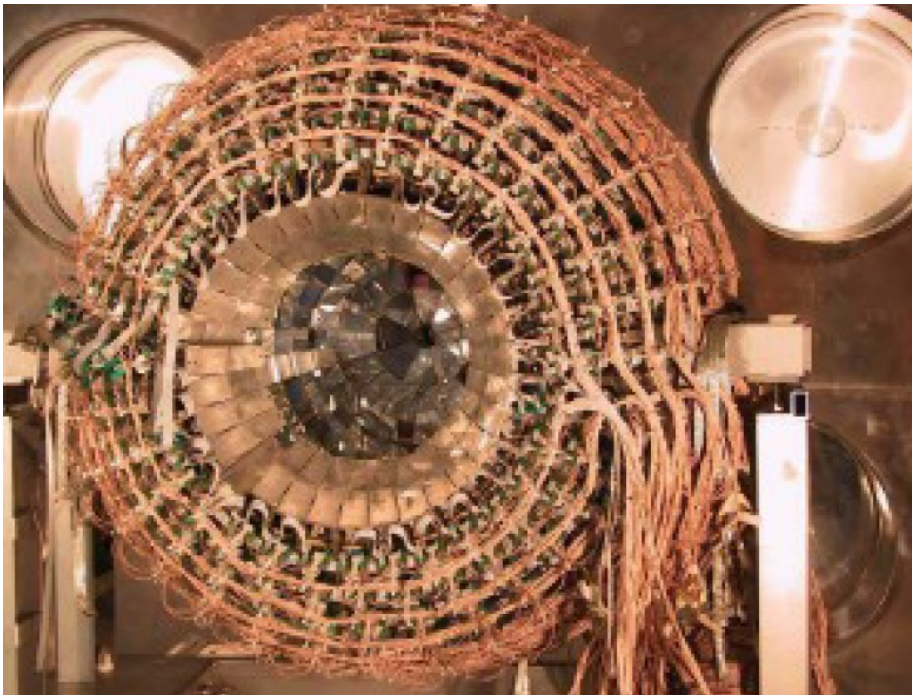

Figure 27: A photography of the sphere of the CHIMERA detector [webCHI].

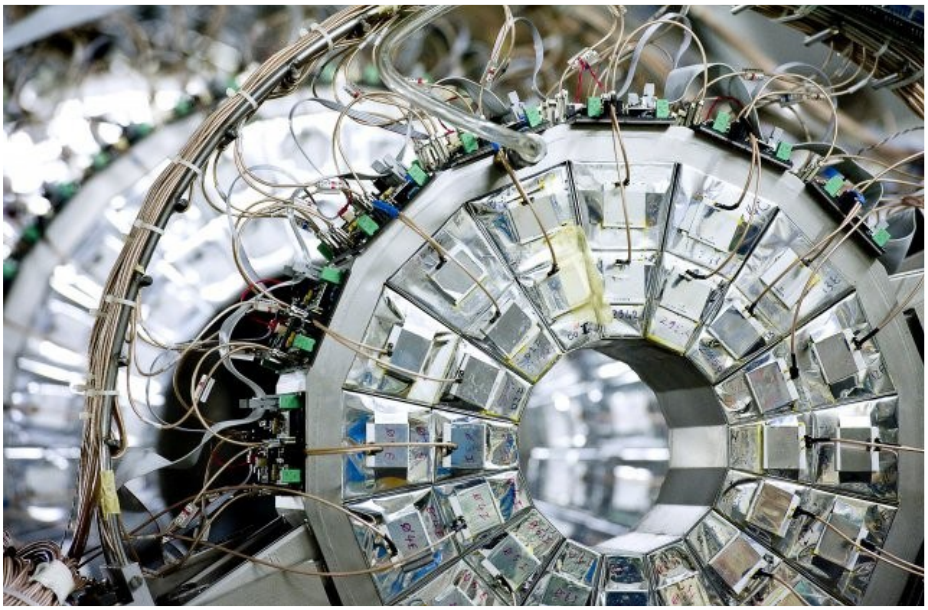

Figure 28: A picture of a wheel of CHIMERA.

CHIMERA's most crucial aspect is its physical and geometrical design [PAG01, PAG04, PAG12]. The above-mentioned configuration is responsible for the detector's high granularity and impressive solid angle coverage, encompassing approximately 94% of the total 4π. These features are fundamental to the multi-detector's performance, enabling the application of particle identification methods. In particular, three different identification techniques can be applied simultaneously: the ΔE-E technique allows the identification in charge of the Heavy Ion fragments and for isotopic identification of IMFs with atomic number $Z < 10$; instead, their velocity is measured by the connection of the ΔE component with the Time Of Flight (TOF) signal, the latter obtained by comparing the timing of the detector signal and the timing of the high frequency from the cyclotron; finally, the PSD method is used to identify the LCPs stopped in the CsI(Tl) scintillators. Furthermore, an in-depth study of the shape of signals produced in Si detectors was conducted, performed by both conventional and digital pulse shape acquisition.

The main goal of this investigation was focused on further advancing toward the charged particle discrimination with PSD method applied on Silicon detectors. Considering the front-end electronics, the CHIMERA multi-detector was upgraded to measure the rise-time of the signals, in order to achieve the mass and charge identifications for reaction products stopped inside the Si stages: it was called the E-rise-time technique [POL05-ALD04b]. This means that the reconstruction of events is characterized by an exceptional accuracy. In Figure 29 an overview of the identification methods of CHIMERA was summarized. The CHIMERA beamline was also equipped with a Micro-Channel Plate timing system and a microstrip silicon tagging detector: exotic beams produced by projectile fragmentation of a primary beam, delivered by the LNS-CS accelerator, can be identified applying the ΔE-TOF technique. Concerning to the scientific program of CHIMERA, this characterization of the events encouraged the study of nuclei with large isospin asymmetry, in order to determine the evolution of the reaction mechanism for both binary and compound nucleus reactions.

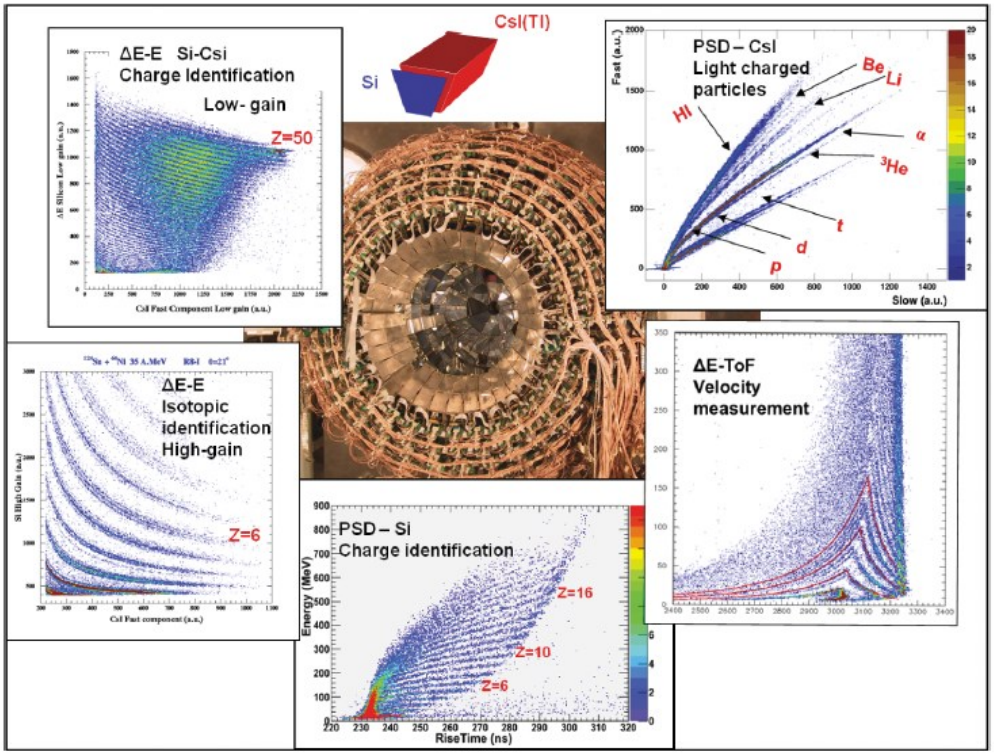

Figure 29: An overview of the identification methods adopted by the CHIMERA multi-detector [PAG12].

According to the two types of detectors involved, the CHIMERA multi-detector employs two distinct, yet functionally similar, electronic chains [RUS23] to process the current signal generated by photodiodes, ultimately feeding it into a data acquisition system.

For the Si-detectors, the output signal is first sent to a Charge Preamplifier (PAC). The PAC performs initial amplification and impedance matching, producing a signal directly proportional to the charge produced by the impinging particle in the detector. This signal then proceeds to an Amplifier (AMP), which has two sections: one for providing an energy output and the other one for providing the timing outputs and a multiplicity signal. The energy signal is subsequently processed by a Charge Digital Converter (QDC). Concurrently, the temporal signal is handled by a Constant Fraction

Discriminator (CFD), whose logic output serves as the start signal for a Time to Digital Converter (TDC). In fact, in the last section, the signal is differentiated by a high-pass Capacitive-Resistive (CR) filter and then passes to the timing gain section. Depending on the operating mode of the CHIMERA multi-detector, the maximum gain is used to lower the detection thresholds. The timing output is shared into three components:

- The first allows to evaluate the over-threshold condition and provide an appropriate signal to control the outputs of the module.
- In the second, the signal is again differentiated by a high-pass CR filter, with a differentiation time of $50\,ns$; then, it is processed by a CFD with a typical fraction of 30% and a delay of $30\,ns$. The logical signal is used as the start signal, while the stop signal is obtained from the cyclotron Radiofrequency (RF). The TDC output, converted in ns, gives a measure of the arrival time of the detected particle. The 30% CFD is also used to measure the event-by-event hit multiplicity.
- Finally, the signal produced by the time gaining section is processed by a CFD with a typical fraction of 80% and a delay of $150\,ns$; again, considering the start and stop signals as above, the TDC output in ns allows to calculate the rise-time of the signal, which is expressed by the difference of the last two extrapolated components: $RT = t_{30} - t_{80}$.

The Data Acquisition System collects both the energy and time signals.

The electronic chain for the CsI(Tl) detectors also incorporates a PAC and an AMP. However, it utilizes two QDCs and a Stretcher

to handle two distinct energy outputs. The first energy signal, after appropriate shaping and a high-gain (x10) amplification, is directed to a QDC that integrates the signal's tail to extract the "slow" component. The second energy output is stretched to its maximum amplitude before being passed to another QDC to obtain the "fast" component.

Schematic representations of CHIMERA's electronic chains used to process signals produced by the Silicon detectors and the CsI(Tl) scintillator are provided in Figure 30.

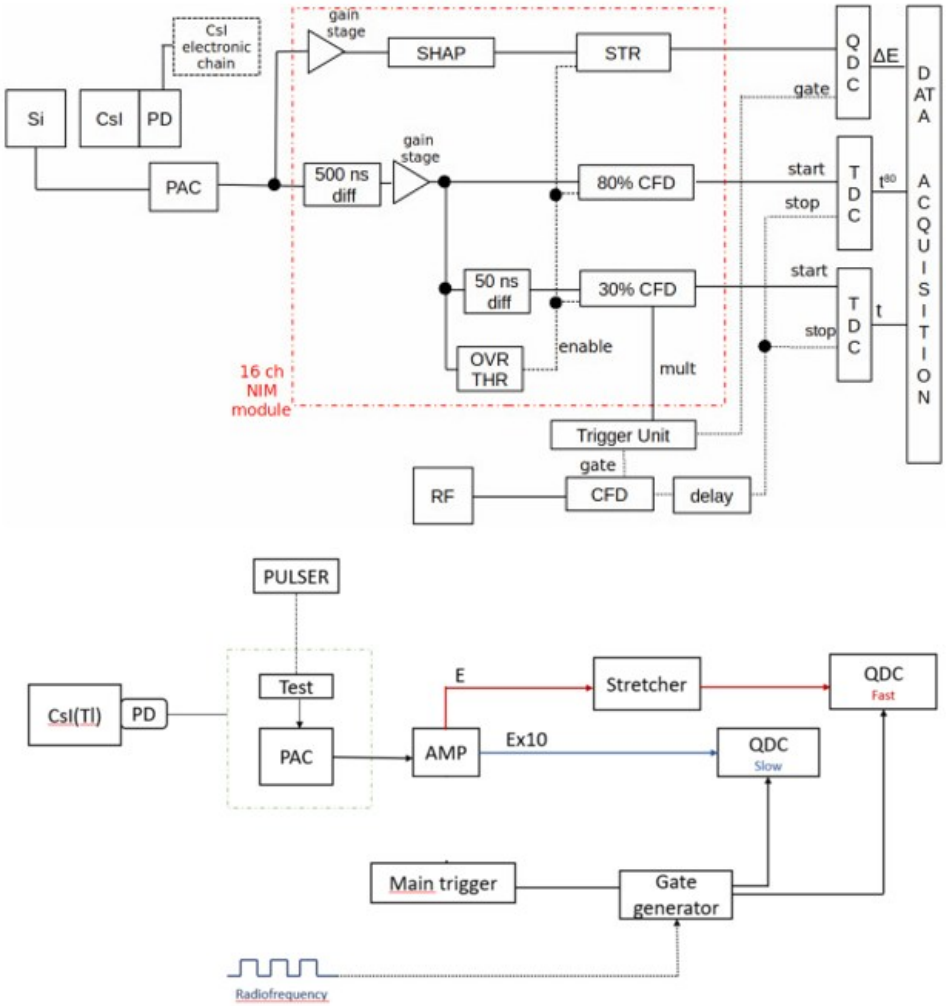

Figure 30: Schematic representation of the electronic chains used in the CHIMERA apparatus to process signals produced by Si detectors (upper scheme) and CsI(Tl) scintillators (lower scheme) [RUS23].

The 4π CHIMERA multi-detector was built to improve heavy-ion research in the intermediate energy range. Its first experimental use, involving a partial setup, occurred in 1997: the first ring of the detector, including only 32 telescopes, was coupled with the INDRA multi-detector at GANIL in France. Then, in 1999, a significant portion of the device was installed at LNS-INFN in Catania and used in the experimental setup of the REVERSE experiment [DEF14]. In the following years, the detector was completed and installed along one of the beam lines of LNS-INFN. The main aims of the first experiments that included CHIERA in the setup were the investigation of some important aspects of the nuclear physics, *i.e.* the IMFs emission and the isospin dependence in the nuclear multifragmentation, so in the collision mechanism at intermediate energy. The REVERSE experiment chosen some HICs for different physics goal, such as ^{124}Sn+^{27}Al and ^{124}Sn+^{64}Ni at $25\ AMeV$ and $35\ AMeV$ to study the creation of cluster states, ^{112}Sn+^{58}Ni and ^{124}Sn+^{64}Ni at $35\ AMeV$ to investigate the isospin role in the reaction mechanisms and the dynamical fission process, production of exotic nuclei, evolution of supernovae and structure of neutron star. All these nuclear reactions were studied in reverse kinematics, thanks to high granularity of CHIMERA, with great advantages like a strong focusing effect and the relatively high kinetic energies of the emitted particles. The data analysis highlighted a very good energy and time resolution (around 1-2% and 1 ns, respectively) and the flexibility of the acquisition system of CHIMERA, which allowed to set different trigger conditions. Imposing some constraints on the multiplicity of charged particle, events with the total charge close to the projectile charge could be well reconstructed; therefore, for about 25% of these

events with the primary PLF, also TLF were detected in coincidence with the PLF. The experimental results had been compared with theoretical predictions based on the BNV transport theory, filtered according to the geometrical configuration of the detecting system: basic features of the PLF, TLF and IMF region were perfectly in agreement, and also the IMF charge distribution was quite accurately predicted. The capability of CHIMERA to detect fragments in a wide range of kinetic energies, ranging from slow moving TLF up to fast moving PLF (as already discussed and shown in Fig. 3), was one of the most important innovations achieved by CHIMERA among 4π detection systems. In particular, these features allowed to develop a new investigation method, based on the evaluation of fragment relative velocities in a three-body kinematical analysis, in order to calibrate the time scale of the emission of IMF produced in semi-peripheral collisions. The time scale calibration was firstly applied to the ^{124}Sn+^{64}Ni reaction at 35 $AMeV$. Data analysis highlighted that light IMFs ($Z \lesssim 10$) emitted in semi-peripheral collisions were predominantly emitted from the dynamically expanding neck region. The method was very interesting for establishing the hierarchy effect in the emission time of IMFs: increasing IMF's charge the corresponding emission time scale also increases to values as large as 300 fm/c or more, typical for those IMFs originating from nearly sequential asymmetric splitting of a primary PLF into two massive fragments. Finally, time scale as a function of the isospin dynamics was also investigated with CHIMERA, in order to probe the isospin diffusion as a function of the density gradient: it was observed that fragments dynamically emitted from the initial phase of the reaction

show larger values of the isospin asymmetry, indicating a favoured emission of more neutron-rich nuclei. [PAG01, PAG04, PAG12].

CHAPTER 3

Latest results from data analysis related to the FARCOS correlator, concerning to the CHIFAR experiment.

The main experimental goals of the CHIFAR experiment, already extensively explained in the first chapter of this thesis, can be summarized in three points:

- LCPs, IMFs, TLFs and PLFs detections, in order to identify the final products of nuclear collisions
- the investigation of the IMFs emission mechanism, that means dynamical or statistical processes, in terms of their probabilities
- the role of the isospin degree of freedom ($i.e.$ the ratio N/Z) in HICs, with final aim of linking it to the symmetry energy and the asy-stiff/soft parametrization of the asymmetric nuclear matter EOS.

The choice of the experimental setup, based on the coupling between 10 telescopes of the FARCOS correlator and the 4π CHIMERA multi-detector, as shown in Fig. 1, encouraged the investigation of the six nuclear reactions at 20 $AMeV$ incident beam energy. This lower energy with respect to the previous REVERSE and InKiIsSy experiments (both carried out at 35 $AMeV$) will allow the comparison of the data analysis results between the two beam energies and make a kind of nuclear systems data systematics as a function of isospin, energy and size.

The data analysis was focused on the data collected by the two first stages of the FARCOS telescopes, that means the two DSSSDs

(300 μm and 1500 μm thick respectively). In the following paragraphs of this chapter, the procedure concerning the energy calibration and the evaluation of the energy resolution of the Si stages will be discussed. A timing analysis was mandatory in order to applicate the so-called "pixelation technique": the correct position to each particle detected by FARCOS could be assigned. Finally, the ΔE-E matrices of each telescope were studied during the IMFs identification phase.

1. *Energy calibration of the DSSSDs: the "punching-through" technique.*

In the first step of the data analysis, the first two stages, *i.e.* the DSSSDs, of each FARCOS telescope used in the CHIFAR experiment were energy calibrated. The so-called "punching-through" technique [ZAG25, ZAG25b] was applied to the two-dimensional matrices involving the electronic channels of the two Si detectors with thicknesses of 300 μm and 1500 μm respectively.

The initial incident energy E_i of the impinging particles is unknown. The calibration technique works as it follows: the particle punches through the first stage of a FARCOS telescope, that means the Si-300 μm thick and a certain amount ΔE of the incident energy is lost. Afterwards, the particle has to stop at the end of the second Si detector - 1500 μm thick. At the end of the path (*i.e.* 1800 μm) in the two DSSSDs, if the remaining energy is zero ($i.e\ E_f = 0\ MeV$), the technique hypotheses are satisfied and the particle incident energy E_i is known (see Fig. 31) When this particular condition occur, it is possible to individuate an energy calibration point.

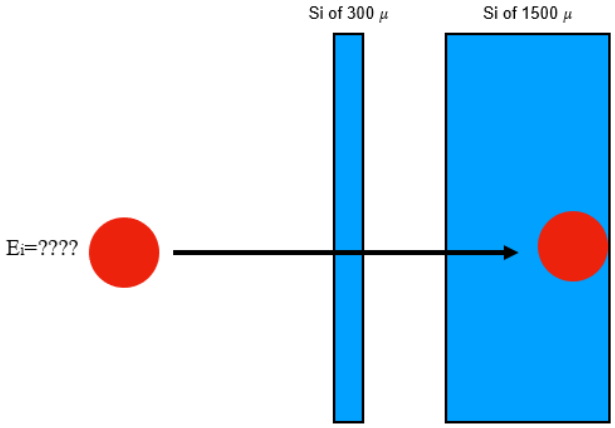

Figure 31: Schematic representation of the energy loss of a particle that stops in a total path of 300 μm + 1500 μm thickness of Si.

For each FARCOS telescope, the two-dimensional matrices of the electronic channels were studied. The energy deposited in the strip of the first DSSSD, as a function of the corresponding energy deposited in the strip of the second one, generated some hyperbolic curves, such as "banana plots" in channels, not energy calibrated yet. According to the Bethe-Bloch formula, the energy loss of the incident particles in a material is proportional to the square of the particle's charge and to the mass (for no relativistic particles having $E/A < 100\ MeV/A$). Consequently, the obtained hyperbolic trends can be associated to the atomic number Z of the particles detected within the two DSSSDs of FARCOS telescopes. The final goal is to be able to identify the incident ions in the detector, in terms of their charge and mass: the perspective involves a good identification for the final isotopes between $2 \leq Z \leq 20$, besides, of course, to measure their position and energy with high resolution.

Considering the two-dimensional matrices of the electronic channels for each couple of DSSSDs, some experimental deviations from the expected behaviour have been highlighted. In particular, at the end of specific hyperbolic curves, some snap backs events

associated to the detected particles can be observed. Specifically, in the 2D plots, these tails are more evident in correspondence of the ^{7}Li, ^{7}Be and ^{9}Be associated "banana" lines, as can be observed in the upper left panel of the Fig. 32. This means that condition relating to the final energy equal to zero at the end of the total path inside the two DSSSDs was violated: the range of the impinging particle is larger than 1800 μm. Conversely, the incident particles are passing through the second Si stage and lose their remaining energy in the third stage of the telescope, *i.e.* CsI(Tl) scintillators.

Applying the "punching-through" technique begins by selecting the electronic channels corresponding to the ^{7}Li, ^{7}Be and ^{9}Be snap backs and use such electronic channel for the calibration fits of each telescope. Assuming the ion completely arrested in 1800 μm of Si, using the LISE++ software [LISE], the total kinetic energy released, and then the two contributes lost in each DSSSD stage by each fragment, were evaluated (see Tab. 2). The linear best fit has allowed to extrapolate the calibration parameters for each FARCOS telescope. This explained technique was applied to the front sides of the DSSSDs (first and second stages). The corresponding back side strips were calibrated in the following step, using the previous front strip side already calibrated.

Particle	Energy lost in Si-300 μm	Energy lost in Si-1500 μm	Total kinetic energy released
^{7}Li	13,52 MeV	125,43 MeV	138,95 MeV
^{7}Be	18,45 MeV	172,75 MeV	191,20 MeV
^{9}Be	20,74 MeV	192,76 MeV	213,50 MeV

Table 2: Energy lost in the two stages of Si-detectors of the telescope n° 5, and total initial energy for ^{7}Li, ^{7}Be and ^{9}Be particles, calculated by LISE++, according to the punch-through technique.

Once the three energies are get, the calibration parameters can be extrapolated, assuming a linear function as the energy response E of the Si detector in units of MeV, *i.e.* $E = a * channel + b$ where a is measured in MeV/ch and b in MeV. The obtained linearity results very good, with a value of the parameter $R^2 = 0.99$ in the case of the fifth telescope, for example. Moreover, a constraint has been also put in order to include in the fit a zero value fourth point in the axis origin, according to the digital acquisition of FARCOS (upper right panel of Fig. 32).

The "punching-through" technique was implemented for all the strips, for a selection of six telescopes - the number 1, 5, 7, 8, 9 and 10 - employed in the CHIFAR experiment.

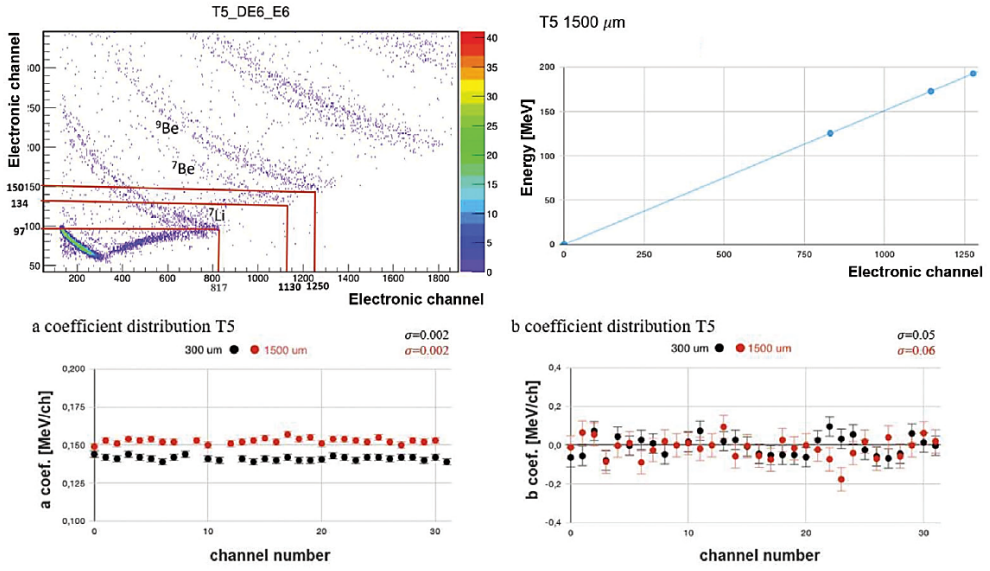

Figure 32: The "punching-through" technique is applied to the two-dimensional channel matrix of the front side of the fifth telescope, selecting three points corresponding to the ^{7}Li, ^{7}Be and ^{9}Be snap backs (upper lift panel). Calibration parameters are extrapolated from the linear best-fit of the same module (upper right panel). Comparison of the two calibration parameters, between the first and second DSSSDs of the telescope n° 5 (bottom panel) [ZAG25b].

A statistical analysis was applied to each telescope, in order to evaluate the errors associated with the calibration parameters values extrapolated from the linear best-fit. A good stability for the coefficients is well achieved, as it was verified from the comparison between the respective distributions of the parameters, for the first and second DSSSD of each telescope (see bottom panel of the Fig. 32, related to the fifth telescope as example). Furthermore, all the six telescopes calibrated using the method explained above were compared with each other. Regarding the angular coefficient a, which represents the preamplifier sensitivity, the trends of corresponding strips are quite similar, homogeneous and stable, for the two DSSSDs of all six telescopes. The comparisons are shown in the upper panels of Figures 33 and 34, for the 300 μm and 1500 μm thick Si detectors, respectively. The difference obtained for the first DSSSD stage of the telescope n.1 is due to the different ASIC preamplifier gain used in the measurements. For the second coefficient b, also a good agreement between the telescopes was achieved (shown in bottom panels of Figs. 33 and 34). As it is supposed in a digital acquisition, its value is close to zero within the error bars.

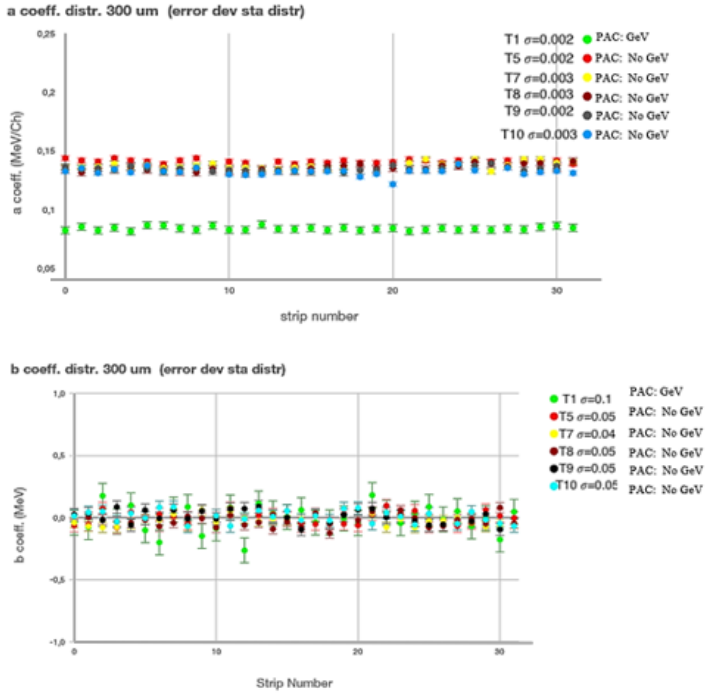

Figure 33: Comparisons of calibration coefficients distributions for six DSSSDs (300 μm thick) analyzed: error bars indicate standard deviations, according to the best-fit $E = a * ch + b$.

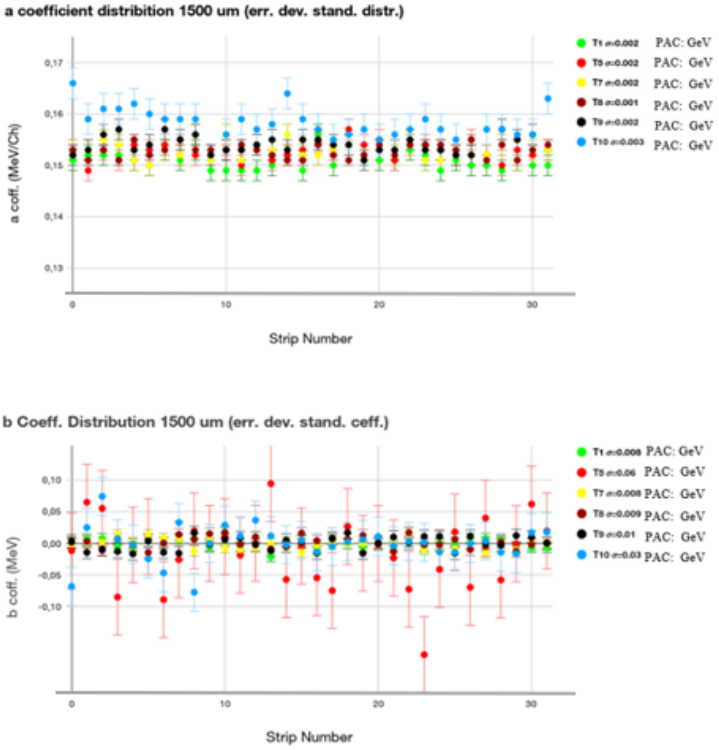

Figure 34: Comparisons of calibration coefficients distributions for six DSSSDs (1500 μm thick) analyzed: error bars indicate standard deviations, according to the best-fit $E = a * ch + b$.

DSSSD 300 µm thick	a mean value [keV/ch]	b mean value [keV]
T1	84.1 ± 0,3	-7 ± 1
T5	141.3 ± 0,3	-4 ± 9
T7	137.9 ± 0,3	-26 ± 7
T8	135.6 ± 0,5	-21 ± 9
T9	134.8 ± 0,4	10 ± 10
T10	132.5 ± 0,6	8 ± 9

DSSSD 1500 µm thick	a mean value [keV/ch]	b mean value [keV]
T1	151.0 ± 0,3	0 ± 1
T5	152.7 ± 0,3	-20 ± 10
T7	152.8 ± 0,3	-1 ± 2
T8	152.8 ± 0,2	-2 ± 2
T9	154.0 ± 0,3	0 ± 2
T10	154.8 ± 0,5	0 ± 6

Table 3: Mean values of the calibration coefficients for the six telescopes and for the two DSSSDs.

In Table 3 the average values of the calibration coefficients associated with each DSSSD of six telescopes studied are reported. The good agreement confirms the validity of the application of the "punching-through" technique for the energy calibration of FARCOS. In particular, the method allowed us to include the global information of a DSSSD for each telescope, which in principle should be the same for each strip, but is treated as an independent

electronic channel. The small differences observed could be explained by the coupling between the PAC and the different capacitances of the two DSSSDs.

Once the calibration procedure is completed, the statistics of the events collected by each strip of Si-detectors can be plotted in a single ΔE-E identification matrix for each telescope. Specifically, the two-dimensional spectra graph the energies from the 1500 μm thick Si-strips on the x-axis, while the y-axis represents the same measurement but related to 300 μm thick Si-strips. This means that the points in the plot have a pair of energy coordinates – (E; ΔE) – now measured in units of MeV thanks to the energy calibration procedure. For a more correct data analysis, the yields of the first and last strips of Si stages were not included in the statistics, in order to eliminate bad correlations due to the bending effects of the electric field.

Figures 35-37 below show some examples of ΔE-E matrices for the energy calibrated telescopes. The spectra contain the events accumulated during the CHIFAR experimental runs for the ^{124}Sn+^{64}Ni "neutron-rich" reaction, spanning a total of 60 hours of data acquisition. Analogue two-dimensional distributions were obtained for the other five reactions studied in the CHIFAR experiment.

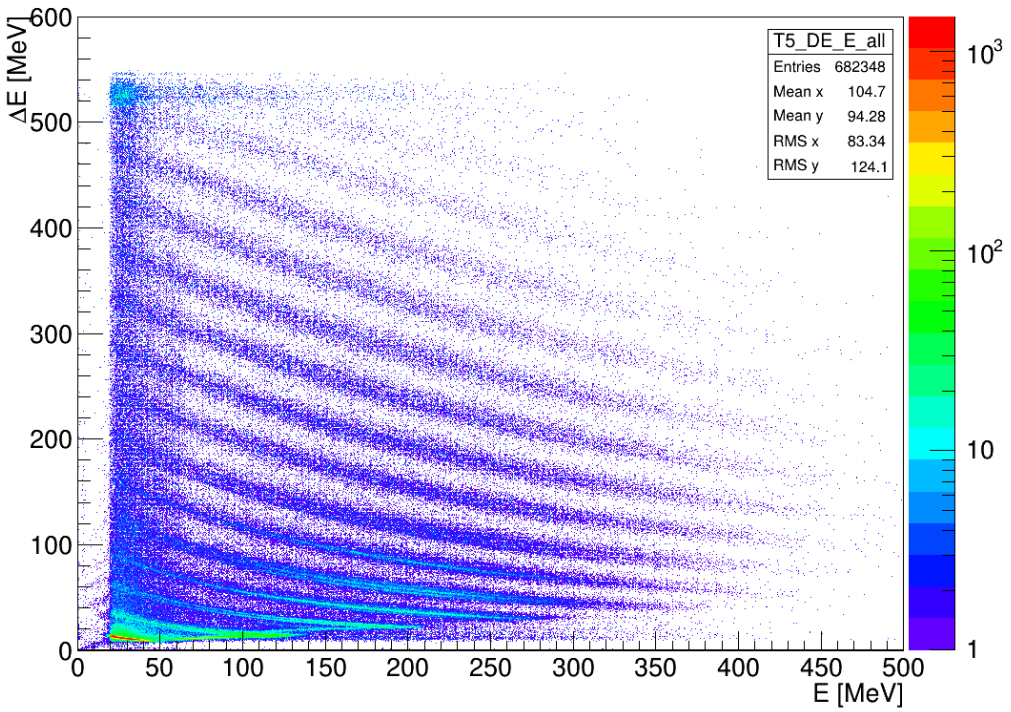

Figure 35: ΔE-E calibrated matrix for telescope n°5, relating to events acquired from the $^{124}Sn+^{64}Ni$ "neutron-rich" reaction.

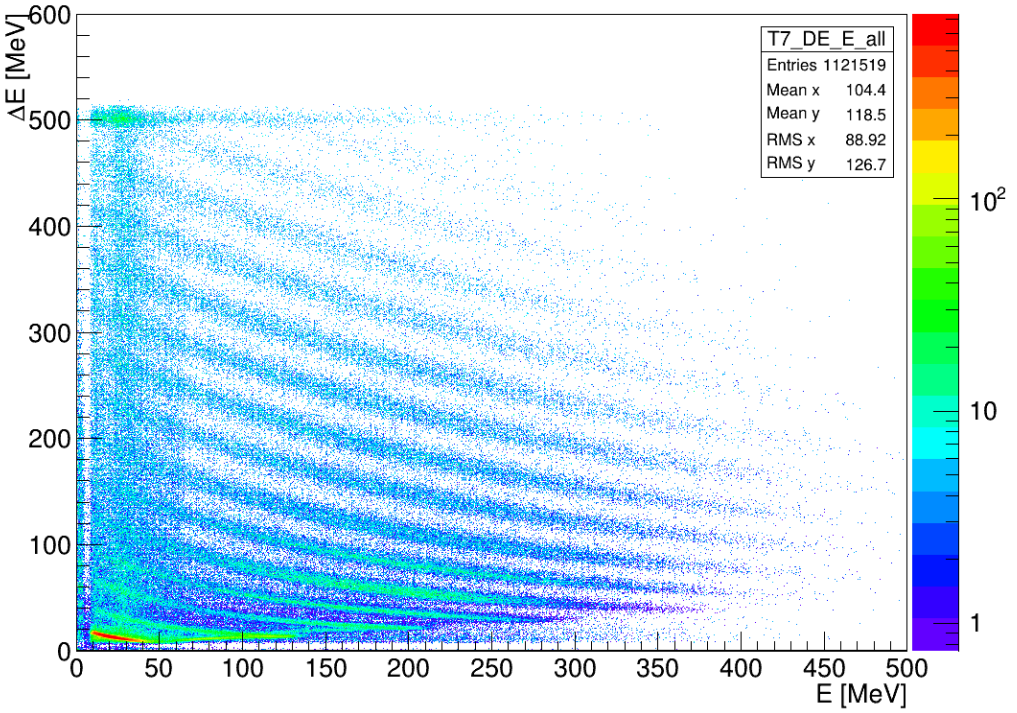

Figure 36: ΔE-E calibrated matrix for telescope n°7, relating to events acquired from the $^{124}Sn+^{64}Ni$ "neutron-rich" reaction.

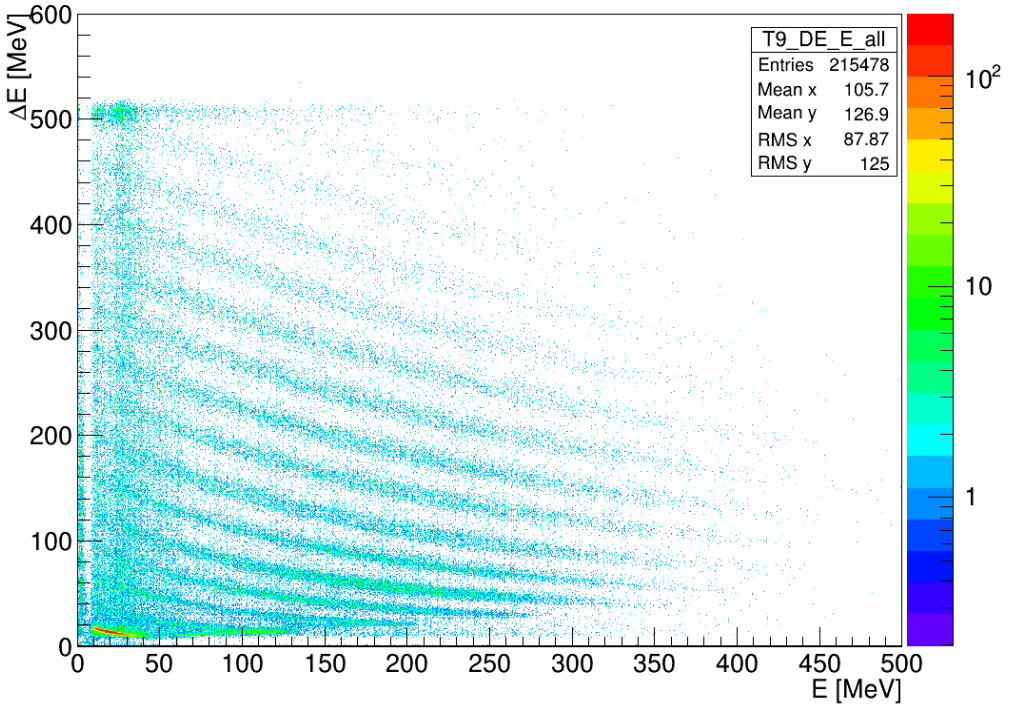

Figure 37: ΔE-E calibrated matrix for telescope n°9, relating to events acquired from the $^{124}Sn+^{64}Ni$ "neutron-rich" reaction.

2. *Evaluation of the energy resolution of both sides of the DSSSDs.*

FARCOS was designed to have high energy and angular resolution for reaction dynamics and nuclear structure studies. Its coupling capability with other 4π detectors allows the study of Heavy Ions reactions at intermediate energies and the identification of LCP and IMFs as final products. The second step of the analysis explained here was dedicated to the energy resolution evaluation of both sides, *i.e.* front and back sides of the two DSSSDs, for each FARCOS module [ZAG25, ZAG25c].

The analytical approach was based on a typical feature of Si detectors. Theoretically, they have to satisfy the linear

proportionality between the $FWHM$ and the square root of the energy released by the particle incident on the detector, which also means:

$$FWHM^2 = a \cdot E + b \quad (2)$$

Formula (2) explains the relationship between the energy resolution of the Si detector, expressed as the square of $FWHM$, and the mean value of the energy released, assuming that the statistical probability of the charge created inside of the detector is following a Poisson distribution. The two linear coefficients - a and b - represent the differential increase of the $FWHM$ as a function of the energy and the square of the electronic error of each detector, respectively.

Given the array structure of FARCOS telescopes, the estimation of the energy resolution of both sides of the DSSSDs involved the evaluation of their $FWHM$ as a total error, and its separation into two components, related to the electronic noise and to the intrinsic contribution of the detection system. During the CHIFAR experiment, some runs of three elastic scattering measurements were acquired: ^{16}O+^{197}Au at $85\ MeV$ beam energy and two ^{12}C+^{197}Au at 75 and $65\ MeV$. All three beams have been delivered by the Tandem accelerator housed at INFN-LNS. Considering the total energy of these beams, the evaluation of the energy resolution focused on the first DSSSD, which has a thickness of 300 μm. Indeed, the beam energies were not enough to punch through the first stage and reach the second one of the FARCOS telescopes.

Considering the front side strips of the DSSSD, the mean energy released in the first stage of each telescope was estimated from a Gaussian fit of the three elastic peaks. The procedure was accurately

performed strip by strip, acquiring the mean value of the energy and the sigma parameter of the fit (see Fig. 38); finally, the $FWHM$ was calculated.

In order to perform a high-level accuracy analysis, it was decided to consider the coincidence between one strip of the front side and not all 32 strips of the back side, choosing only a group of them taking into account for the angular spread of one strip that in some cases can be as large as 10° in the polar angle of the laboratory frame. After comparing the sigma deviations in the performance of Gaussian fits with several group of strips, the best conclusion was that the energy spread of the elastic peak in the angular region covered by 8 strips gives the minimum total error. Consequently, the 32 strips of each DSSSD were studied in 4 sets of 8 strips each: this means that each vertical strip of the front side was put in coincidence with 4 groups, each consisting of 8 horizontal strips of the back side.

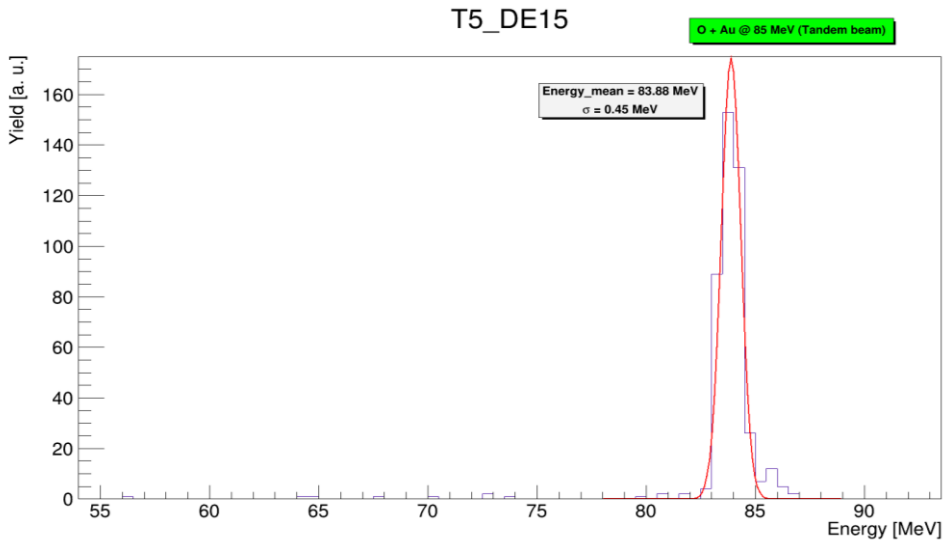

Figure 38: Histogram of the energy peak released on the strip n°15 of the first DSSSD of the telescope n°5; the front side single strip is in coincidence with 8 back strips, for $^{16}O+^{197}Au$ @ 85 MeV elastic scattering. From the Gaussian fit, the energy mean value and the sigma parameters are evaluated.

Once all the Gaussian fits were performed, for each front strip, for each telescope the average of the deposited energy and the $FWHM$ were calculated, relating to the three elastic scatterings. All quantities are accompanied by their respective absolute errors, calculated using the theory of error propagation. Therefore, as regards the estimate of the energy resolution of the DSSSDs, expressed as a percentage, it was determined by the ratio between the $FWHM$ and the energy mean, for each telescope.

The next step was about the evaluation of the two components of the energy resolution, as a measurement of the electronic noise and of the intrinsic contribution of the single detector. For each telescope analyzed, a linear fit was extrapolated from the three elastic scatterings, in order to verify the linear relationship expressed by the formula (2), typically for Si detectors. The plots obtained are shown in the Figure 39: the square of the evaluated $FWHM$ as a function of the energy mean value E is plotted, with the linear fit (red lines) and the associated errors (green lines). Finally, for each telescope, the electronic noise and the intrinsic detector error were calculated from formulas (3) and (4). Unlike for the electronic error, the intrinsic component depends on the specific reaction of scattering, because the total error of the telescope is different according to the beam energy of the three processes.

$$electronic\ error = \sqrt{b} * 1000\ \ [keV] \tag{3}$$

$$detector\ error\ = FWHM - electronic\ error \tag{4}$$

The overall results of the entire procedure described above, about the energy resolution of the front sides of the DSSSDs, are summarized in Tabs. 4-6 below. They are related to the three elastic scattering, and show the energy mean values, the $FWHM$, the energy resolution in percent, the electronic and detector components with their associated errors.

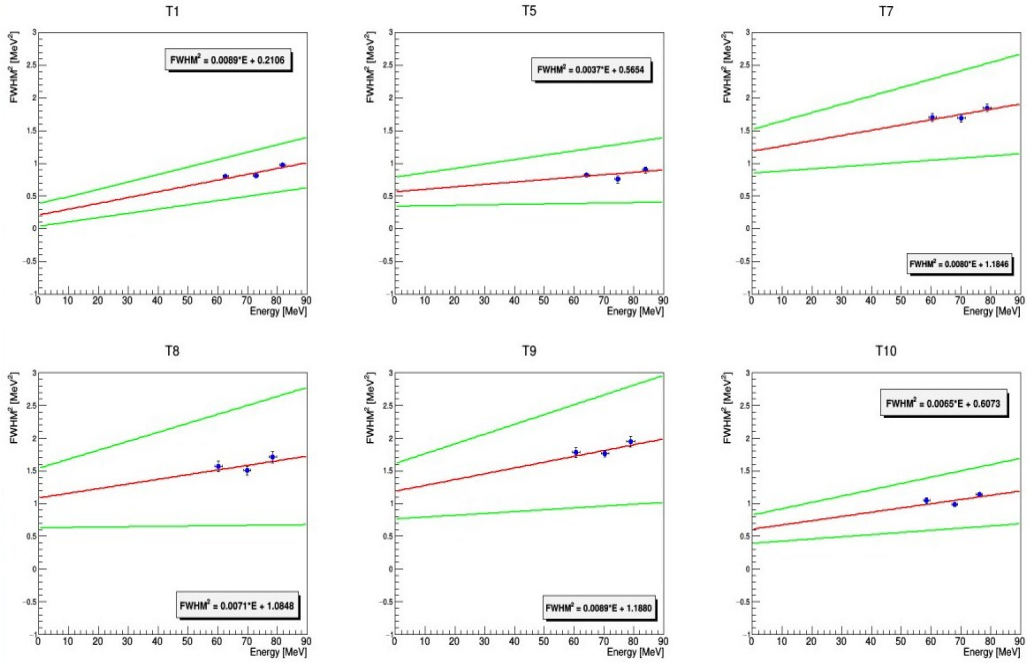

Figure 39: Experimental linear fits for the six telescopes analyzed: $FWHM^2$ of the three elastic scatterings are plotted as a function of mean energy, with statistical error bars. In each panel of the figure the value of the two fits parameters is reported. The red line represents the fit results; the green lines are the upper and lower limit of the fit considering for the error on the parameters as a result from the fit procedure.

Elastic scattering: $^{16}O+^{197}Au$ at 85 MeV							
Telescope	**Energy mean**	**FWHM (total error)**	**Resolution**	**Electronic error**	**Electronic error**	**Detector error**	**Detector error**
	[MeV]	**[MeV]**	**[%]**	**[keV]**	**[%]**	**[keV]**	**[%]**
T1	81,80 ± 0,99	0,99 ± 0,02	1,2	459 ± 187	47	528 ± 202	53
T5	83,81 ± 0,95	0,95 ± 0,02	1,1	752 ± 149	79	196 ± 171	21
T7	78,81 ± 1,36	1,36 ± 0,02	1,7	1088 ± 154	80	271 ± 176	20
T8	78,43 ± 1,31	1,31 ± 0,03	1,7	1042 ± 220	80	266 ± 253	20
T9	78,92 ± 1,40	1,40 ± 0,03	1,8	1090 ± 195	78	306 ± 224	22
T10	76,11 ± 1,07	1,07 ± 0,02	1,4	779 ± 140	73	286 ± 156	27

Table 4: Average values of energy, $FWHM$, energy resolution in percent, electronic and detector components with their associated errors, for each telescope, relating to the elastic scattering $^{16}O+^{197}Au$ at 85 MeV.

Elastic scattering: $^{12}C+^{197}Au$ at 75 MeV							
Telescope	**Energy mean**	**FWHM (total error)**	**Resolution**	**Electronic error**	**Electronic error**	**Detector error**	**Detector error**
	[MeV]	**[MeV]**	**[%]**	**[keV]**	**[%]**	**[keV]**	**[%]**
T1	72,78 ± 0,90	0,90 ± 0,01	1,2	459 ± 187	51	444 ± 199	49
T5	74,57 ± 0,87	0,87 ± 0,03	1,2	752 ± 149	86	118 ± 183	14
T7	70,16 ± 1,30	1,30 ± 0,02	1,9	1088 ± 154	84	212 ± 177	16
T8	69,89 ± 1,23	1,23 ± 0,03	1,8	1042 ± 220	85	185 ± 248	15
T9	70,35 ± 1,33	1,33 ± 0,02	1,9	1090 ± 195	82	239 ± 214	18
T10	67,88 ± 0,99	0,99 ± 0,02	1,5	779 ± 140	78	215 ± 155	22

Table 5: Average values of energy, $FWHM$, energy resolution in percent, electronic and detector components with their associated errors, for each telescope, relating to the elastic scattering $^{12}C+^{197}Au$ at 75 MeV.

Elastic scattering: $^{12}C+^{197}Au$ at 65 MeV							
Telescope	**Energy mean**	**FWHM (total error)**	**Resolution**	**Electronic error**	**Electronic error**	**Detector error**	**Detector error**
	[MeV]	**[MeV]**	**[%]**	**[keV]**	**[%]**	**[keV]**	**[%]**
T1	62,65 ± 0,90	0,90 ± 0,02	1,4	459 ± 187	51	437 ± 203	49
T5	64,22 ± 0,91	0,91 ± 0,02	1,4	752 ± 149	83	154 ± 171	17
T7	60,47 ± 1,31	1,31 ± 0,02	2,2	1088 ± 154	83	217 ± 178	17
T8	60,25 ± 1,25	1,25 ± 0,03	2,1	1042 ± 220	83	210 ± 252	17
T9	60,67 ± 1,33	1,33 ± 0,03	2,2	1090 ± 195	82	244 ± 223	18
T10	58,47 ± 1,02	1,02 ± 0,02	1,7	779 ± 140	76	242 ± 161	24

Table 6: Average values of energy, $FWHM$, energy resolution in percent, electronic and detector components with their associated errors, for each telescope, relating to the elastic scattering $^{12}C+^{197}Au$ at 65 MeV.

By comparing the results obtained, some qualitative conclusions can be drawn. Specifically, it can be noted that the mean energy values are homogenous and in agreement with the beam energy, for each elastic scattering respectively. This is most evident for telescopes T1 and T5; the other ones show a slightly lower energy value than expected. A likely explanation is that the detector has a dead region (or not fully depleted); further investigations could be useful for a fully understanding and correction.

The estimation of the energy resolution of the front side of DSSSDs gave a value around $0.5\%\ RMS$, which corresponding to $1.5\ MeV$ at $300\ MeV$ of peak: the resolution results better for the higher energies and decreasing for the lower ones. The total error associated to the energy measured was around $1.5\ MeV$. Finally, from the evaluation of the intrinsic and electronic components of the error, the analysis has confirmed that approximately 80% of the total deviation was due to the electronic chain, i.e. the digitizer, the preamplifier and anything else coming from the whole experimental setup.

Regarding the energy resolution of the back side of the DSSSDs, the difference between the energies released by the particle in the front and back sides, divided by the energy lost in the first one, that means the ratio $\frac{\Delta E_{front}-\Delta E_{back}}{\Delta E_{front}}$, was evaluated for each front strip in coincidence with all back strips of each DSSSD with thickness of 300 μm. The analytical procedure was analogous to the already described method for the front side. Therefore, from gaussian fits, the energy resolution of the back side of DSSSDs was estimated around

1.6% RMS, which corresponding to 4.8 MeV at 300 MeV of peak (see Fig. 40).

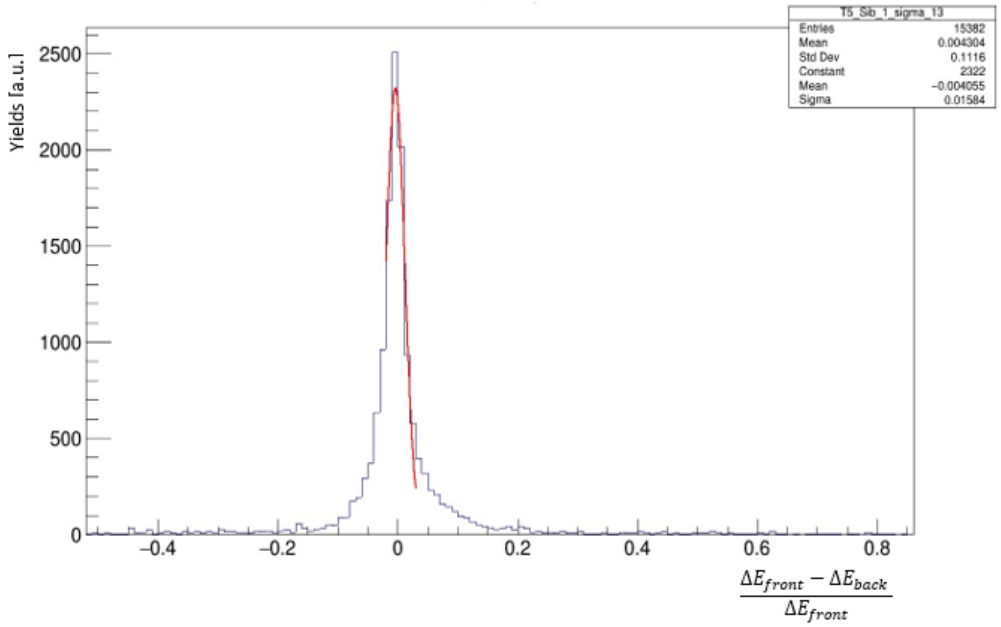

Figure 40: Histogram of the energy peak released on the strip n°13 of the first DSSSD of the telescope n°5. The ratio $\frac{\Delta E_{front} - \Delta E_{back}}{\Delta E_{front}}$ is evaluated for each front strip in coincidence with all back strips, for $^{16}O+^{197}Au$ @ 85 MeV elastic scattering. From the Gaussian fit, the sigma parameter is calculated.

3. *The "pixelation technique": a timing analysis for the unambiguous reconstruction of the particle position in the detector.*

The choice to use DSSSDs as the first two stages of the FARCOS array clusters allowed us to implement a specific technique for the reconstruction of the detected particles. In fact, in the most recent experimental setups for nuclear physics experiments, DSSSDs have become excellent instruments capable of collecting particles with very high energy and angular resolution, thanks to their segmentation into strips. They have reduced the need of several electronic channels: for a giving surface coverage, a single detection

system, having 32×32 strips, is now able to detect particles and their positions, instead of involving 1024 detectors. However, there are also some disadvantages, such as efficiency issues, and in particular the possibility that a fraction of the incident particles on the DSSSD may not be measured correctly. The so-called "interstrip events" identify those cases in which the particle is collected into the very slight region between two adjacent strips; this means that its energy is shared between them, altering the real reconstruction of the particle. Finally, considering the possibility that multiple particles are measured in the same detection system, the capability to assign the correct position to each particle may be affected by some difficulties. These motivations encourage the CHIMERA Collaboration to improve a method, the so-called "pixelation technique" [CAR24, CAR25] appropriate for the DSSSDs of the FARCOS correlator, testing it with the data collected at INFN-LNS. The ultimate goal of this method is to assign the correct position to each particle detected by FARCOS, in terms of its coordinates: from the analysis of the fired strip of the front side and the one of the back side of the first stage of a FARCOS telescope, *i.e.* the 300 μm thick DSSSD, the pair of the polar angle θ and the azimuthal one ϕ determine a unique spatial position of the particle.

The procedure works step by step [ZAG25c]. After the calibration phase already explained, for each telescope the ΔE-E matrices obtained (shown in Figs. 35-37) include all experimental events, without discrimination with regard to noise, electronic inductions, interstrip events, and so on. A selection of the events was mandatory.

In a first step, some experimental constraints were imposed on the particle multiplicity in a single FARCOS telescope, meeting the following conditions:

a. particles stopped inside the Si stages, that means multiplicity equal to zero in the CsI(Tl) crystals
b. multiplicity equal to 1 in both sides of the first DSSSD, and also in the front side of the second DSSSD; about the last back side a multiplicity less than 4 is required
c. ideally, the energy released by the incident particle at the front side of the detector should be approximately the same as that lost at the corresponding back side; concerning the FARCOS telescopes, the evaluation of the energy resolution highlighted some differences between the energy resolutions of two sides of the DSSSDs (back sides have a worse energy resolution). Experimentally, an energy range of ±15% was imposed between the energy measurements on the two corresponding sides. This specific range was chosen in order to maintain a good compromise in the statistics of the events
d. strips hit by a particle must be the same, comparing the first and the second DSSSDs front sides, or at most the previous or subsequent one, so neighbouring.

For the events with multiplicity equal to one, that means with a single particle detected in a single FARCOS telescope, a good assignment of the position of the particles detected without ambiguity was achieved.

In the next step of the procedure, condition b. was partially modified to extend the selection and also include events with multiplicity equal to 2 on the front sides of the two DSSSDs. The

other constraints relating to the energy and the fired strips remained unchanged. Unfortunately, with this new inclusion of additional events, some ambiguities have been observed. In particular, simply comparing the energies lost in the stages of the detector was no longer enough to classify all the events, meaning it was no longer possible to discriminate between interstrip, electronic induction or spurious events. Table 7 illustrates some examples of the several ambiguities examined. If two different energy values are measured only in the second DSSSD, and the fired strip are adjacent, then this has been classified as an interstrip event: the real energy released by the particle can be reconstructed from the sum of the two values. Conversely, in other cases where energies and strip appear uncorrelated, the ambiguities remain unresolved. The pixelation technique must be implemented using another variable in the analysis, such as the time variable [CAR24, CAR25].

<table>
<tr><th></th><th>ΔE_front [MeV]</th><th>ΔE_back [MeV]</th><th>E_front [MeV]</th><th>Nstrip_300_front</th><th>Nstrip_300_back</th><th>Nstrip_1500_front</th></tr>
<tr><td rowspan="4">#1</td><td rowspan="4">51,6344</td><td rowspan="4">51,8097</td><td>79,8859</td><td rowspan="2">29 [1]</td><td rowspan="2">13 [1]</td><td>29 [0]</td></tr>
<tr><td>148,723</td><td>30 [1]</td></tr>
<tr><td colspan="4">228,6089</td><td colspan="2">Position ambiguity resolved: this is an interstrip event in DSSSD_1500µm (ambiguity in energy only)</td></tr>
<tr><td rowspan="3">#2</td><td>12,9576</td><td>12,9558</td><td>22,1211</td><td>4 [0]</td><td>0 [0]</td><td>4 [0]</td></tr>
<tr><td>118,896</td><td>120,412</td><td>180,113</td><td>13 [1]</td><td>25 [1]</td><td>13 [1]</td></tr>
<tr><td colspan="6">Unresolved ambiguity: are these 2 different particles?? Could we assign their position using the TIME VARIABLE??</td></tr>
<tr><td rowspan="4">#3</td><td>12,0703</td><td>12,3186</td><td rowspan="3">24,9049</td><td>29 [0]</td><td>29 [1]</td><td rowspan="2">30 [1]</td></tr>
<tr><td>114,905</td><td>116,925</td><td>30 [1]</td><td>18 [0]</td></tr>
<tr><td>126,9753</td><td colspan="3">Unresolved ambiguity: this is an interstrip event in DSSSD_300µm; Could we assign its position using the TIME VARIABLE??</td></tr>
</table>

Table 7: examples of observed ambiguities, simply comparing the energies lost in the stages of the detector and the fired strips; the implementation of the time variable could be useful to improve the pixelation technique.

The timing analysis allows to exclude unphysical events, *i.e.* noise and spurious coincidences, examining the detection time of the particles. The so-called "detection time" variable is obtained from the digitized signal: it is defined as the time during which the signal reaches 10% of its amplitude, after the subtraction of the baseline.

For each telescope of the FARCOS correlator, time difference spectra were plotted, evaluating the difference between the detection times of a particle crossing the front and back sides of the first DSSSD (300 μm thick). The difference is centred around the zero, and the sigma appraised by a Gaussian fit is approximately $0.22\ ns$, for example for the telescope n°5, considering the "neutron-rich" ^{124}Sn+^{64}Ni system (Fig. 41). Analogue results are obtained for the other telescopes and reactions analyzed in the CHIFAR experiment. The long tails of the coincidence time peak are due to both differences in time of flight, which cannot reasonably occur for well measured events, and so they will be identified as "spurious events", and as noise affecting the timing of the small signals. The analysis also included the study of the two-dimensional distributions relating to the already calculated time difference as a function of the detected energy of the particle, again relating to the sides of the first DSSSD (see Fig. 42, relating the same T5 and "neutron-rich" reaction). Finally, the time difference between the detection time of a particle punching through both front sides of the second DSSSD - 1500 μm thick - and the first one - 300 μm thick - was plotted. For each telescope and studied reactions, from gaussian fits, a time difference around $(0.58 \pm 0.27)\ ns$ was measured: this means that the particle detection time is longer in the second stage than in the first one of the FARCOS telescope (Fig. 43).

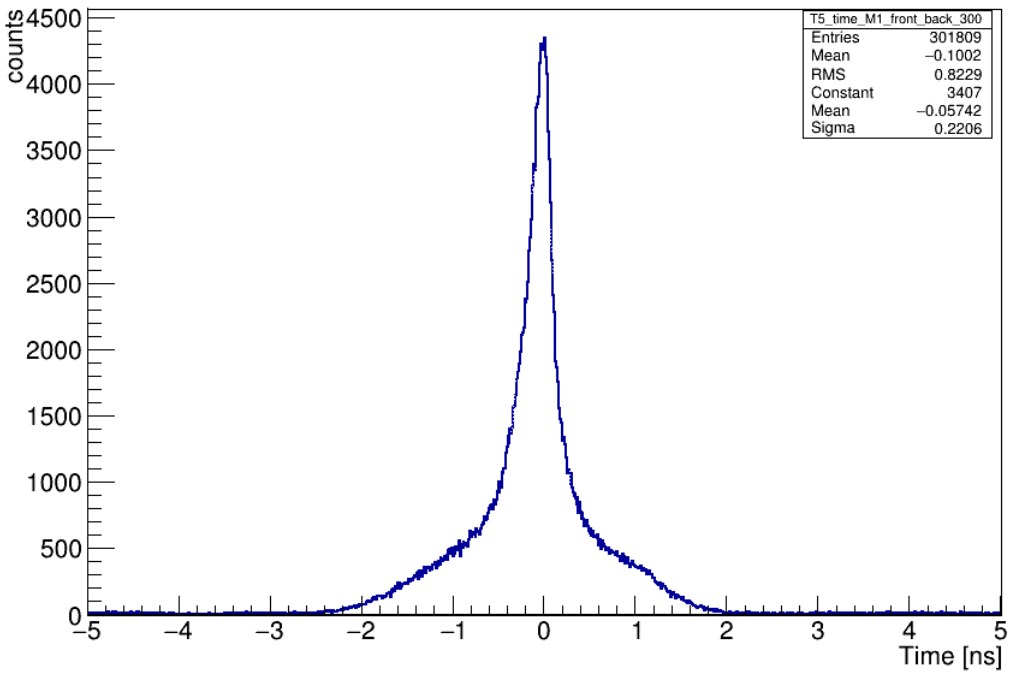

Figure 41: Time difference spectrum between the detection times of a particle crossing the front and back sides of the first DSSSD (300 µm thick), for the telescope n°5, from data collected in the $^{124}Sn+^{64}Ni$ "neutron-rich" reaction.

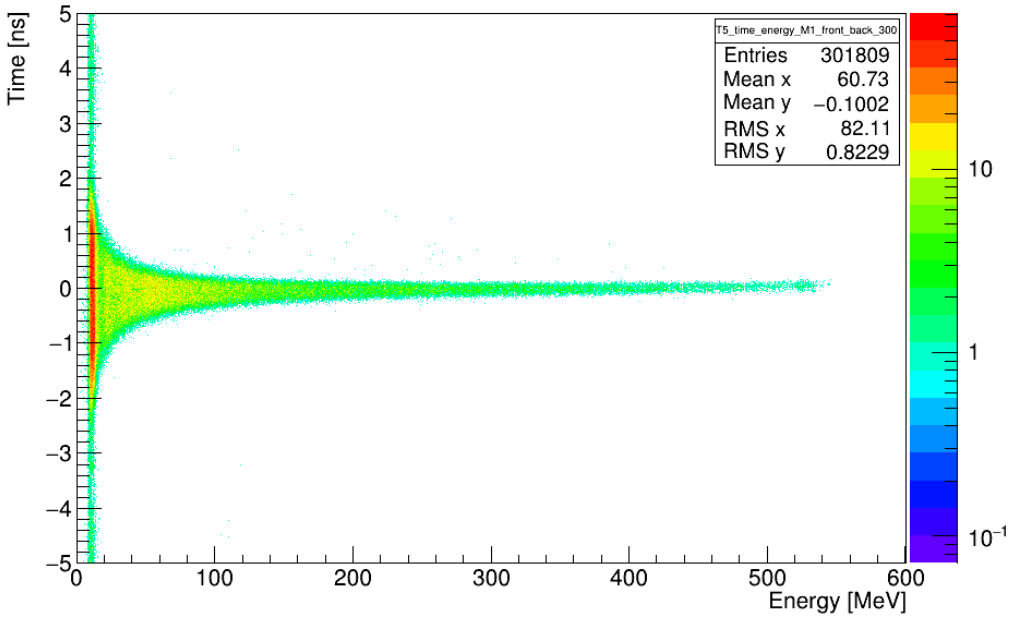

Figure 42: Time difference spectrum, as a function of the energy released by a particle crossing the front and back sides of the first DSSSD (300 µm thick), for the telescope n°5, from data collected in the $^{124}Sn+^{64}Ni$ "neutron-rich" reaction.

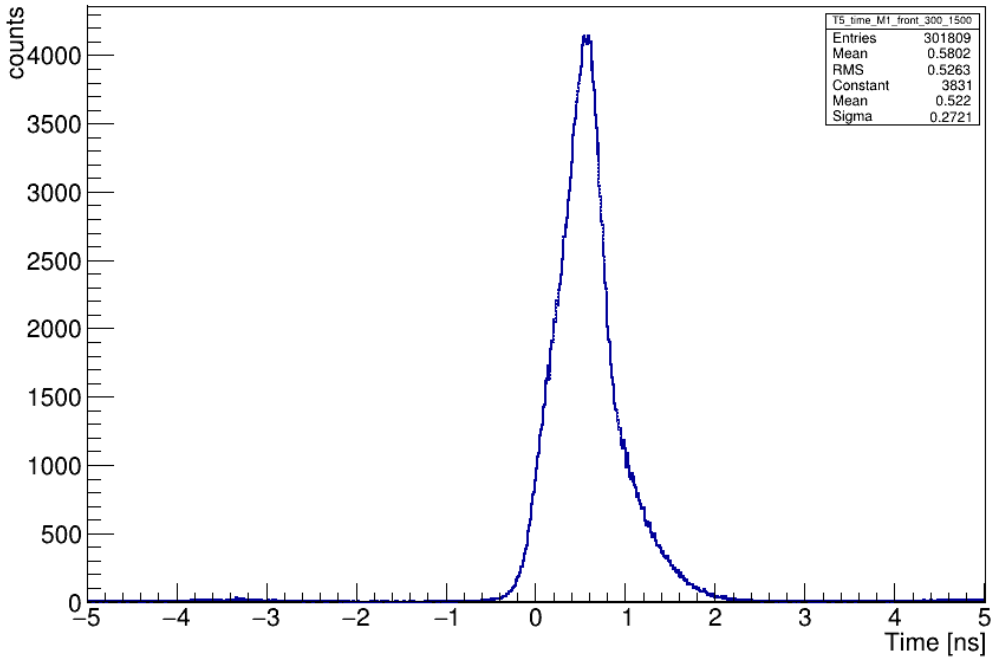

Figure 43: Time difference spectrum between the detection times of a particle crossing both front sides of the second DSSSD (1500 µm thick) and the first one (300 µm thick), for the telescope n°5, from data collected in the $^{124}Sn+^{64}Ni$ "neutron-rich" reaction.

The time differences, between the sides of the first DSSSD and between the two stages, calculated with the above descripted procedure, allow to select the events with multiplicity equal to 2 on the front sides of the two DSSSDs. Specifically, a particle is accepted and included in the final analysis, as belonging to the event only if its detection time falls within the time window $[mean - 2\sigma; mean + 2\sigma]$, in order to maintain a good statistic. In fact, according to this choice, the described time analysis assured the exclusion of spurious coincidence and noise in the selected events. Finally, the interstrip events in the second DSSSD were reconstructed and resolved as a unique event of an incident particle having a real energy given by the sum of the two values measured in the two close fired strips.

The final step of the applied "pixelation technique" concerned unambiguously assigning the correct position to each particle

detected by the FARCOS correlator. By considering their coordinate pairs, namely the polar angle θ and the azimuthal angle ϕ, the univocal spatial position of the particle can be plotted in a matrix of the $\phi\ vs.\ \theta$ plane, for all ten FARCOS telescopes employed in the CHIFAR experiment (see Fig. 44). The angular distributions, obtained for each reaction studied, allowed to verify the angular coverage of FARCOS in the experimental setup, that means a polar coverage between 13°-30° in the laboratory frame system, and a total azimuthal coverage of 2π, according to the coupling of the FARCOS telescopes around the CHIMERA sphere, as already shown in Figure 1.

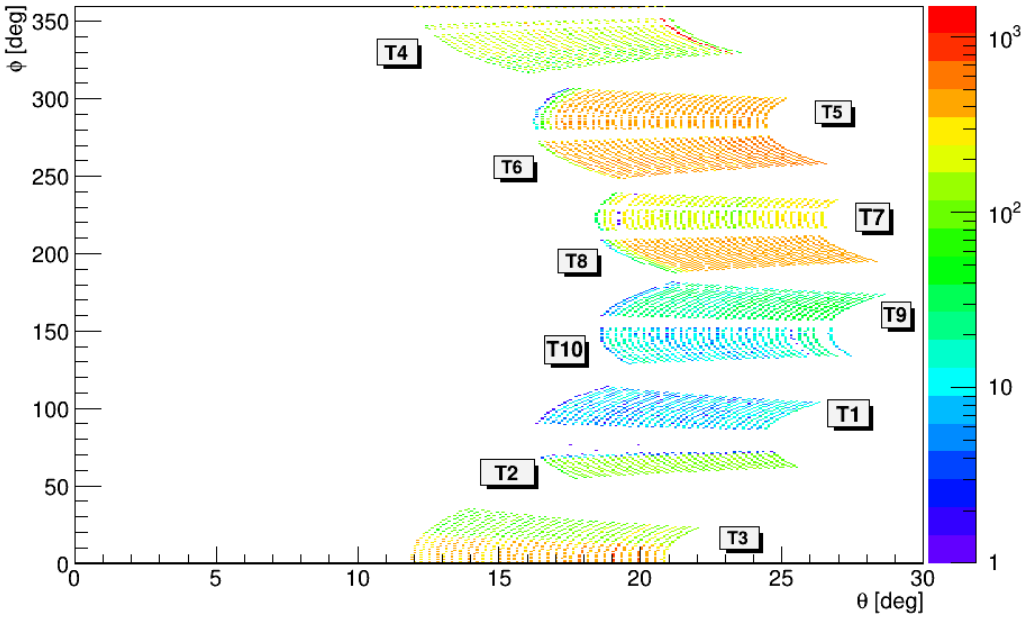

Figure 44: Angular distribution in the $\phi\ vs.\ \theta$ plane, for all FARCOS telescopes used in the CHIFAR experiment. The assignment of the position of detected particles is unambiguously; this distribution is related to the events collected by the $^{124}Sn+^{64}Ni$ "neutron-rich" reaction.

4. Identification of the IMFs detected by the FARCOS correlator.

The first objective of the CHIFAR experiment, as already discussed at the beginning of this chapter, was the investigation of the IMFs productions at the low beam energy of $20\,AMeV$. Data analysis moved on the identification of the final products of the six nuclear collisions studied in the CHIFAR experiment. Specifically, the identification phase of the IMFs detected by the FARCOS correlator involved the ΔE-E technique, applied between the first and the second DSSSD of each FARCOS telescope.

4.1 Particles identification techniques.

The experimental setup of the CHIFAR experiment, that means the FARCOS correlator and the 4π CHIMERA multi-detector are ideal tools for the measurement of the energies released by the detected particles. Additionally, their velocities can be estimated. Several techniques allow the identification of the reaction products, using these experimental measurements thanks to the performance of the detection systems [LEO87, KNO].

The incident charged particles interact with the material of the detectors and lose a part, or all, of their initial energy.

The quantum-mechanical calculation was first performed by Bethe, Bloch, and other physicists. The energy transfer was parametrized in terms of the transfer momentum, since it is a measurable quantity, while the impact parameter is not. The quantity of the energy loss is expressed by the Bethe-Bloch formula (5):

$$-\frac{dE}{dx} = 2\pi N_a r_e^2 m_e c^2 \rho \frac{Z}{A}\frac{z^2}{\beta^2}\left[\ln\left(\frac{2m_e\gamma^2 v^2 W_{max}}{I^2}\right) - 2\beta^2 - \delta - 2\frac{C}{Z}\right] \quad (5)$$

whit the following parameters involved:

- r_e: classical electron radius
- m_e: electron mass
- N_a: Avogadro's number
- I: mean excitation potential
- Z: atomic number of absorbing material
- A: atomic mass of absorbing material
- ρ: density of absorbing material
- z: charge of incident particle in unit of e
- $\beta = v/c$ of the incident particle
- $\gamma = 1/\sqrt{1-\beta^2}$
- δ: density effect correction
- C: shell correction
- W_{max}: maximum energy transfer in a single collision.

The formula (5) highlights that the energy loss of a particle crossing in an absorbing material is proportional to the square z^2 of the atomic number of the incident particle, and inversely proportional to the square of the velocity of the particles. It also depends on the ratio $\frac{Z}{A}$ between the atomic and mass number of the absorbing material.

The dependence on the nature of the particle allows us to identify in charge the detected particles. Besides, in some cases, the discrimination in mass is also possible, characterizing the production of isotopes. The so-called "ΔE-E technique" is one of the particle

identification methods used in the analysis of the reconstruction of nuclear collisions, based on the physics described.

The ΔE-E technique requires the use of a telescope as a detection system. In the first thinner detector, the incident charged particle loses a portion of its initial energy, called "lost energy" ΔE; subsequently, it is stopped inside the second stage of the telescope, where its "residual energy" E can be measured. This happens if the energy of the particle is such that the particle passes through the first detection stage and is then stopped in the second stage. The sum of the lost and the residual energies is equal to the initial incident energy of the particle. The two measured quantities can be plotted in a two-dimensional distribution: the ΔE-E matrix shows several hyperbolic branches, and for this reason also called "banana-plot". Each line identifies charged particles according to their atomic number Z and atomic mass number A. In particular, according to the square dependence from the charge in the Bethe-Bloch formula, the banana lines are larger separated increasing the atomic number Z with respect to the mass number A, which instead allow to discriminate the different isotopes, grouped in the sets of less separated hyperbolas. In particular, using the array structure of CHIMERA and FARCOS, a good identification of the light fragments ($Z \lesssim 20$) can be observed (see Figs. 45, 46).

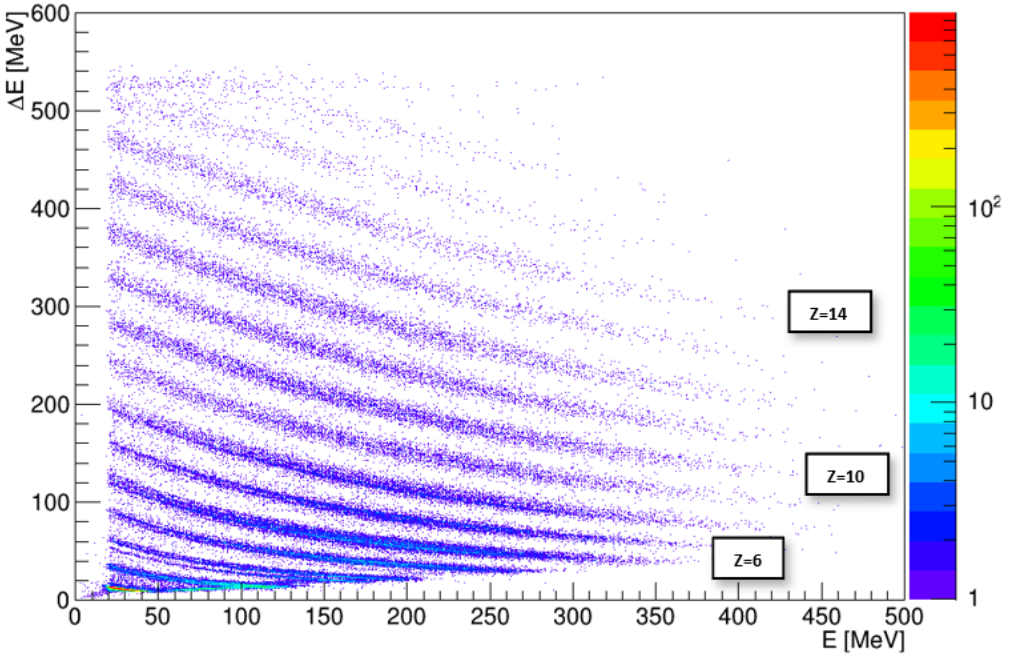

Figure 45: An example of a typical ΔE-E matrix, obtained from the analysis of "neutron-poor" ^{112}Sn+^{58}Ni reaction at incident beam energy of 20 $AMeV$, from data collected from the FARCOS correlator in the CHIFAR experiment. Hyperbolic curves are clearly distinguishable between $2 \leq Z < 16$.

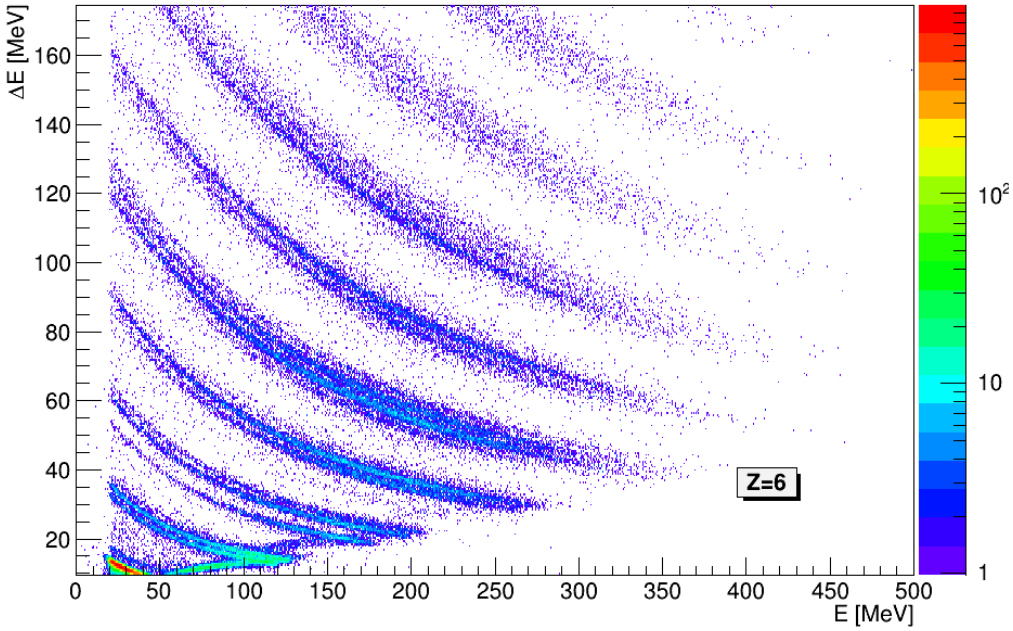

Figure 46: Zoom of the previous ΔE-E matrix, relating to ^{112}Sn+^{58}Ni reaction: the good separation between the isotopic lines, based on the mass number A, can be appreciated.

Another method applied for the particle identification is the "Pulse Shape Discrimination" (PSD) technique. In scintillator detectors, in particular in the inorganic ones, the yield trend, corresponding to the collected emission scintillation light, can be composited of the sum of two exponential decays: they are called "fast" and "slow" components, produced by the de-excitation of the atoms, after the crossing of the particle in the detector. The fast and slow components have different decay times, independent of each other. Typically, in the inorganic scintillators, compared with the fast decay time, the time constant τ_1 ranges from $0.4\ \mu s$ to $0.7\ \mu s$ (fast), while τ_2 has a consistent value of about $3.2\ \mu s$ (slow). The fraction of light appearing in the slow component often depends on the nature of the exciting particle. This dependence can be useful to discriminate between different kinds of particles that released the same energy in the detector: it is the principle of the particle identification used in the PSD method.

In the CHIMERA and FARCOS detectors, the light produced by the CsI(Tl) crystal scintillators is then collected by the coupled photodiodes and finally converted into an electrical signal. From this signal, the fast and slow components are extrapolated. The relative yields of the two components depend on the specific energy loss of the particle and, hence, can be used to identify the light charged particles and their isotopes up to $Z{\sim}3$ (left panel of Fig. 47).

As already described in Chapter 2, an in-depth study of the shape of signals produced in the detectors has been conducted [PAG04, PAG12, PAG12b]. In particular, particles with $Z > 2$ which stopped in the Silicon detector (300 μm thick), thanks to the performances of CHIMERA, can be identified in charge by using the

PSD method applied on Silicon detectors. After some upgrades of the front-end electronics for the CHIMERA Si detectors, the rise-time of the signals (between the 30% and 80% of the signal maximum) was measured and then studied versus the energy ("E-rise-time" technique), in order to obtain mass and charge identifications for the reaction products stopped inside the Si stages [POL05-ALD04b]. The PSD-Si method has made CHIMERA a unique 4π multi-detector in the world, thus able to measure the heavy fragments originating from the target in order to characterize the entire reaction event (right panel of Fig. 47).

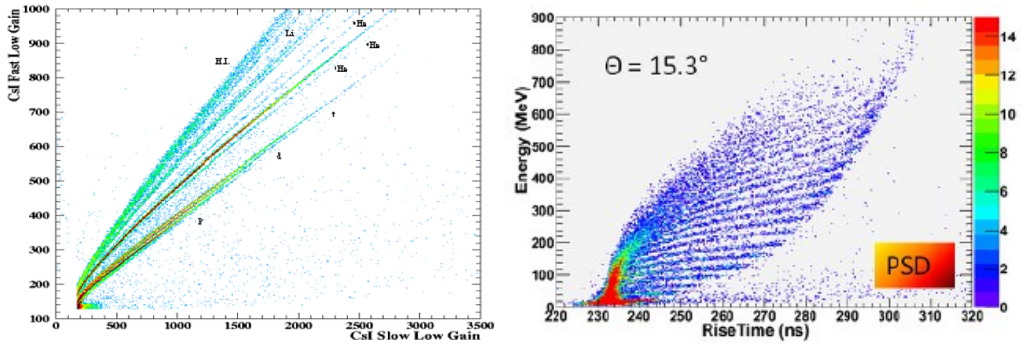

Figure 47: Pulse Shape Discrimination identification for the $^{124}Sn+^{64}Ni$ nuclear reaction at 35 $AMeV$, related to the CsI(Tl) crystals of the CHIMERA multi-detector: (left panel) a fast-slow matrix; (right panel) kinetic energy as a function of the rise time (Si-PSD)[PAG12b].

The energy measured by the detector is physically correlated to the velocities of the incident particles. The "Time-Of-Flight" (TOF) technique is applied to calculate the velocity of the particles. This method uses the "start" and "stop" reference times, that are sent to the TDC. The digital output is proportional to the time interval that includes the real time of flight of the particles, needed to arrive in the detector plus a delay due to electronic chain. According to the conversion factor, the TOF can be expressed as the difference (6):

$$TOF = \alpha * (t_{ch} - t_0) \quad (6)$$

where t_0 is the electronic delay between the start and the stop signal. The velocity is then determined by the classical ratio between the distance travelled by the particle and the TOF.

If the particle is stopped inside the detector stage, it has released all its kinematic energy. Its mass can be evaluated by the inverse formula (8):

$$M = 2Ev^2 = 2E\frac{TOF^2}{d^2} = 2E\frac{\alpha*(t_{ch}-t_0)^2}{d^2} \quad (8)$$

where E is the total energy measured.

The CHIMERA beam line was equipped with an efficient Micro-Channel Plate (MCP) timing system and a microstrip Silicon tagging detector [LOM11, PAG12b]. The tagging system was based on the E-TOF technique, in order to identify the incident ions coming from exotic beams produced by the projectile fragmentation of primary beams, delivered by the CS housed at INFN-LNS. The MCP was placed upstream on the beamline, while a DSSSD was located approximately 2 meters upstream the target. By correlating the energy released in the DSSSD as a function of the TOF calculated between the two detectors, the resulting distribution is shown in Figure 48 [RIS25]. It is possible to identify several isotopes, from ^{6}He up to ^{17}C ions.

This characterization is an important aspect of the scientific program of the CHIMERA Collaboration, with a view to improve the study of the large isospin asymmetric nuclear matter. The final goal is to determine the evolution of the reaction mechanism for both binary collisions, compound nucleus reactions and multi-fragmentation [PAG12b, AMO09, PIR11].

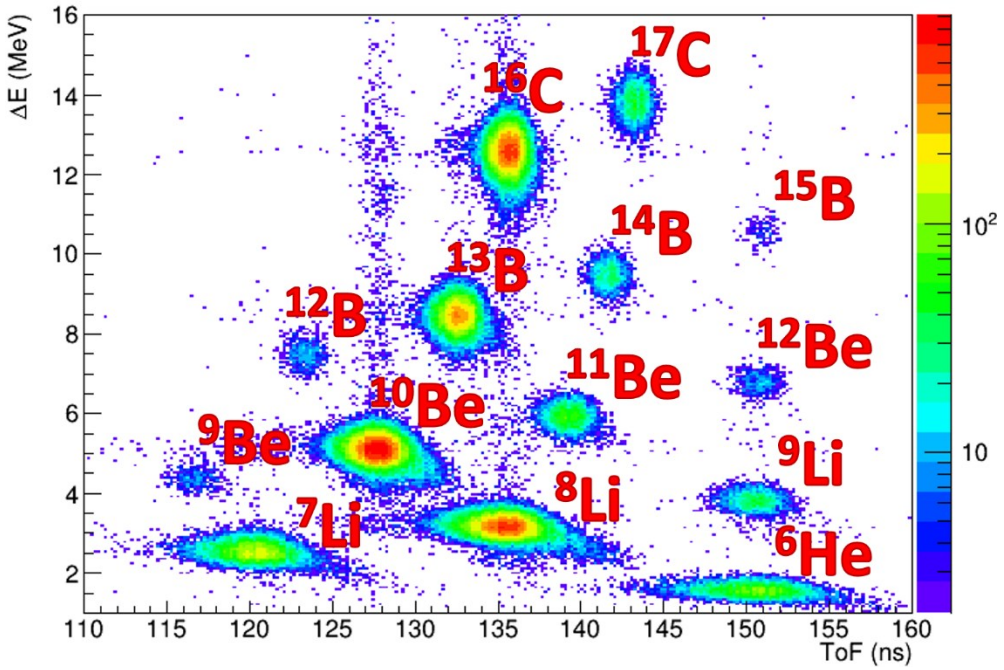

Figure 48: ΔE-TOF calibrated plot; correlating the energy released as a function of the TOF, several isotopes can be identified, from ^{6}He up to ^{17}C ions [RIS25].

4.2 The ΔE-E technique applied to IMFs detected by FARCOS.

The FARCOS array configuration is ideally suited for the application of the ΔE-E technique, in order to identify the IMFs produced after the six nuclear collisions studied in the CHIFAR experiment [ZAG25, ZAG25b, ZAG24].

The first two DSSSDs of each FARCOS telescope were considered as the interaction layers of the IMFs. This means that the measurement of the energy loss ΔE of the particles in transmission on the first stage of the telescope, *i.e.* the 300 μm thick DSSSD, was studied as a function of the residual energy E of the particles stopped in the second stage, *i.e.* the 1500 μm thick DSSSD. Based on the Bethe-Bloch formula (5) already explained, the CHIMERA Collaboration has implemented an identification algorithm: by evaluating the two contributions ΔE and E, for a given particle, it

was used the following proportionality (9), which then generates the equilateral hyperbolic curves in the final plots:

$$\Delta E * E \propto z^2 * m \tag{9}$$

The identification phase of the IMFs detected by the FARCOS correlator maintained the same experimental constraints used in the analysis with the "pixelation technique". For each telescope, the ΔE-E matrix studied was obtained from the already discussed conditions about energy, fired strips and multiplicity of the particles impinging on the single telescope according to the timing analysis. This selection of the events ensured that there was no ambiguity in the application of the algorithm for identifying IMFs. Figures 49-54 illustrate the ΔE-E matrices acquired from the data collected by the $^{124}Sn+^{64}Ni$ "neutron-rich" reactions, for six of the FARCOS telescopes analyzed. Similar plots are observed for the other five reactions of the CHIFAR experiment.

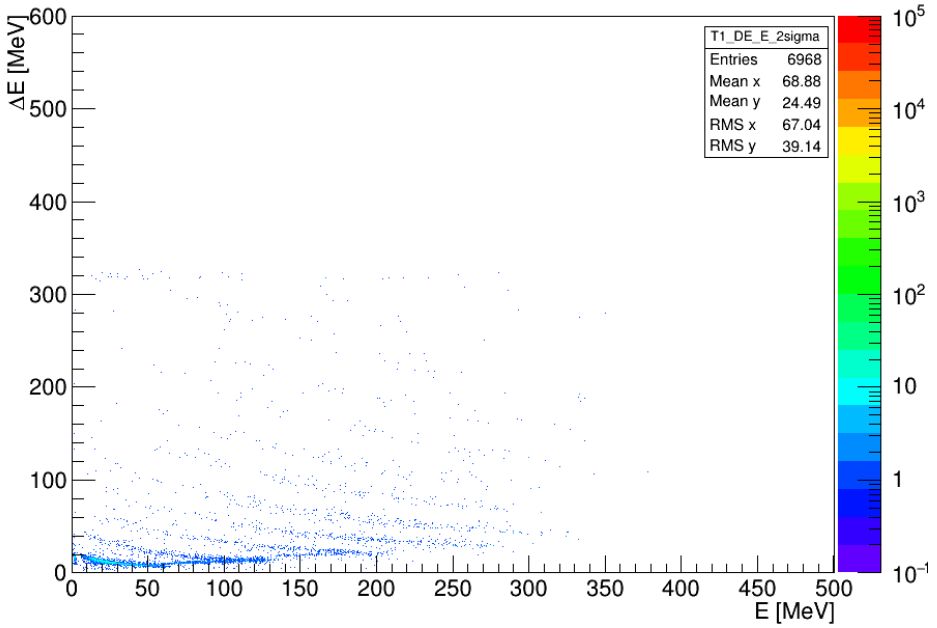

Figure 49: ΔE-E matrix for the telescope n°1, relating to the data collected from the $^{124}Sn+^{64}Ni$ "neutron-rich" reaction. Experimental constraints were imposed to select events with particle multiplicity up to 2 and to eliminate noise and spurious coincidences.

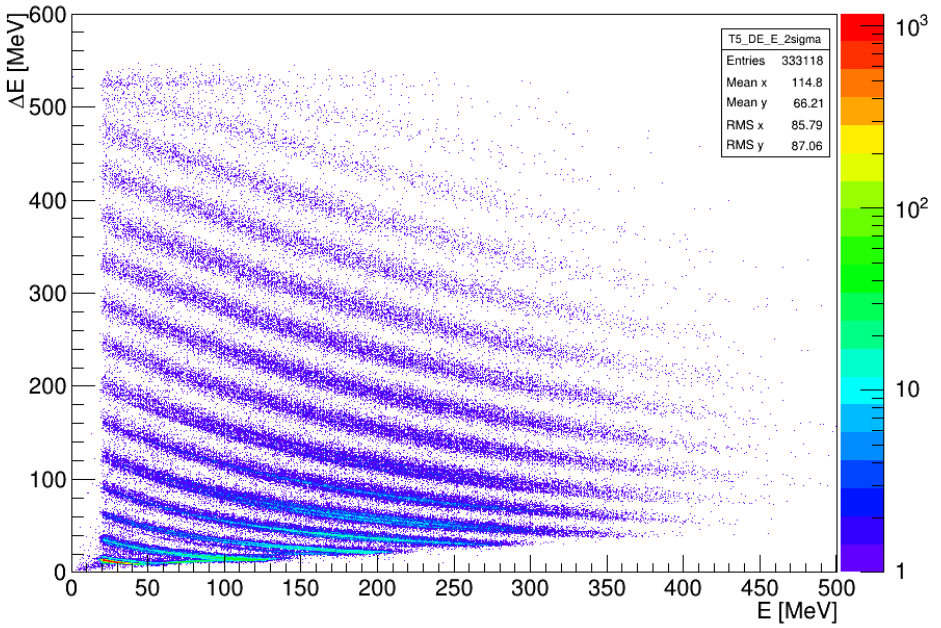

Figure 50: ΔE-E matrix for the telescope n°5, relating to the data collected from the $^{124}Sn+^{64}Ni$ "neutron-rich" reaction. Experimental constraints were imposed to select events with particle multiplicity up to 2 and to eliminate noise and spurious coincidences.

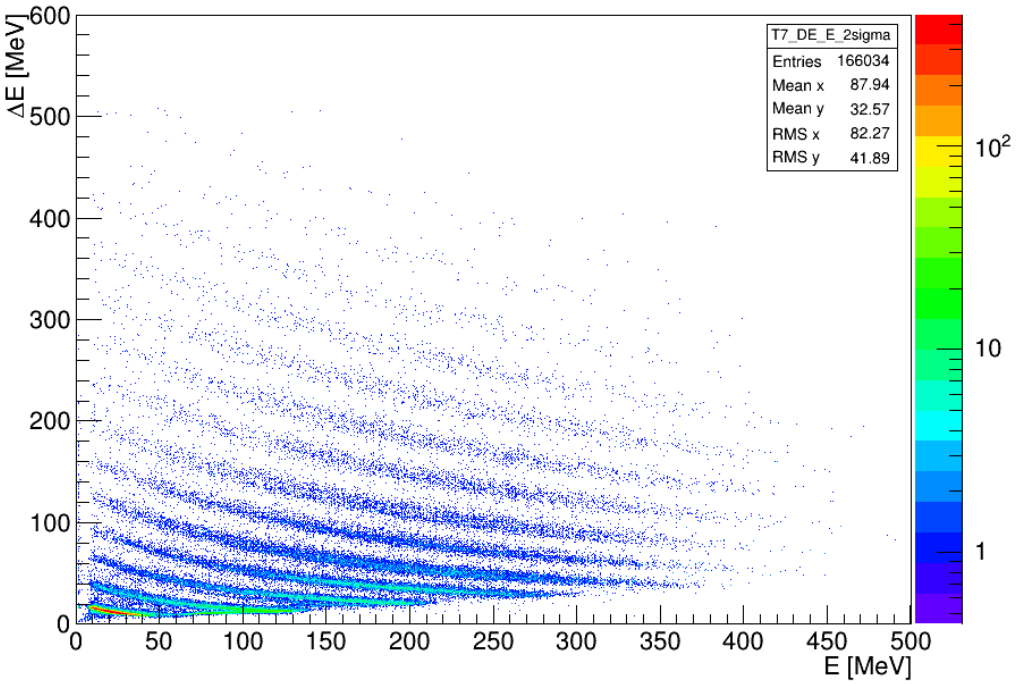

Figure 51: ΔE-E matrix for the telescope n°7, relating to the data collected from the $^{124}Sn+^{64}Ni$ "neutron-rich" reaction. Experimental constraints were imposed to select events with particle multiplicity up to 2 and to eliminate noise and spurious coincidences.

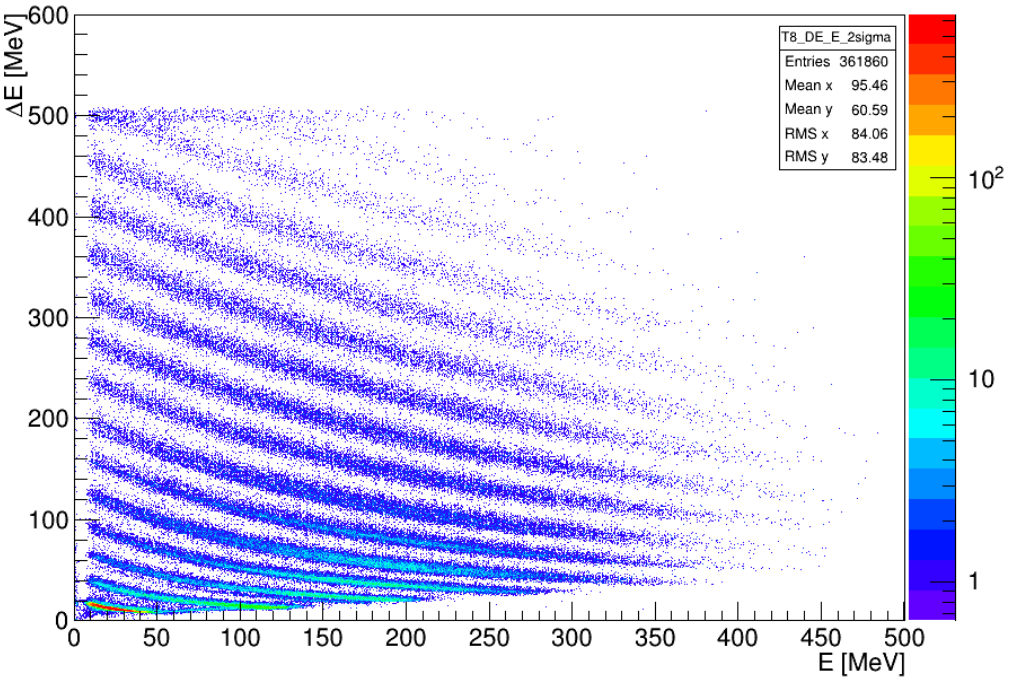

Figure 52: ΔE-E matrix for the telescope n°8, relating to the data collected from the $^{124}Sn+^{64}Ni$ "neutron-rich" reaction. Experimental constraints were imposed to select events with particle multiplicity up to 2 and to eliminate noise and spurious coincidences.

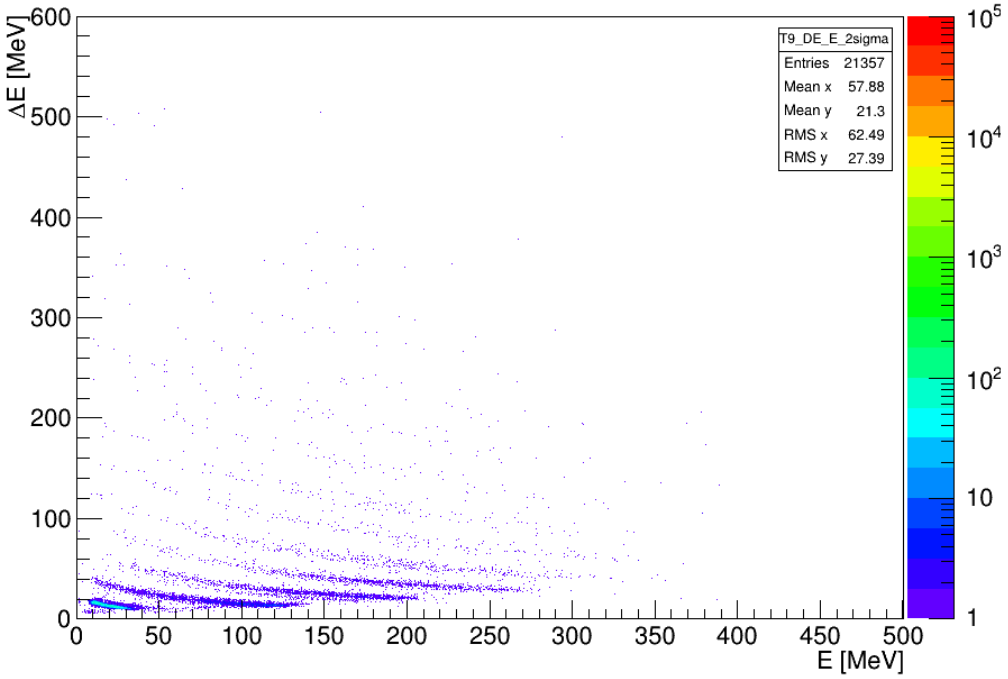

Figure 53: ΔE-E matrix for the telescope n°9, relating to the data collected from the $^{124}Sn+^{64}Ni$ "neutron-rich" reaction. Experimental constraints were imposed to select events with particle multiplicity up to 2 and to eliminate noise and spurious coincidences.

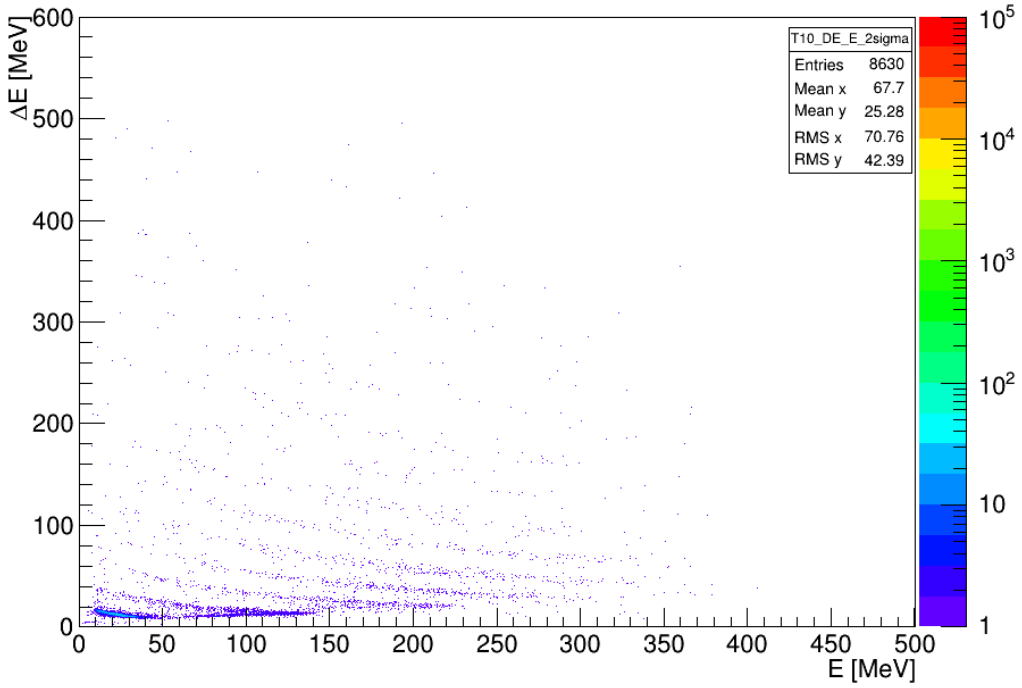

Figure 54: ΔE-E matrix for the telescope n°10, relating to the data collected from the $^{124}Sn+^{64}Ni$ "neutron-rich" reaction. Experimental constraints were imposed to select events with particle multiplicity up to 2 and to eliminate noise and spurious coincidences.

The final step of the identification process used the implemented algorithm to fit "banana" plots, for each telescope. Geometrically, FARCOS covered the angular region between 13° and 30° in the laboratory frame system. By considering this configuration, data analysis provided a good identification of the detected particles. In details, IMFs were identified in charge up to $Z \approx 16$; furthermore, isotopes could be discriminated with the mass number up to $A \approx 20$, which corresponds to the atomic charge $Z \approx 9$. In the two-dimensional spectra, protons are not represented, because they release very low energy in the first detection stage. In future analysis, they will be identified using other methods, such as the PSD applied to the CsI(Tl) crystals. An example of the fitting results from the application of the identification algorithm is shown

in the figure below (blue, red and pink lines indicate the fits in Fig. 55). The analysis highlighted some differences for telescopes n° 1, 9 and 10. The statistics of the events were much lower, as these latter telescopes did not perform optimally. The IMFs identification could be extracted up to $Z \approx 7$ (see Fig. 56). Probably, the experimental constraints applied were too restrictive, and other procedures are needed to find better results.

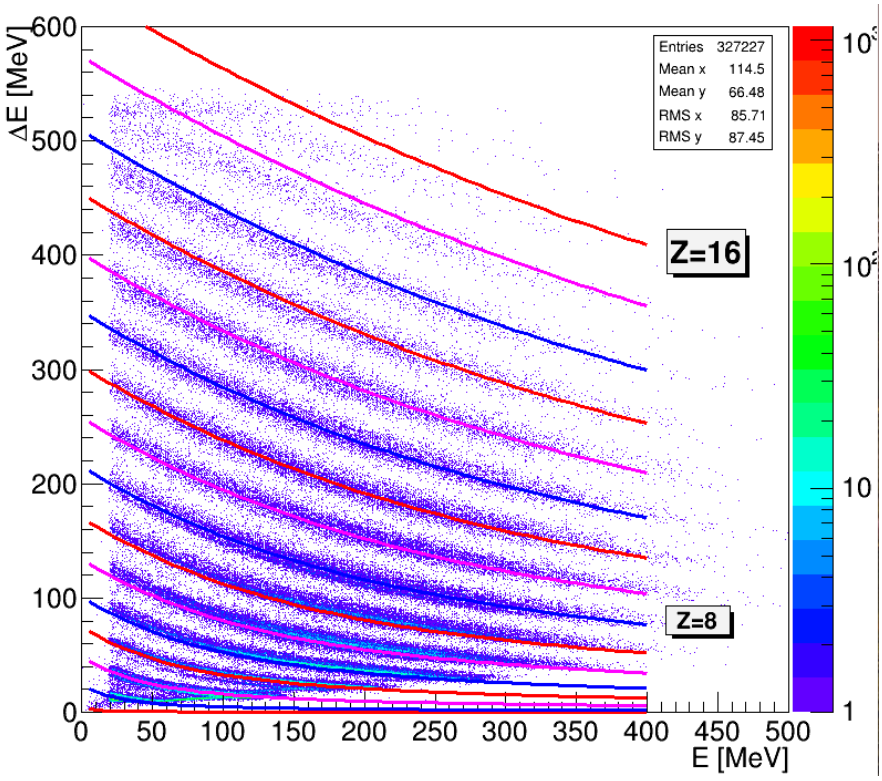

Figure 55: Identification fit algorithm applied to the banana lines of the ΔE-E matrix of the telescope n°5, relating to the data of the $^{124}Sn+^{64}Ni$ "neutron-rich" reaction. IMFs were well identified in charge up to $Z \approx 16$.

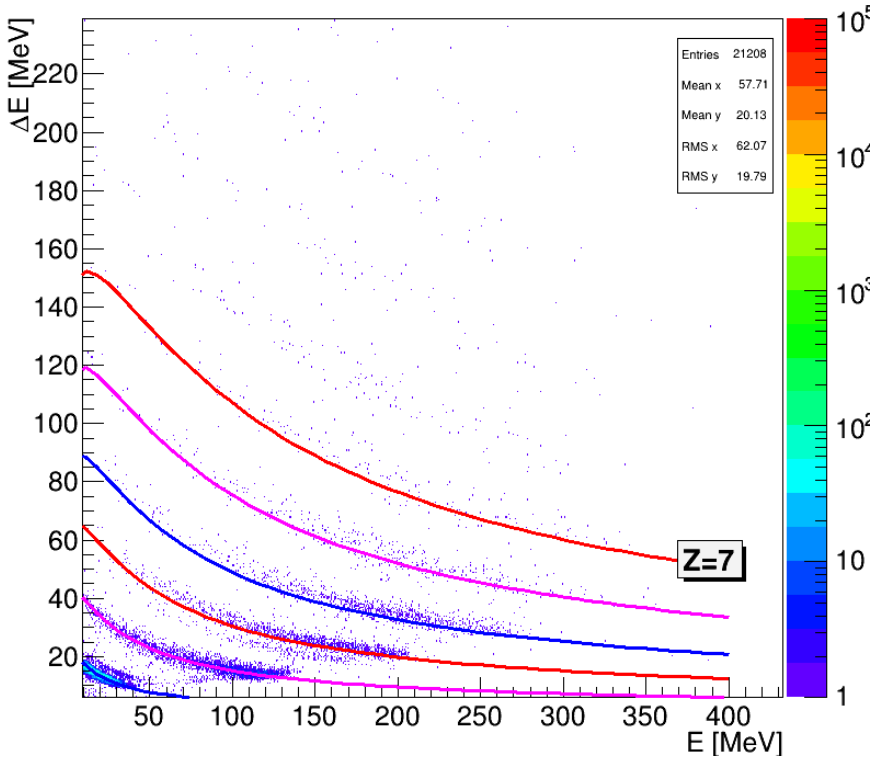

Figure 56: Identification fit algorithm applied to the banana lines of the ΔE-E matrix of the telescope n°9, relating to the data of the ^{124}Sn+^{64}Ni "neutron-rich" reaction. IMFs were well identified in charge up to $Z \approx 7$.

The fit identification algorithm also allows to extrapolate the charge and mass distributions for each telescope. The experimental procedure highlighted the goodness of the discrimination obtained from the fits. Specifically, distributions are plotted as function of the atomic charge Z (two examples are shown in Figs. 57, 58) and the atomic mass number A (two patterns in Figs. 59, 60) for the isotopes stopped on the second DSSSD of the analyzed telescope. In fact, for each atomic number Z, only the isotopes with a lifetime enough to reach the detector ($> 50\ ns$) and to pass through the first stage and stopped in the second stage of the FARCOS telescope have been identified, as can be noted from the mass distributions.

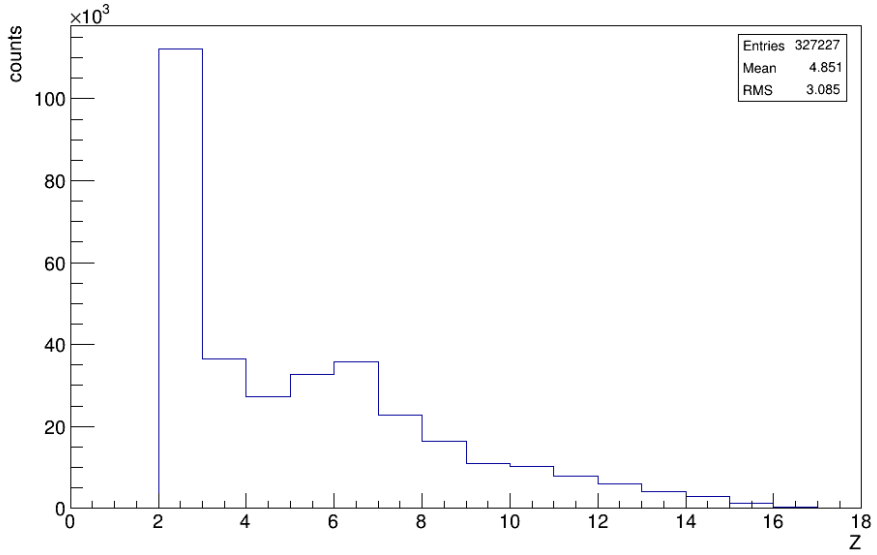

Figure 57: Charge distribution for the particles stopped on the second DSSSD of the telescope n°5, relating the $^{124}Sn+^{64}Ni$ "neutron-rich" reaction.

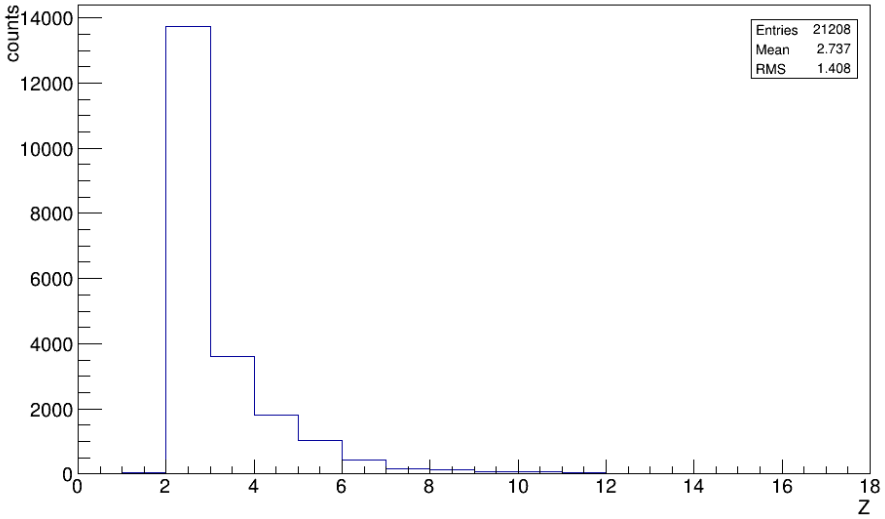

Figure 58: Charge distribution for the particles stopped on the second DSSSD of the telescope n°9, relating the $^{124}Sn+^{64}Ni$ "neutron-rich" reaction.

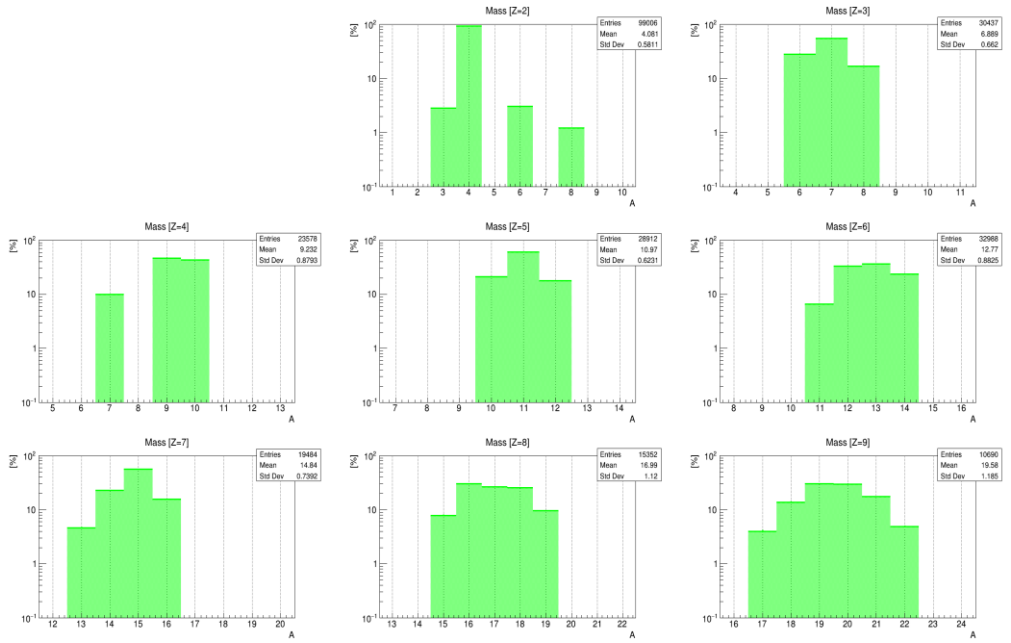

Figure 59: Mass spectra for $2 \leq Z \leq 9$, identifying the particles stopped on the second DSSSD of the telescope n°5, in the $^{124}Sn+^{64}Ni$ "neutron-rich" reaction.

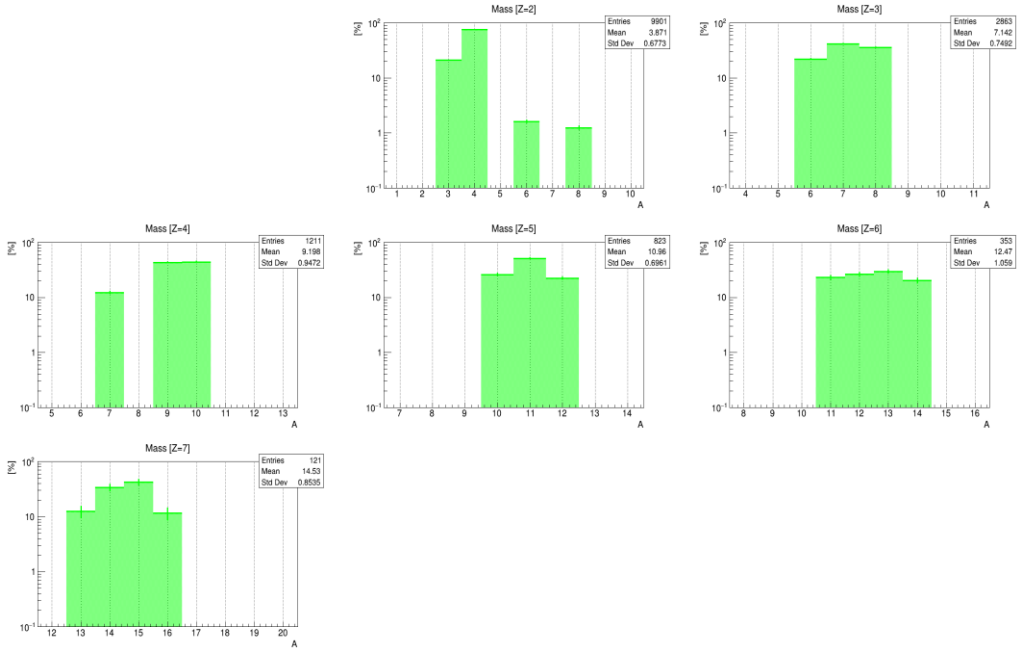

Figure 60: Mass spectra for $2 \leq Z \leq 9$, identifying the particles stopped on the second DSSSD of the telescope n°9, in the $^{124}Sn+^{64}Ni$ "neutron-rich" reaction.

As already mentioned, protons and their isotopes cannot be distinguished using only the first two stages of the FARCOS telescopes; for this reason, they are absent in Figures 59 and 60. The particles identification in charge and in mass is different for each

telescope, due to the fact that not all telescopes worked at their best performance. Figures 61-64 illustrate some final checks in the identification procedure, obtained from the same algorithm. They are related to the identification for specific charge and/or mass.

Not all telescopes were operating at their maximum of energy resolution capabilities. It should be noted that in the CHIFAR experiment, the final version of the FARCOS correlator was coupled for the first time to the CHIMERA multi-detector, and several adjustments will be introduced later. In general, it can be stated that, under the experimental conditions and with the constraints discussed, a good particle identification has been reconstructed with the ΔE-E technique.

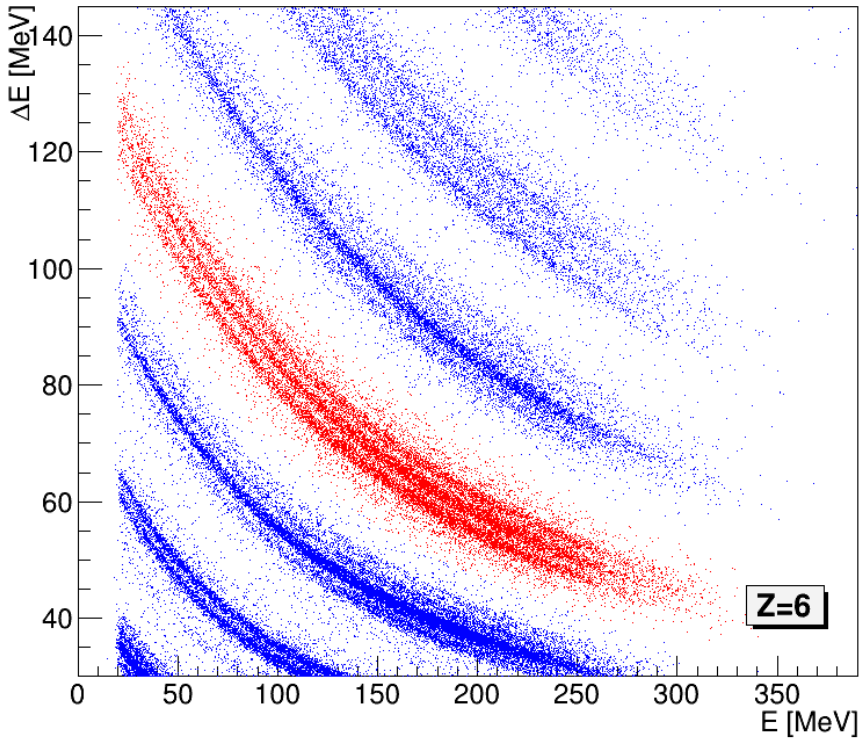

Figure 61: Zoom on identification in charge for the IMFs with atomic number $Z = 6$, related to the telescope n°5, for the $^{124}Sn+^{64}Ni$ "neutron-rich" reaction.

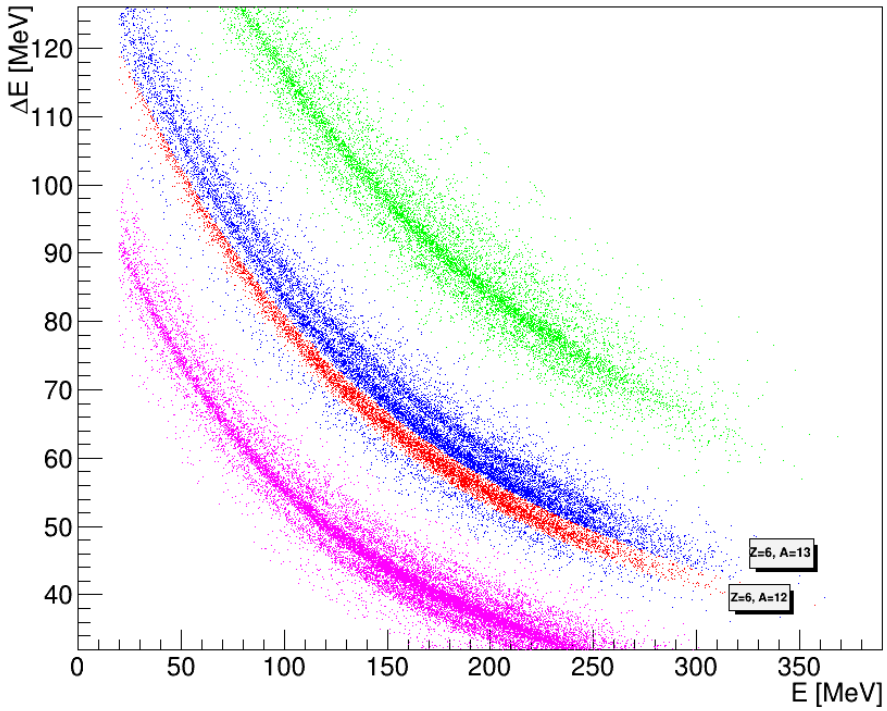

Figure 62: Zoom on identification in charge and mass for the IMFs with atomic number $Z = 6$ and mass number $A = 12$, related to the telescope n°5, for the ^{124}Sn+^{64}Ni "neutron-rich" reaction.

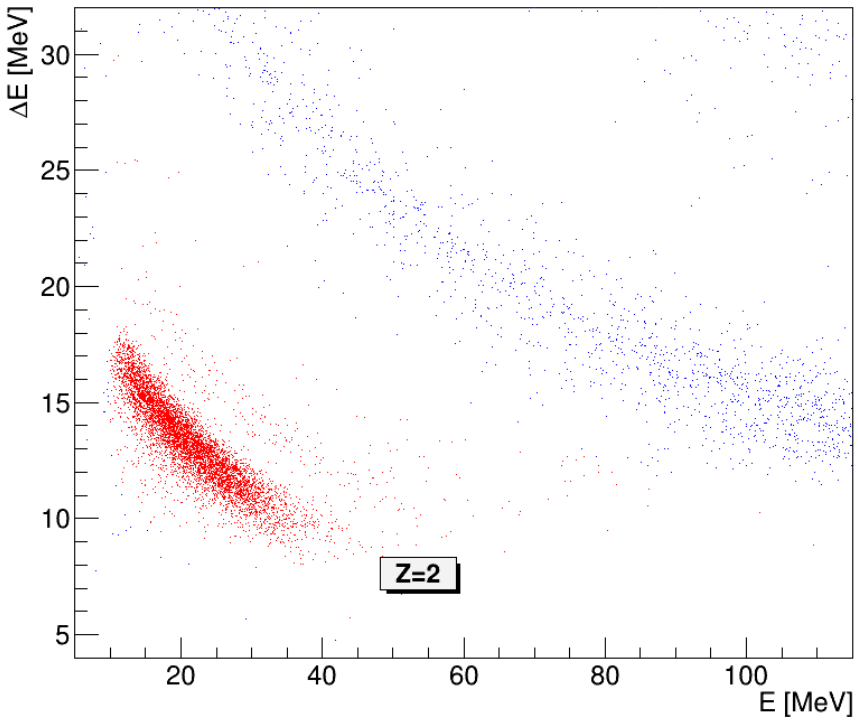

Figure 63: Zoom on identification in charge for the IMFs with atomic number $Z = 2$, related to the telescope n°9, for the ^{124}Sn+^{64}Ni "neutron-rich" reaction.

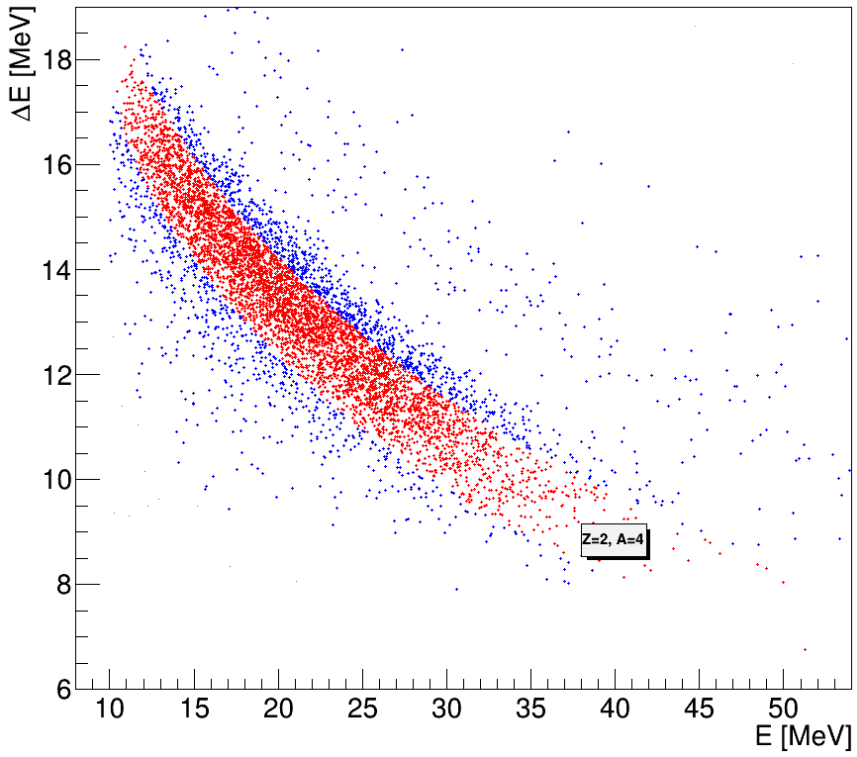

Figure 64: Zoom on identification in charge and mass for the IMFs with atomic number $Z = 2$ and mass number $A = 4$, related to the telescope n°9, for the $^{124}Sn+^{64}Ni$ "neutron-rich" reaction.

CHAPTER 4

Studies on isospin content and dynamical emission.

1. The Isospin role in Heavy Ion Collision @ 20 AMeV: a preliminary analysis.

The data analysis of the CHIFAR experiment also aims to investigate the role of the isospin degree of freedom in HICs at low energy regime, in order to highlights the cruciality of the isospin content of the colliding system in understanding of the HI collisions.

In a first phase of this study, some preliminary evidence has already been obtained considering the data collected only by the FARCOS correlator [ZAG25, ZAG25b]. Nevertheless, the comparisons of the preliminary charge and mass distributions of the particles detected by FARCOS, as obtained by using the particle identification algorithm, revealed interesting trends. In particular, the analysis focused on the three main nuclear reactions studied in the CHIFAR experiment at the beam energy of 20 $AMeV$, namely the "neutron-rich" ^{124}Sn+^{64}Ni, the "neutron-poor" ^{112}Sn+^{58}Ni and the "isobaric" ^{124}Xe+^{64}Zn system. The choice aims to emphasize the differences between the respective isospin contents, *i.e.* the ratios $I = N/Z$ as already reported in Table 1 of chapter 1 of this thesis, and their consequent effects on the isotopic composition of the emitted IMFs.

The first comparison among the three systems concerned the charge distributions of the particles collected by FARCOS. Their normalized distributions of the atomic number Z are shown in Figure 65. To illustrate just one example of the results obtained, the

comparison relates to the particles identified by the FARCOS telescope n°5. In the picture, the blue dots represent the "isobaric" ^{124}Xe+^{64}Zn colliding system, the pink ones refer to the "neutron-poor" ^{112}Sn+^{58}Ni, and the green ones to the "neutron-rich" ^{124}Sn+^{64}Ni system. The contribute of each detected charge Z is evaluated as a percentage, with respect to the total, between $1 \leq Z \leq 17$. Of course, the protons and their isotopes are underestimated because most of them loose few energies in the silicon stages. From this preliminary analysis, there are not huge differences in the trends of the three main systems. In more details, an enhancement of light IMFs emission, that means for $3 \leq Z \leq 9$, can be highlighted in the "neutron-rich" collision. This may be correlated to an enhanced dynamical production of IMFs, according to the growth of the neutron contribute. A similar enrichment was found in the analysis of the dynamical emission probability with the data collected in the experiments at beam energy of 35 $AMeV$: nevertheless, in that case the relevant increase was found for IMFs of $Z \geq 7$ [RUS20], as can be seen in Figure 16 of Chapter 1. In addition, the "isobaric" system records a stronger emission of heavier IMFs, *i.e.* for $Z > 10$: the greater fissility of the projectile, which is proportional to Z^2, leads to a higher fission probability. But this result was different and not observed previously; one possible interpretation is that at low beam energy of 20 $AMeV$, the projectile fissility plays a more important role, while at 35 $AMeV$ the leading feature was the dynamical effects. However, these are only preliminary conclusions that need to be confirmed by more accurate and detailed analysis. Overall, the trends appeared similar and not significantly different from those

highlighted by REVERSE and InKiIsSy experiments [RUS20]. The above-mentioned divergences have to be carefully investigated to better understand the evolution of the reaction mechanisms as a function of the beam energy.

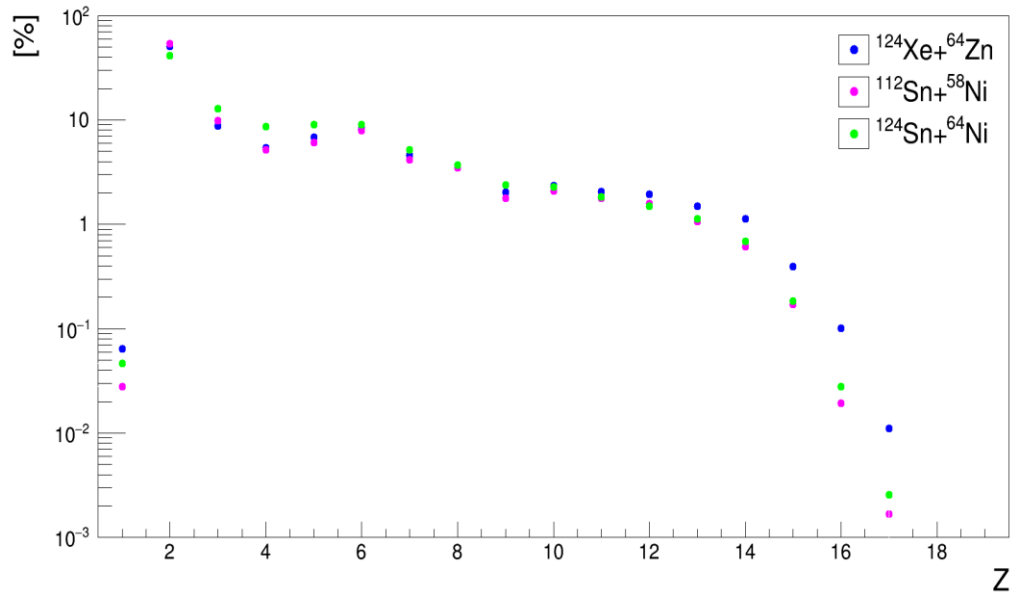

Figure 65: Comparison of the normalized distributions of the three reactions systems, as a function of the charge number Z; blue dots refer to the "isobaric" system ^{124}Xe+^{64}Zn, pink ones refer to the neutron poor system ^{112}Sn+^{58}Ni, and green ones to the neutron rich system ^{124}Sn+^{64}Ni, for FARCOS telescope n° 5.

After the charge distributions comparison, isotopes were studied for some selected atomic number Z. As already discussed in the chapter 3, the ΔE-E identification algorithm allowed to distinguish IMFs in charge up to $Z \approx 16$, and in mass up to $A \approx 20$ (corresponding to a charge of $Z = 9$). Specifically, the distributions of the isotopes detected by the FARCOS correlator having atomic number between $3 \leq Z \leq 6$ were studied, again referring to the three main reactions of the CHIFAR experiment. Subsequently, the histograms of the normalized yields expressed as percentages, as a function of the atomic mass numbers A, were compared, for each telescope. The isotopes used for these comparisons among the three different reactions are as follows:

- Lithium isotopes: ^{6}Li, ^{7}Li, ^{8}Li
- Beryllium isotopes: ^{7}Be, ^{9}Be, ^{10}Be
- Boron isotopes: ^{10}B, ^{11}B, ^{12}B
- Carbon isotopes: ^{11}C, ^{12}C, ^{13}C, ^{14}C.

The analytical procedure followed intermediate steps, in which the mass distributions for each telescope were superimposed and compared considering the pairwise reactions between them. In a first step, attention was paid to the ^{112}Sn+^{58}Ni and the ^{124}Sn+^{64}Ni systems. Mass distributions relative to the neutron rich configuration resulted systematically more abundant for higher atomic mass numbers, with the respect to the neutron poor one. Then, the study included the "isobaric" collision, first between the ^{124}Xe+^{64}Zn and the ^{124}Sn+^{64}Ni, which have the same total mass. Here too, a neutron enrichment effect was observed. The final pairwise comparison involved the ^{124}Xe+^{64}Zn and ^{112}Sn+^{58}Ni, reactions with approximately the same initial isospin content. And also in this case, the mass distributions showed the expected trends. However, a small tendency for the "neutron-poor" system to produce isotopes with fewer neutrons can be observed, due to the isospin impact of the two reactions. Finally, the mass distributions of the three reactions have been superimposed, for each atomic number Z, in order to better observe the overall nature of the results discussed. An example of these last plots obtained is illustrated in Figure 66, relating to the IMFs detected in the fifth telescope of the FARCOS correlator.

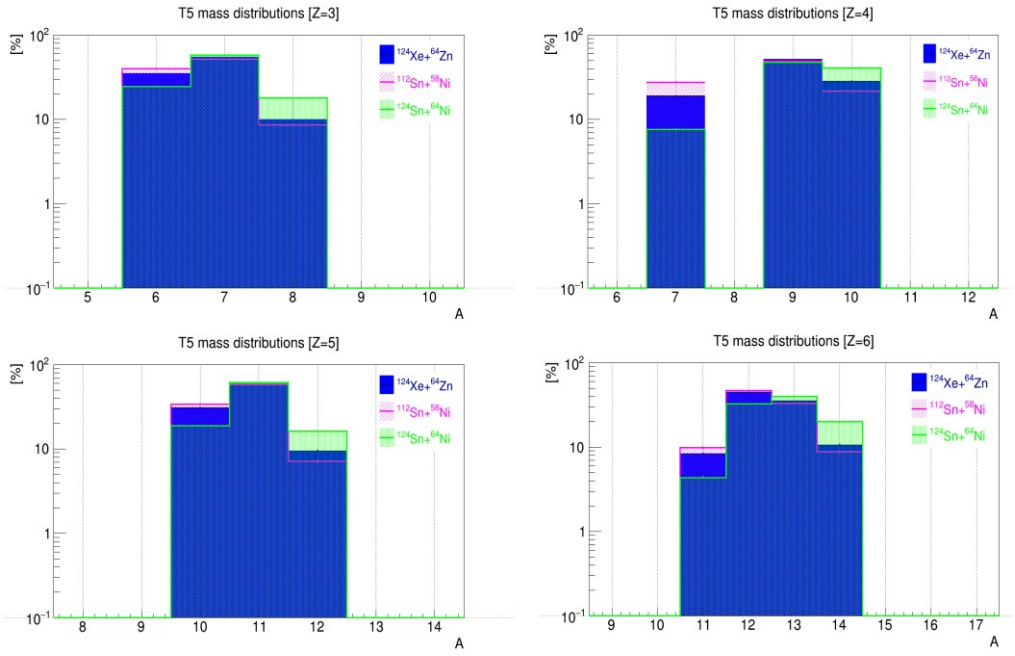

Figure 66: Comparison of the normalized percentage distributions as a function of the mass number A, for charge numbers Z from 3 to 6, for telescope n° 5; blue histograms are relative to the "isobaric" ^{124}Xe+^{64}Zn system, pink ones are associated to the "neutron-poor" ^{112}Sn+^{58}Ni one, and green ones refer to the "neutron-rich" ^{124}Sn+^{64}Ni one.

The highlighted effect of neutrons enrichment at higher atomic mass numbers, for any given Z, can be clearly correlated with the isospin ratio N/Z of the individual system. This preliminary analysis already allows us to emphasize the role of the isospin degree of freedom as entrance channel on the reaction outcomes. The final IMFs product distributions are keeping the memory of the initial isospin content, through the combination of the projectile and target. The pre-equilibrium, dynamical, and subsequent evaporation phases do not ultimately result in fragments distributed according to a natural abundance: the memory of the initial conditions, such as the isospin contribute, is not lost.

The analysis explained so far must be considered preliminary and not yet complete, for several reasons. First, the distributions included only data collected by the FARCOS correlator telescopes

used in the CHIFAR experiment. At this stage of the analysis, the CHIMERA data had not still been merged. This means that data had not yet been filtered with more advanced physical constraints. In particular, a selection based on global variables, such as the total multiplicity of charged particles, the reaction plane, the centrality of the nuclear reaction, equilibrated or dynamical fission processes, and so on, is mandatory for the characterization of the reaction mechanisms of the HICs studied at low beam energy of $20\ AMeV$. However, the effect of neutron enrichment had already been observed in the experimental results of the same reactions but studied at higher bombarding energy of $35\ AMeV$ [RUS20]. Now, in the present study, even at a lower incident energy, the isospin content appears to play an appreciable role in the neutron enrichment of the produced isotopes. The next step of the analysis, by filtering the data with more specific constraints based on the features of the entire experimental setup, will allow for more accurate results.

In future analyses, these results could be also implemented as constraints for transport models, such as SMF [BAR05] or CoMD-II [PAP07], and afterburner codes, such as GEMINI [CHA05]. This allows for simulation of reactions at the studied beam energy of $20\ AMeV$, in order to optimize model elements and provide a better reproduction of the experimental data.

2. *Some preliminary investigations of the dynamical effects with CHIMERA and FARCOS.*

The investigation of the IMFs emission mechanisms was the third objective proposed by the CHIFAR experiment, in terms of the difference between the statistical or dynamical emission processes, expressed by their probabilities. The status of the data analysis is not yet advanced enough to provide a definitive overview of the conclusions. However, some distributions relating to some physics cases will be illustrated below, in order to highlight some preliminary but interesting results [ZAG25, ZAG25b].

The data had not still filtered by the detector response, so the experimental conditions remained the same as those imposed at each phase of the data analysis explained so far in this thesis. Given the constraints required on the multiplicity and the energy of the IMFs collected by the FARCOS correlator, the study focused on already well identified particles, that means the IMFs with atomic charge $2 < Z < 16$ were selected. Please note that LCPs are not yet included, because they will be identified using the PSD of CsI(Tl) signals in future analyses. The distributions of the component of the velocity perpendicular to that of the beam axis (*i.e.* the perpendicular velocity), as a function of the parallel velocity was studied for each reaction of the CHIFAR experiment. Figure 67 shows the velocity distribution related to the "neutron-rich" ^{124}Sn+^{64}Ni system, as an example of the results. The emission of the IMFs is centred on the PLF velocity region in the laboratory frame system, between the center-of-mass velocity ($v_{c.m.}$~$4.08\ cm/ns$) and the beam velocity (v_{beam}~$6.18\ cm/ns$), towards the mid-velocity. The trend of the

velocity distributions highlighted the forward and backward emissions, with respect to the PLF velocity: these are some preliminary observations that could be related to IMFs dynamical emission, and all the reactions examined showed the same impacts.

Mass number distributions as a function of the parallel velocity were also studied: similar effect, as the ones already described are observed (see Fig. 68). Again, the lightest and fastest fragments were not involved in the present phase of the data analysis. Furthermore, considering the equivalent two-dimensional spectra related to the final reaction products collected by the CHIMERA multi-detector (see Fig. 69), the high resolution of the FARCOS correlator can be appreciated, in the good identification of the phase space for $2 < Z < 16$, and between the center-of-mass velocity and the beam velocity.

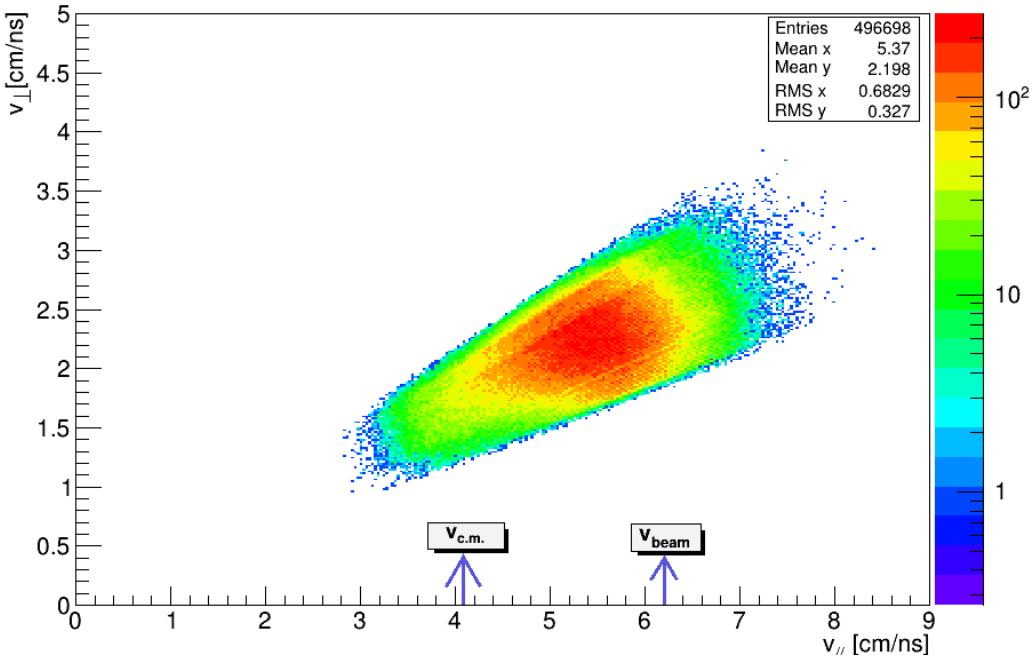

Figure 67: Distribution of the perpendicular velocity as a function of the parallel velocity, related to the "neutron-rich" $^{124}Sn+^{64}Ni$ system; IMFs with atomic charge $2 < Z < 16$ were selected. Values of beam and projectile-target center of mass velocities are indicated by the arrows in the plot.

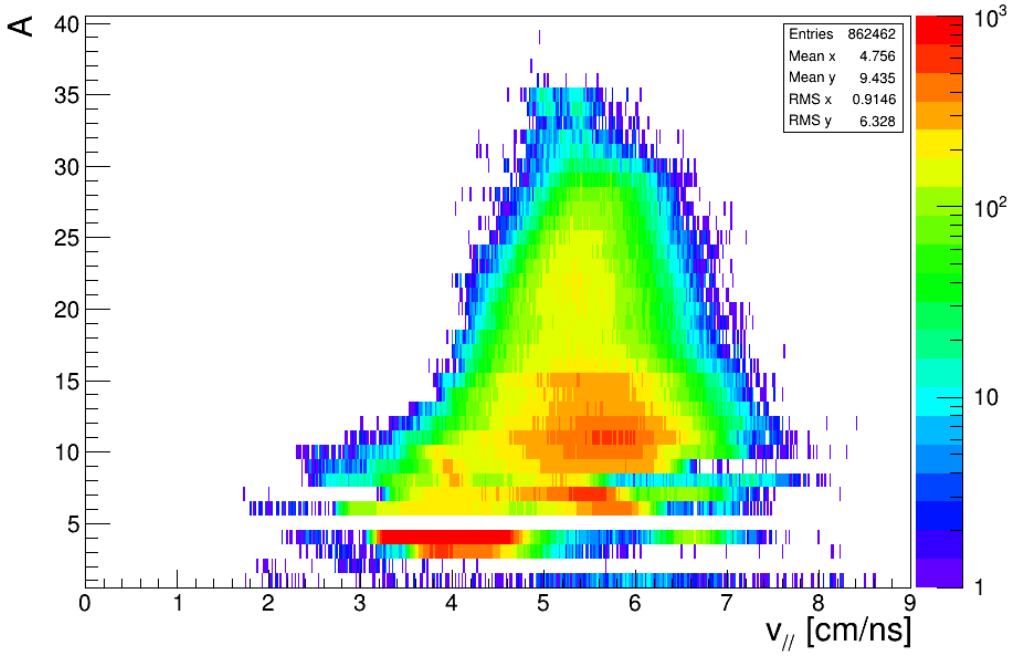

Figure 68: Mass number distribution as a function of the parallel velocity, related to the "neutron-rich" ^{124}Sn+^{64}Ni system; IMFs with atomic charge $2 < Z < 16$ were selected.

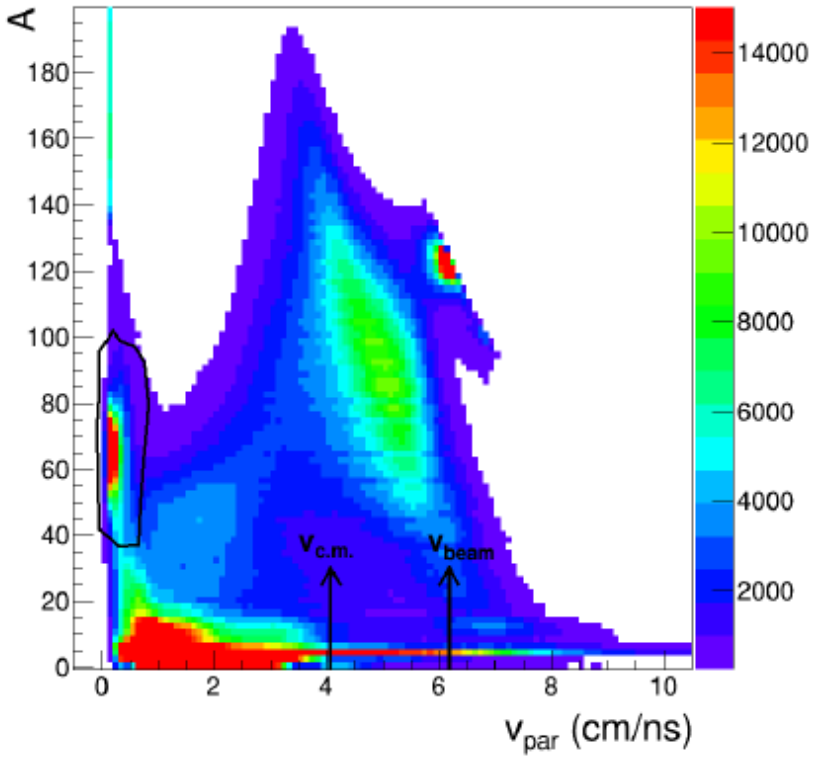

Figure 69: Mass number distribution as a function of the parallel velocity for the ions identified by using the CHIMERA multi-detector for the "neutron-rich" ^{124}Sn+^{64}Ni system.

In the research prospectives of the CHIMERA Collaboration, the primary focus of the CHIFAR experiment was fixed on the role of the isospin degree of freedom in HICs at low energy regime, linking it to the symmetry energy and the asy-stiff/soft parametrization of the asymmetric nuclear matter. The isospin dependence in HICs is still a matter of in-depth study: the isospin content plays a crucial role in understanding the nuclear interactions (in vacuum and in the medium), due to its connection with the Equation Of State (EOS) of the nuclear matter.

Isospin transport phenomena are strictly related to the formation of a dilute region within the dynamical neck-like structure [DEF14]. This density gradient is predicted to cause an excess of neutrons, indicated as the isospin migration, towards this dilute area. The extent of this migration depends on the slope of the symmetry energy, which is larger for the so-called "asy-stiff" parametrization at sub-saturation density compared to the so-called "asy-soft" one. Conversely, if the projectile and target have a large initial isospin N/Z asymmetry, the isospin diffusion through the neck drives the isospin equilibration. This diffusion is influenced by the magnitude of the symmetry energy at sub-saturation density, which is greater for the "asy-soft" parametrization. This means that both phenomena of isospin migration and isospin diffusion can compete to characterize the midrapidity and the residual isospin content of the projectile/target [LOM10]. The previous experiments of the CHIMERA Collaboration studied the degree of neutron enrichment for the dynamical emission of the IMFs in the region of the mid-rapidity, for the "neutron-rich" ^{124}Sn+^{64}Ni and the "neutron-poor" ^{112}Sn+^{58}Ni reactions, at beam energy of $35\ AMeV$. The fragments

were selected based on angular, velocity and isospin correlations, and the dynamical emission results were compared with those of the statistical emission from a PLF source [DEF12]. The distributions of the mean value of the isospin content $\langle N/Z \rangle$ as a function of the atomic number Z of the IMFs for the "neutron-rich" system at $35\ AMeV$ have been investigated: the results of the dynamical (DE) and statistical (SE) emissions of the IMFs have been compared (see Fig. 70) [DEF14]. The mean isospin contributes $\langle N/Z \rangle$ for the dynamically emitted fragments (indicated by black circles in Fig. 70) were systematically higher than those for the statistically emitted particles (red squares). The same effect was observed for the "neutron-poor" system, also studied at $35\ AMeV$. A comparison of the two emission types (DE/SE) for the two reactions is shown in Fig. 71. The experimental data had been also compared to SMF+GEMINI transport model calculations (see right panel in Fig. 70), in order to constraint the density dependence of the symmetry energy in the EOS of the nuclear matter. In particular, the SMF model implements the nuclear mean-field dynamics as well as the effect of fluctuations induced by nucleon-nucleon collisions. Regarding the parametrization of the potential contribution of the symmetry energy in the EOS, two different dependencies have been studied: the first, called "asy-stiff", increases linearly with the density of the nuclear matter; instead, the second, called "asy-soft", exhibits a weak variation around the nuclear saturation density $\rho_0 \approx 0.17\ nuc/fm^3$. In Fig. 70 the SMF+GEMINI calculations have been plotted as hatched histograms for dynamically emitted IMFs: specifically, the blue and magenta hatched areas are related to the asy-stiff and asy-soft parametrizations, respectively. As can be observed, the asy-stiff

parametrization, corresponding to a linear behaviour of the potential term of the symmetry energy with the nuclear matter density, produces more neutron-rich fragments than the asy-soft choice, ant it was better matched to the experimental data. The experimental isospin $\langle N/Z \rangle$ distributions of IMFs, as a function of their atomic number Z, have been plotted for both statistical and dynamical emissions, comparing the results of the "neutron-rich" $^{124}Sn+^{64}Ni$ (upper panel of Fig. 71) and the "neutron-poor" $^{112}Sn+^{58}Ni$ (lower panel of Fig. 71) reactions, at beam energy of $35\ AMeV$. A flattening of the odd-even effect on the $\langle N/Z \rangle$ distribution of the neutron-rich system with respect to the neutron-poor one can be clearly observed. In particular, the amplitude of this odd-even effect is enhanced for fragments dynamically emitted by the neck, with respect to the ones statistically emitted in the sequential decay: this highlights its crucial role in the reaction mechanism.

The correlation between the emission time scale of IMFs at midrapidity in semi-peripheral collisions and their isotopic composition gives strong indication that large values of isospin content are acquired by light IMFs dynamically emitted in the early stage of the reaction.

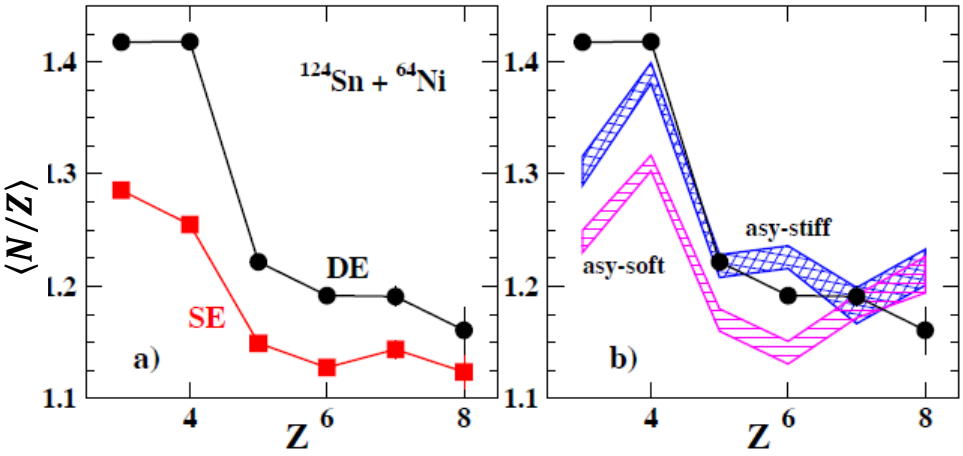

Figure 70: Isospin distributions as a function of the IMFs atomic number Z, for dynamical emission (DE) and statistical emission (SE), for the "neutron-rich" $^{124}Sn+^{64}Ni$ system at beam energy of 35 $AMeV$ (left panel); data of the dynamical emission are compared with SMF+GEMINI calculations (right panel) and asy-stiff parametrization (blue hatched area) or asy-soft parametrization (magenta hatched area) [DEF14].

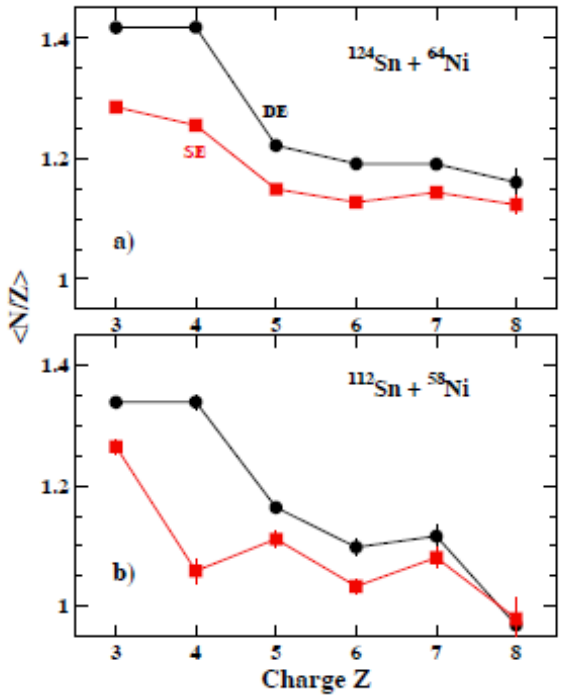

Figure 71: Isospin distributions as a function of the IMFs atomic number Z, for dynamical emission (DE) and statistical emission (SE), for the "neutron-rich" $^{124}Sn+^{64}Ni$ (panel a) and "neutron-poor" $^{112}Sn+^{58}Ni$ (panel b) systems at beam energy of 35 $AMeV$ [DEF14].

In the most recent phase of the data analysis of the CHIFAR experiment, some preliminary studies have focused on the investigation of phenomenon of the isospin transport, in order to correlate it with the symmetry energy in the asymmetric nuclear matter and characterize the EOS.

From the identification procedure, described in the Chapter 3, relating to the IMFs detected by the FARCOS correlator, some of the most abundant isotopes produced by the studied collisions were chosen: ^{4}He, ^{6}He, ^{6}Li, ^{7}Li, ^{8}Li, ^{7}Be, ^{9}Be, ^{10}Be, ^{10}B, ^{11}B, ^{12}C and ^{14}C. The N/Z distributions of some ratios of these selected isotopes were analyzed, as a function of the parallel velocity [ZAG25, ZAG25b]. The trends of the six nuclear reactions studied in the CHIFAR experiment, at the incident beam of $20\ AMeV$, were analyzed and compared each other, in order to observe the contribute of the isospin content for the three projectiles and as many targets. In particular, the N/Z distributions of the three main systems, namely the "neutron-rich" ^{124}Sn+^{64}Ni system, the "neutron-poor" ^{112}Sn+^{58}Ni system and the "isobaric" ^{124}Xe+^{64}Zn system, were initially compared (see Fig. 72, for the carbon isotopes yield ratio). Then, the trends of N/Z distributions were observed for the couples of the reactions with the same projectile, that means ^{124}Sn+^{64}Ni and ^{124}Sn+^{64}Zn (see Fig. 73), or ^{112}Sn+^{58}Ni and ^{112}Sn+^{64}Ni, or ^{124}Xe+^{64}Zn and ^{124}Xe+^{64}Ni; finally, the same targets were considered, ^{124}Sn+^{64}Ni, ^{112}Sn+^{64}Ni and ^{124}Xe+^{64}Ni (see Fig. 74), or ^{124}Sn+^{64}Zn and ^{124}Xe+^{64}Zn. For each combination and for each isotopic ratio, the results have shown that the N/Z distributions follow the isospin content of the colliding nuclei: the memory of the initial isospin conditions is preserved in the IMFs production in each studied reaction, according to the

respective isospin ratio already calculated and reported in the Table 1 of this thesis. The phenomenon of isospin migration can be highlighted in the distributions, as an effect of the neutron enrichment in the region of the mid-velocity. As far as we have understood the dynamical emission probability (DE) is favoured in the neutron-rich systems, both in the projectile and in the target, with respect to the statistical emission (SE). This behaviour can be correlated to the asy-stiff parametrization of the asymmetric nuclear matter. These results are very preliminary, because the event global variable detected by CHIMERA, the detector response and the experimental setup efficiency have not been included. Furthermore, the thresholds for the particles detected within the two DSSSDs of the FARCOS telescopes may not be perfectly optimized for the conditions inherent in the CHIMERA multi-detector. Future analyses will need to be developed with this in mind to obtain more qualitative results.

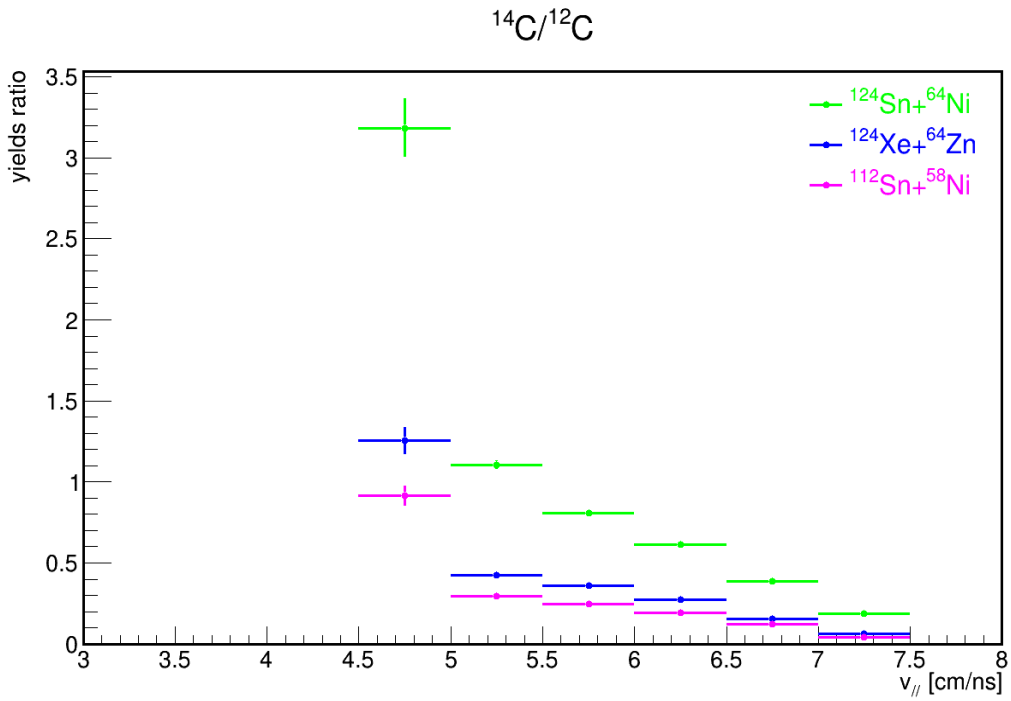

Figure 72: N/Z distributions for the carbon isotopes yiped ratio, as a function of the parallel velocity, compared for the "neutron-rich" $^{124}Sn+^{64}Ni$, the "neutron-poor" $^{112}Sn+^{58}Ni$ and the "isobaric" $^{124}Xe+^{64}Zn$ systems, at beam energy of 20 $AMeV$.

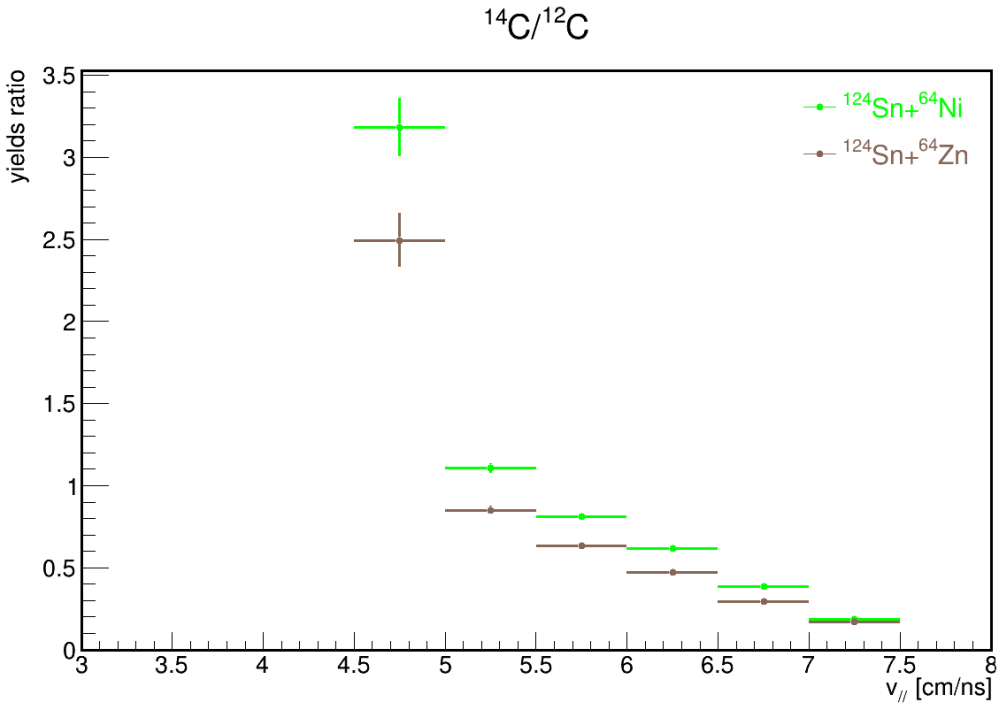

Figure 73: N/Z distributions for the carbon isotopes yiped ratio, as a function of the parallel velocity, compared for the "neutron-rich" $^{124}Sn+^{64}Ni$ and $^{124}Sn+^{64}Zn$ nuclear reactions of the CHIFAR experiment.

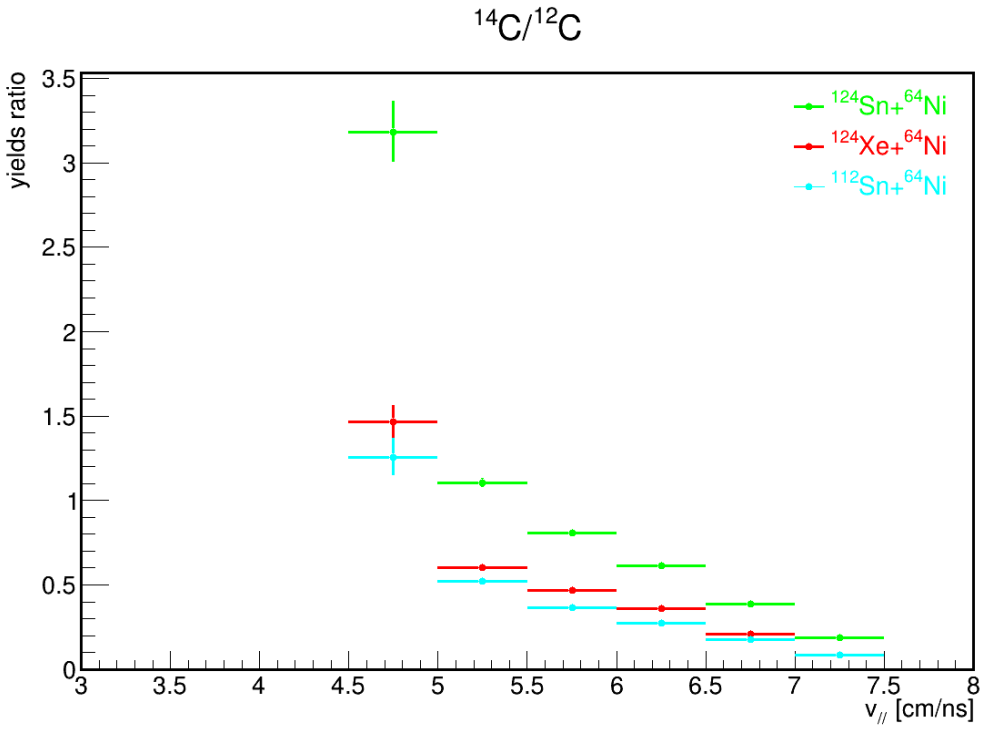

Figure 74: N/Z distributions for the carbon isotopes yiped ratio, as a function of the parallel velocity, compared for the "neutron-rich" $^{124}Sn+^{64}Ni$, $^{112}Sn+^{64}Ni$ and $^{124}Xe+^{64}Ni$ nuclear reactions of the CHIFAR experiment.

For each analysed reaction, the CHIMERA multi-detector permitted to reconstruct, event by event, the global variable in order to characterize the reaction process like the total kinetic energy, the charged particle multiplicity, the reaction plane, etc. CHIMERA is able to measure the particle variables in the event like its kinetic energy, its position in the laboratory reference frame (l.r.f) or in the center of mass reference frame (c.m.r.f) in principle for all particles at the end of the reaction. In order to better understand the reaction event, correlations among the global variables and the particle variables are often a useful tool, for example the correlation between the Total Kinetic Energy (*i.e.* $TKE = \sum_i E^i_{kin}$) and the polar deflection angle of the heavier detected fragment in the projectile-target center of mass system (*i.e.* $\theta_{c.m.}$). The two-dimensional distributions obtained for the "neutron-rich" $^{124}Sn+^{64}Ni$ and

"neutron-poor" ^{112}Sn+^{58}Ni systems, at incident beam energy of $20\ AMeV$, are shown in Figures 75 and 76. The distributions of the TKE as a function of $\theta_{c.m.}$ highlighted three different regions: the first one is characterized by the quasi-elastic emission, while the deep-inelastic mechanism is predominant in the second region, with the possible rupture of the PLF; finally, fission/fusion is the main process of the third region. In order, they are schematically individuated with a purple rectangle (denoted as "TKE1"), a blue rectangle ("TKE2") and an orange rectangle ("TKE3"). The respective ranges of the TKE and $\theta_{c.m.}$ variables will be useful to impose constraints in data analysis.

A preliminary study of the merger between the data collected by FARCOS and CHIMERA was conducted. The mass number distributions as a function of the parallel velocity were again studied, in order to confirm the high resolution of the FARCOS correlator in the region between the center-of-mass velocity and the beam velocity. Figure 77 shows the two-dimensional distribution obtained for "neutron-rich" ^{124}Sn+^{64}Ni system, from CHIMERA data, in colour scale, and from the events identified by FARCOS, as black dots: a good identification of the phase space can be observed up to $A \lesssim 35$.

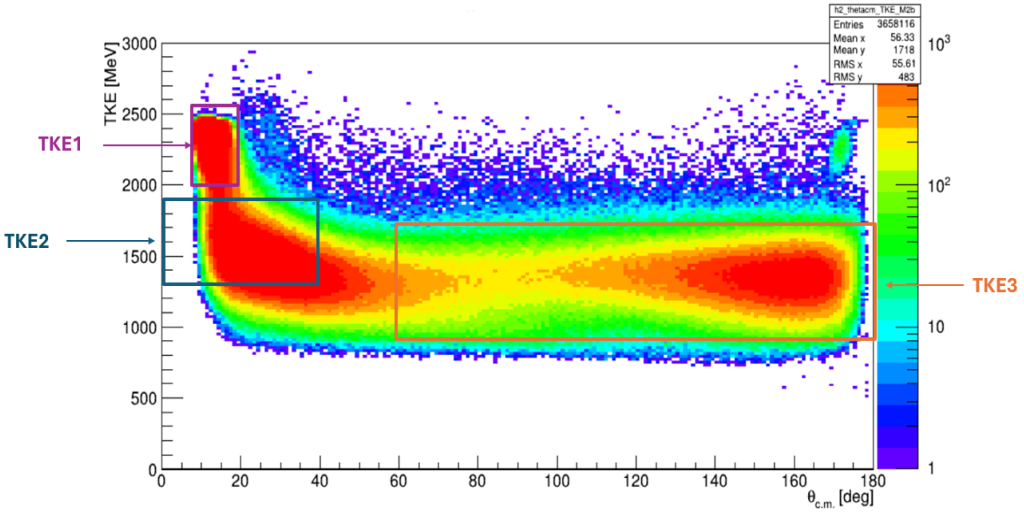

Figure 75: Correlation between the Total Kinetic Energy ($TKE = \sum_i E^i_{kin}$) and the polar deflection angle of the heavier detected fragment in the projectile-target center of mass system ($\theta_{c.m.}$), for the "neutron-rich" ^{124}Sn+^{64}Ni system at beam energy of 20 $AMeV$. The three different regions individuate the quasi-elastic emission (TKE1), the deep-inelastic mechanism (TKE2) and the fission/fusion process (TKE3).

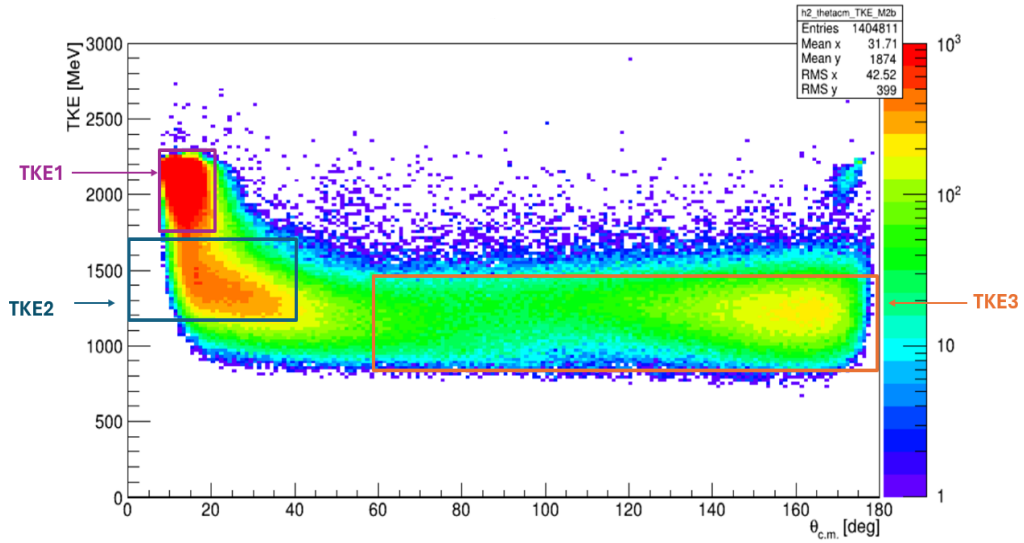

Figure 76: Correlation between the Total Kinetic Energy ($TKE = \sum_i E^i_{kin}$) and the polar deflection angle of the heavier detected fragment in the projectile-target center of mass system ($\theta_{c.m.}$), for the "neutron-rich" ^{112}Sn+^{58}Ni system at beam energy of 20 $AMeV$. The three different regions individuate the quasi-elastic emission (TKE1), the deep-inelastic mechanism (TKE2) and the fission/fusion process (TKE3).

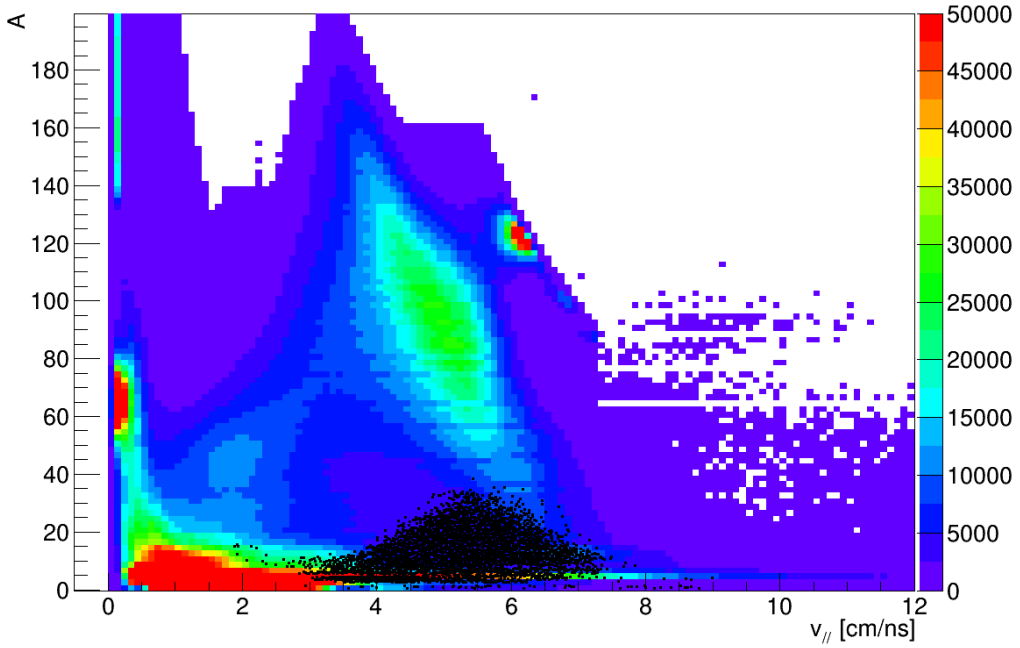

Figure 77: Mass number distribution as a function of the parallel velocity for the ions identified by using the CHIMERA multi-detector, in colour scale, and from the events identified by FARCOS, as black dots, for the "neutron-rich" $^{124}Sn+^{64}Ni$ system.

The merging of the data collected by both detection systems, FARCOS and CHIMERA, is fundamental for selecting the global variables, such as the total charged multiplicity, the impact parameter, the reaction plane, and so on: this will allow to characterize the reaction mechanism and the IMFs emission process. The data analysis will extend the study of the isospin role in HICs: the already discussed N/Z distributions for the identified isotopes will be filtered with specific constraints on thresholds, Total Kinetic Energy and global variables using the CHIMERA multi-detector. The effects of the IMFs dynamical emission and the phenomenon of the isospin migration will be better highlighted.

CHAPTER 5

The ASY-EOS II experiment @ GSI-FAIR.

The CHIMERA Collaboration focuses its research activities and perspectives on the characterization of the Equation Of State (EOS) of the nuclear matter, with the final aim to put new and more stringent constraints on the density dependence of the symmetry energy at supra-saturation densities. Thus, this last chapter of this thesis concerns the ASY-EOS II experiment, carried out at GSI-FAIR in March 2025 in Darmstadt, Germany [RUSprop, DEF25].

The ASY-EOS II experiment was proposed for studying the EOS of neutron rich matter at high baryon densities. Specifically, the main experimental goals were:

- The determination of the high-density behaviour of the symmetry energy; simultaneous measurements of the elliptic flow of neutrons, protons and light charged particles are the key observables. Experimentally, the elliptic flow allows to probe the EOS at densities up to around $2\rho_0$
- The knowledge of the density dependence of the symmetry energy; relevant information for astrophysical predictions of the mass-radius relationship of neutron stars can be extrapolated. Data analysis will provide more specific constraints on the slope parameter L and curvature parameter K_{sym} of the EOS
- The enforcement of tight constraints on nuclear transport theories.

The nuclear reactions investigated in the ASY-EOS II experiment were ^{197}Au+^{197}Au collisions, at four different energies,

$280\ AMeV$, $400\ AMeV$, $600\ AMeV$ and $1000\ AMeV$: an energy scan of this type can currently only be performed at the GSI-FAIR facility.

Heavy Ion Collisions, in fact in terrestrial laboratories, offer a unique opportunity to investigate the EOS of the nuclear matter, in a large range of baryonic densities. In general, it describes a relationship between density, pressure, energy, temperature and the isospin asymmetry [LI08]. The latter is expressed by the term $\delta = (\rho_n - \rho_p)/\rho$, where ρ_n, ρ_p and ρ are the densities of neutrons, protons and total nuclear matter, respectively. For the asymmetric nuclear matter, the EOS is expressed by the sum of two main components: the first one if the energy per nucleon of the symmetric nuclear matter, expressed by the term $E(\rho, \delta = 0)$; the second one is the asymmetric matter part, given by the product of the symmetry energy $E_{sym}(\rho)$ and the square of the isospin asymmetry δ^2. Thus, the total expression of the EOS can be explicated by the formula (10):

$$E(\rho, \delta) = E(\rho, \delta = 0) + E_{sym}(\rho)\delta^2 + o(\delta^4) \qquad (10)$$

Furthermore, the symmetry energy contribute can be expanded around the nuclear matter saturation density ρ_0, with the following expression:

$$E_{sym}(\rho) = E_{sym,0} + \frac{L}{3}\left(\frac{\rho-\rho_0}{\rho_0}\right) + \frac{K_{sym}}{18}\left(\frac{\rho-\rho_0}{\rho_0}\right)^2 + \cdots \qquad (11)$$

whit the following parameters involved:

- $E_{sym,0} \equiv E_{sym}(\rho = \rho_0) = S_0$: value of the symmetry energy at saturation density
- $L \equiv 3\rho_0 \frac{\partial E_{sym}(\rho)}{\partial \rho}\Big|_{\rho=\rho_0}$: slope parameter related to the neutron pressure

- $K_{sym} \equiv 9\rho_0^2 \frac{\partial^2 E_{sym}(\rho)}{\partial \rho^2}\Big|_{\rho=\rho_0}$: curvature parameter or symmetry compressibility.

Imposing more stringent constraints on the density dependence of the asymmetry term of the EOS is very important for many aspects. In fact, the $E_{sym}(\rho)$ contribute is relevant in the study of the nuclei masses, drip lines, collective excitations of neutron-rich nuclei, dynamics of HICs and particles flow, from Fermi to relativistic energies [HOR14, SOR24]. On the other hand, concerning astrophysical phenomena such as core-collapse supernovae and neutron stars, the high-density dependence of the symmetry energy is closely related to multi-messenger astronomy. Specifically, one of the key questions of neutron star physics concerns the determination of the mass-radius relationship of neutron stars, which is equivalent to a precise pressure-density correlation: the maximum mass of neutron star is correlated to the term $E(\rho, \delta = 0)$, while the radius is associated to the $E_{sym}(\rho)$ behaviour at high density, around $2\rho_0$ [FAT18]. Furthermore, other astrophysical observations regard mergers of compact binary stars and tidal deformability in gravitation wave events detected by LIGO/Virgo Collaboration [ABB18], and accurately measurements of neutron star radius by X-rays detection from spatial observatories such as NICER [RIL21-LEG21].

In the last two decades, astrophysical results and meaningful constraints for the nuclear EOS obtained by terrestrial laboratory experiments have been combined to improve the knowledge of the dense matter in neutron stars [TSA24, HUT22]. Many experimental observables in HICs have been studied according to their sensitivity

to the $E_{sym}(\rho)$ at supra-saturation densities, such as ratio of multiplicities or spectra of isospin partners (i.e. π^-/π^+, n/p or $t/^3He$), and the comparison of their flows. In particular, using relativistic HICs, the FOPI Collaboration [XIA09] and the SπRIT Collaboration [LYN22] have collected data on charged pion ratios; but also, the FOPI-LAND data [RUS11], the HADES data [ADA23] on collective flows and the ASY-EOS I data [RUS16] on the elliptic flows of neutron and hydrogen nuclei have probed the EOS of asymmetric matter.

At energies below $1.5\,AGeV$, the reaction dynamics is determined by the nuclear mean field. The pressure produces a collective motion of the compressed matter whose strength will be influenced by the E_{sym} in isospin-asymmetric systems. The strength of collective flows in HICs can be expressed with the Fourier expansion of the azimuthal distributions of particles with respect to the reaction plane, as a function of the particle rapidity y, as follows:

$$\frac{d\sigma(y)}{d\phi} \propto 1 + 2(v_1(y)cos\phi + v_2(y)cos2\phi \dots) \qquad (12)$$

The main observable v_2 is the so-called elliptic flow, related to protons, neutrons and composite charged particles; its value is negative around mid-rapidity at incident beam energies in the range of $0.2 - 5\,AGeV$: this means that matter is squeezed out perpendicular to the reaction plane and shows the strongest sensitivity to the EOS [LEF18]. The ASY-EOS I experiment, carried out at GSI-FAIR in 2011, investigated the isospin-dependent asymmetry component of the EOS at lower densities, around $1 - 1.4\,\rho_0$, using ^{197}Au+^{197}Au collisions at the beam energy of $400\,AMeV$. The robustness of the v_2 ratio observable as a probe of

the asymmetric contribute of the EOS were confirmed by the comparing of the experimental results with the UrQMD model predictions [RUS11]. In these calculations, the symmetry energy was parametrized according to the Fermi-gas model, as following:

$$E_{sym}(\rho) = E_{sym}^{pot}(\rho) + E_{sym}^{kin}(\rho) = 22\left(\frac{\rho}{\rho_0}\right)^{\gamma} + 12\left(\frac{\rho}{\rho_0}\right)^{2/3} MeV \quad (13)$$

with $\gamma = 0.5$ and $\gamma = 1.5$ corresponding to the soft and the stiff dependence of the nuclear matter, respectively. The prediction of the elliptic flow of neutrons and light charged particles emitted around mid-rapidity in Au+Au collisions were compared for the two choices of the stiffness of density dependence of the symmetry energy, as described in the formula (13). The ASY-EOS I experiment imposed tight constraints on the density dependence of the symmetry energy, with respect to the previous experiment, that means the FOPI-LAND data (left panel of Fig. 78). The elliptic flow ratio between neutrons and charged particles were studied as a function of the transverse momentum: experimental data were compared with the UrQMD calculations according to the stiff and soft parametrizations of the E_{sym} (right panel of Fig 78). The linear interpolation gave a final result of $\gamma = 0.75 \pm 0.10$, and $L = 72 \pm 13\ MeV$ for $E_{sym}(\rho_0) = 34\ MeV$ [RUS16].

The combined use of HIC and multi-messenger astronomy data enlighten the importance of the former mainly at $1.5\rho_0$. The stiffness of the EOS gave a value of radius of $12 \pm 0.78\ km$ for $1.4M_{\odot}$ neutron star mass, within 95% confidence level [HUT22, DEF25].

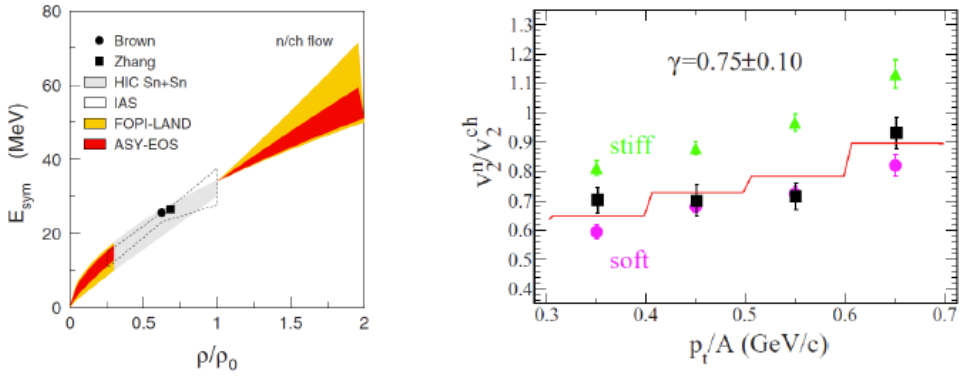

Figure 78: comparison of the constraints obtained for the density dependence of the symmetry energy between the ASY-EOS I (orange band) and the FOPI-LAND (yellow band) experiments (right panel); elliptic flow ratio between neutrons and charged particles as a function of the transverse momentum, for central Au+Au collisions at 400 $AMeV$: experimental data (black squares) were compared with the UrQMD calculations, employing a stiff (green triangles) and a soft (purple circles) density dependence of the symmetry energy; solid red line is the result of a linear interpolation [RUS16].

The ASY-EOS II experiment aimed to extend the knowledge of the symmetry energy to higher densities, close to $2\rho_0$, in a wide range of beam energies, from 280 $AMeV$ to 1000 $AMeV$, in order to improve the measurement precision and the values of the EOS parameters with respect to the previous ones. In fact, the measurement of the v_2^n/v_2^p and v_2^n/v_2^{ch} elliptic flow ratios will permit more effectively probing higher densities than previously done. By using higher beam energies, even higher densities can be probed, according to the model predictions. In fact, simulations of semi-central ^{197}Au+^{197}Au collisions, at different energies, from 250 $AMeV$ to 1000 $AMeV$, and for comparison neutron-rich systems such as ^{132}Sn+^{124}Sn, ^{124}Sn+^{124}Sn and Pb+Pb at 400 $AMeV$, 600 $AMeV$ and 800 $AMeV$ have been studied with the UrQMD transport model, as shown in the left panel of Fig. 79 [RUS16]. The difference of the two ratios between the stiff and soft parametrizations gives the sensitivity of the observable (right panel of Fig. 79). In particular, the sensitivity of the elliptic flow ratio of

neutrons over protons to the slope parameter L of the symmetry energy at saturation density in Au+Au collisions results highest at 400 $AMeV$ and decreases by a factor of ~2 as the incident energy is increased to 1000 $AMeV$.

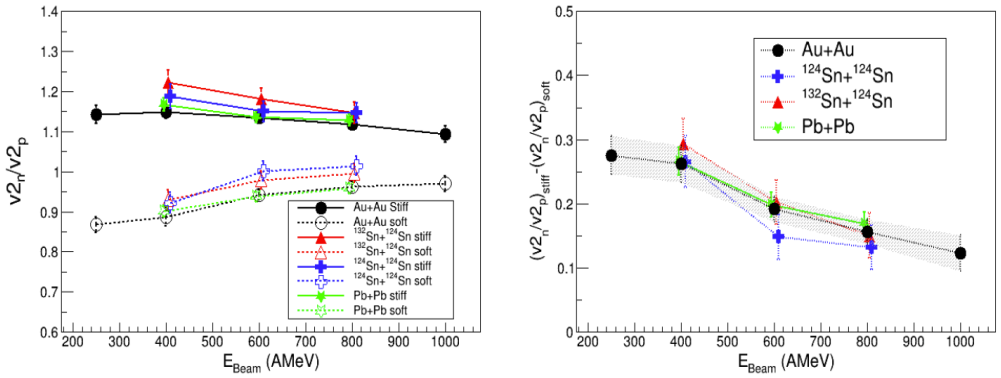

Figure 79: Excitation functions of neutrons over protons elliptic flow ratios (v_2^n/v_2^p), at mid-rapidity for semi-central Au+Au, ^{132}Sn+^{124}Sn, ^{124}Sn+^{124}Sn and Pb+Pb collisions, based on the UrQMD simulations, for stiff and soft density dependence of the symmetry energy (left panel); differences between the stiff and soft results (right panel) [RUS16].

The main goals of the ASY-EOS II experiment can be achieved thanks to the innovative and powerful detector ensemble, placed in Cave C at GSI-FAIR within the R^{3}B (Reactions with Relativistic Radioactive Beams) Collaboration. The experimental setup is sketched in Fig. 80, and involved the following detection systems:

- LOS (R^{3}B) start detector (not shown in Fig. 80): it is a plastic scintillator, placed in vacuum upstream of the target, gave the reference signal for the time-of-flight measurements and trigger. ROLU consists of four rectangular scintillators, each read out by a small PMT (Fig. 81)
- KRAB: it is a new detector, recently built at IFJ PAN in Krakow [LUK18], in order to provide a fast trigger signal based on the multiplicity threshold and charged particles azimuthal distributions for event-by-event reaction plane reconstruction. It allows to discriminate off-target reactions,

that means in air. The detector is constituted by 5 rings of $4 \times 4\ mm^2$ fast scintillating fibers readout by SiPMs, for a total of 736 channels, placed around the target (Fig. 82)

- 4 double-rings of CHIMERA (rings 3-6): about 400 CsI(Tl) scintillators that covered the polar angles between 7° and 20°; they allowed the measurement of charge and energy of forward emitter LCPs up to $Z{\sim}4$, the determination of the impact parameter and the reaction plane orientation of the events (Fig. 83)
- TOFD (R^3B): it is composed by two frames involved 4 planes with 44 scintillator bars ($1000 \times 27 \times 5\ mm^3$), for a total of 88 photomultipliers [HEI22]. The two frames have been separated. The first frame is used to measure the charge and the velocity of the charged particles emitted between 1° and about 5°, mainly projectile spectator-residues and their decay products; global variables for characterizing the collision centrality can be also extrapolated. The second frame is used as a veto for charged particles, in geometrical correspondence to the NeuLAND detector (Fig. 84)
- NeuLAND (R^3B): it gave a unique opportunity to measure neutrons and LCPs in the same angular region, with high efficiency [BOR21]. The calorimetric properties of the detector allow hydrogen isotopes well separated, so a good evaluation of the neutron vs. proton observables. Its highly granularity is guaranteed by 1300 individual submodules ($5 \times 5 \times 250\ cm^3$) arranged in 13 double planes, providing an active area of $250 \times 250\ cm^2$ and a total depth of 1.3 m. It

is placed around 5 m away from the target covering the mid-rapidity regions, that means the polar angles between 34° and 62° (Fig. 85).

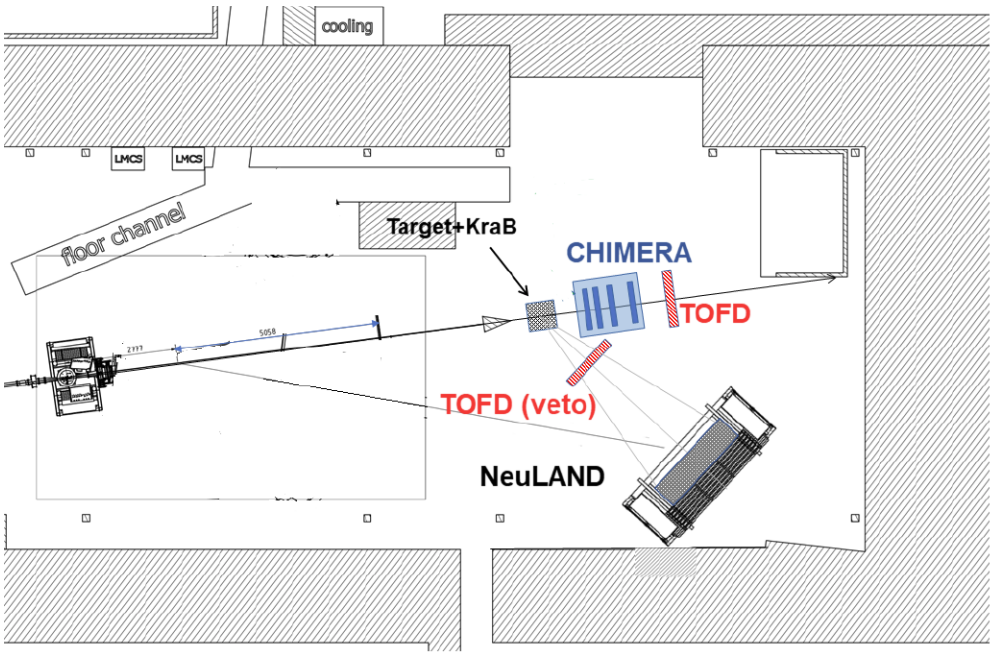

Figure 80: Schematic scale representation of the experimental setup used in the ASY-EOS II experiment, placed in Cave C at GSI-FAIR [RUSprop].

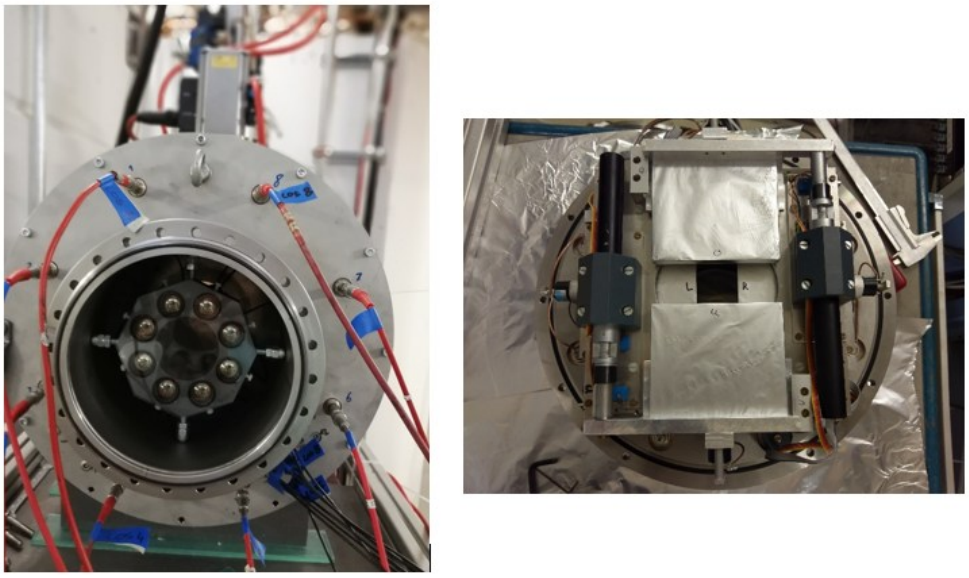

Figure 81: Photos of LOS (on the left) and ROLU (on the right) R^3B detectors.

Figure 82: Photo of KRAB.

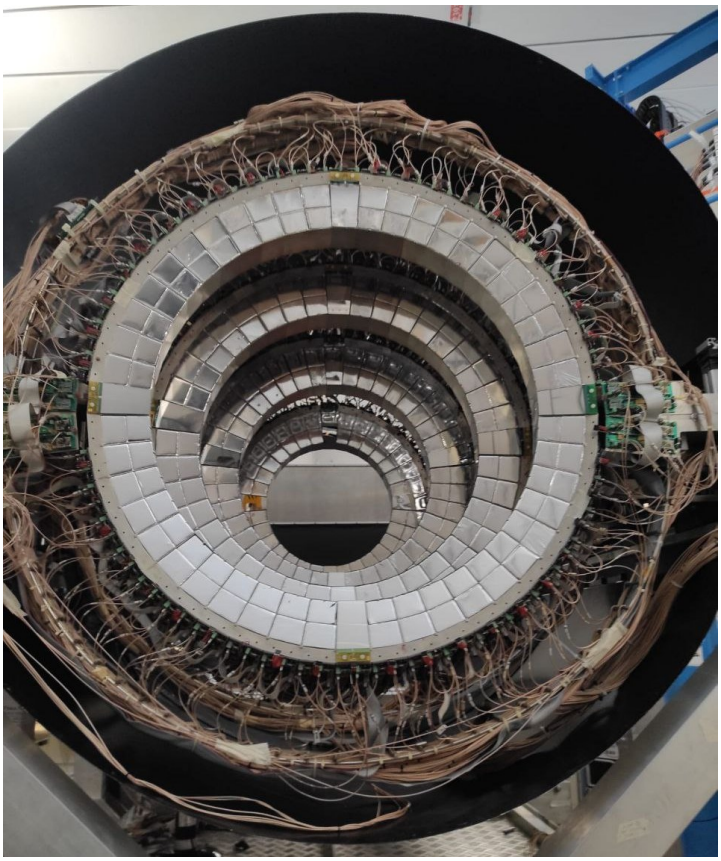

Figure 83: Photo of the 4 double-rings of CHIMERA.

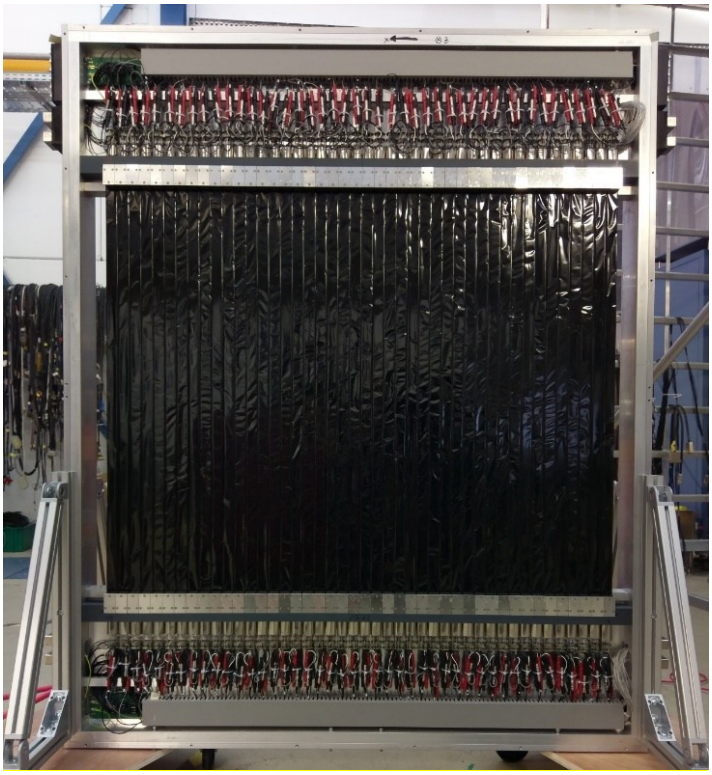

Figure 84: TOFD with HV and lemo cables while the front plate is open.

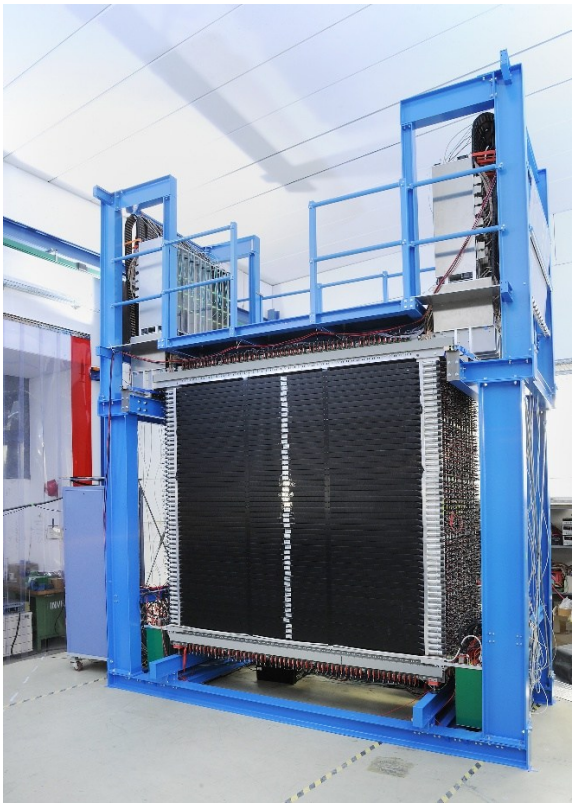

Figure 85: Photo of NeuLAND.

The four beam energies used in the ASY-EOS II experiment were chosen to satisfy several physics reasons. Indeed, the energy of $280\ AMeV$ is the lowest possible for the detector ensemble: this energy could ensure the highest sensitivity to the curvature parameter K_{sym} of the EOS. The $400\ AMeV$ is the energy already measured in the past ASY-EOS I experiment, so it is useful as a reference point for comparing old and new results. The slope parameter L of the EOS has shown its maximum sensitivity at $600\ AMeV$. Finally, the energy of $1000\ AMeV$ is the maximum achievable limit with this experimental setup, allowing to explore the highest densities where neutron/proton elliptic flow observable keeps a significant sensitivity (*i.e.* $\sim 15\%$) for the parametrization of the symmetry energy, according to the UrQMD simulations.

Figures 86-88 show some spectra acquired online during the ASY-EOS II experiment, for ^{197}Au+^{197}Au collision, at beam energy of $280\ AMeV$. In particular, during the data acquisition, attention was paid to the correlation between CHIMERA and KRAB, observing the multiplicity and the reaction plane: as expected, for the collisions with Au target (2%), the reaction plane shows a minimum at 0° and maximum at ±180° (see Fig. 86). The opposite trend is observed for off-target reactions. Regarding CHIMERA data acquisition, several variables have been checked, as the multiplicity, the fast and slow components, and their two-dimensional distributions. The online reconstruction of the reaction plane orientation by the CsI(Tl) scintillators of the 4 CHIMERA double-rings and the statistic of the acquired events are shown in Fig. 87. Finally, during each experimental run, the ratio between the fast and

slow components, as a function of the latter, for each CsI(Tl) scintillator, provided an online identification of the collision products, detected by CHIMERA, from protons up to $Z \lesssim 4$ (see Fig. 88).

The data analysis is currently underway; the results will be discussed in future publications of the CHIMERA Collaboration.

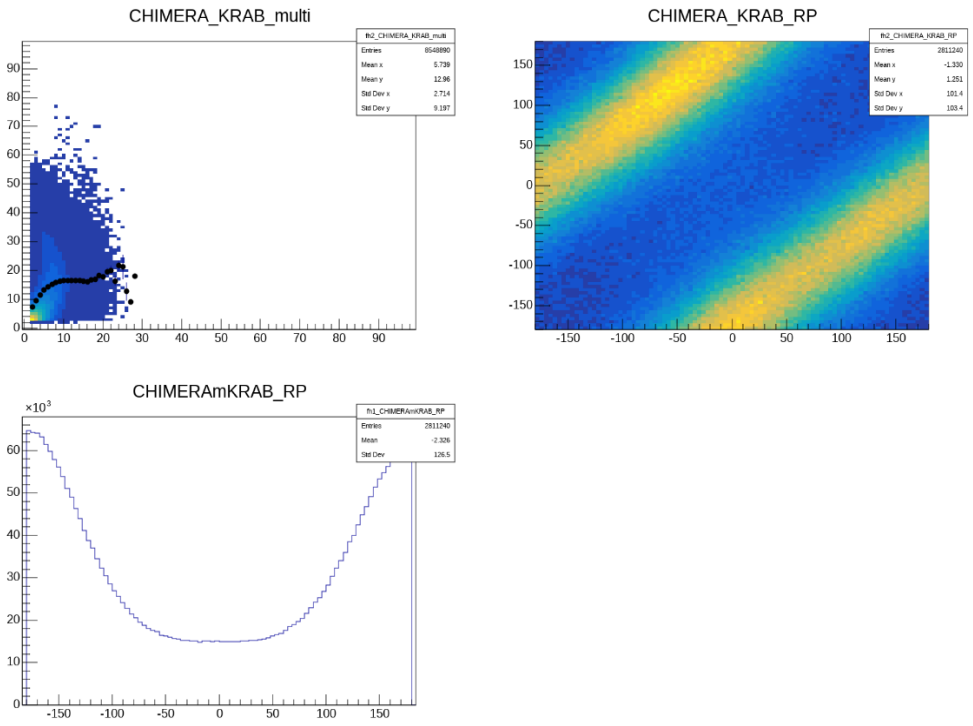

Figure 86: Some online spectra related to the plane reaction reconstructed by CHIMERA and KRAB, for ^{197}Au+^{197}Au collision, at beam energy of 280 $AMeV$, during the ASY-EOS II experiment.

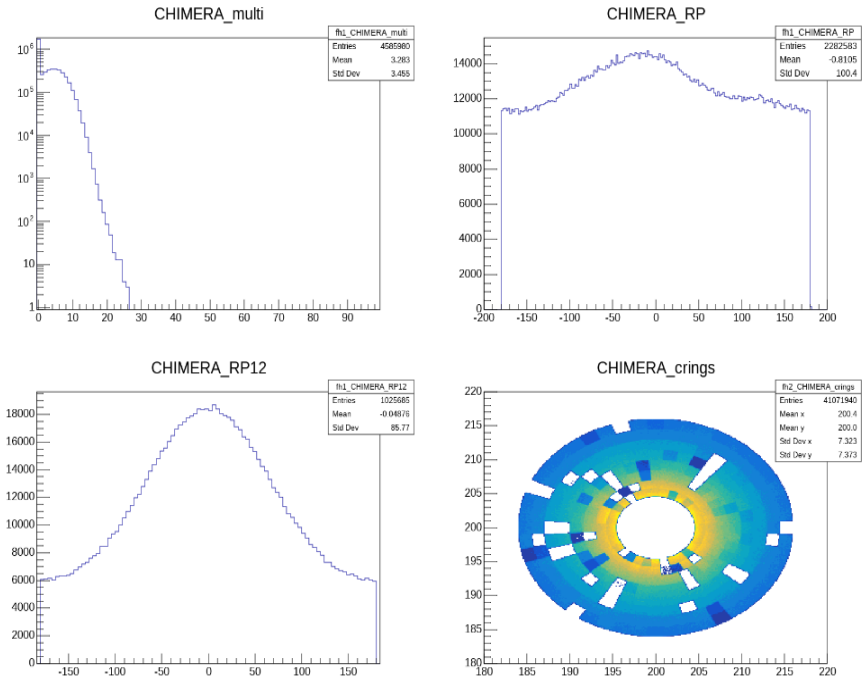

Figure 87: Some online spectra related to the CHIMERA rings acquisition, for ^{197}Au+^{197}Au collision, at beam energy of 280 $AMeV$, during the ASY-EOS II experiment.

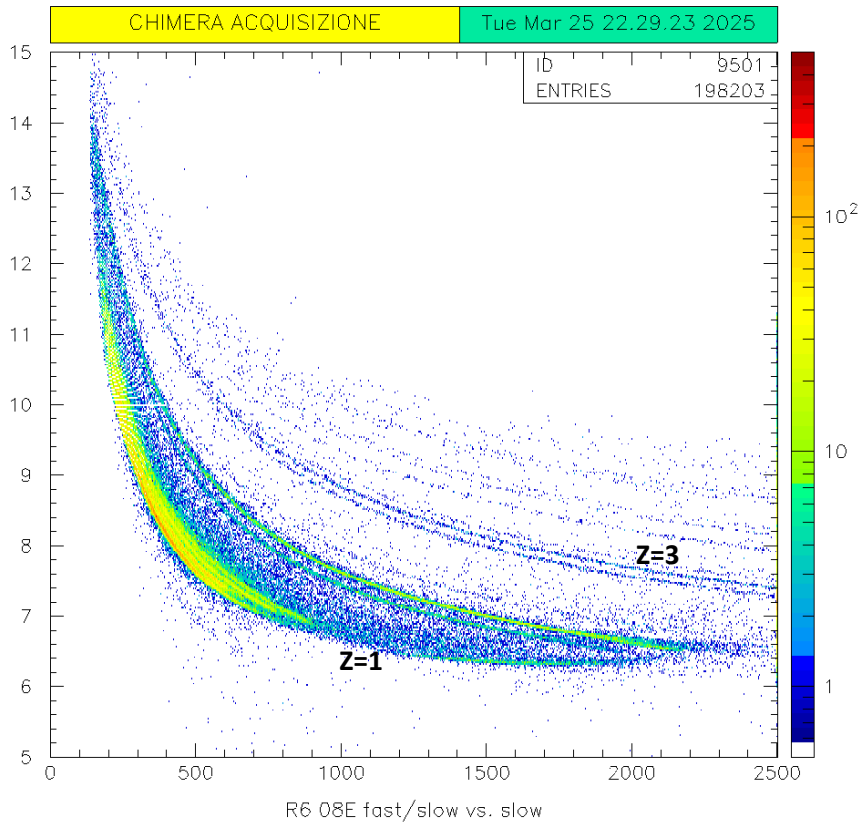

Figure 88: Online acquisition of the ratio fast/slow as a function of the slow component, related to one CsI(Tl) scintillator of CHIMERA, for ^{197}Au+^{197}Au collision, at beam energy of 280 $AMeV$, during the ASY-EOS II experiment.

CONCLUSIONS

The CHIFAR experiment was carried out at INFN-LNS to study the reaction mechanisms in the HICs at intermediate energy regime, the competition between dynamical and statistical IMFs emission process, in terms of their probabilities, and the influence of the isospin content of the colliding nuclei in non-central HICs. In fact, these phenomena are linked to the features of the Equation of State of the nuclear matter.

Previous experiments, conducted by the CHIMERA Collaboration, had already studied the nuclear interaction in the matter using HICs with a beam energy of $35\ AMeV$. The aim of the CHIFAR experiment was to extend the investigation to a lower energy regime, considering six nuclear reactions at the incident beam energy of $20\ AMeV$, by combining three beams – ^{124}Sn, ^{112}Sn and ^{124}Xe – and as many targets – ^{64}Ni, ^{58}Ni and ^{64}Zn. They are appropriately chosen in order to appreciate the difference between neutron-rich and neutron-poor systems.

The experimental setup, based on the coupling between the 4π CHIMERA multi-detector and ten telescopes of the FARCOS correlator, allowed to optimize the study of the correlations between IMFs and LCPs, as outcomes of the nuclear collisions, thanks to high performances of the two detectors.

The energy calibration of the two DSSSDs of each FARCOS telescope, based on the so called “punching through” technique, has been performed, and then the energy resolution of the front and back sides of the Si stages was evaluated. It is expressed in terms of the $FWHM$ and its decomposition into two contributes, the electronic

noise and the intrinsic factor of the detector. An energy resolution around 0.5% RMS (corresponding to 1.5 MeV at 300 MeV of peak) and around 1.6% RMS (corresponding to 4.8 MeV at 300 MeV of peak), respectively for the front side and for back one of the FARCOS telescopes, were achieved. Approximately 80% of the total error, that is around 1.5 MeV, was due to the electronic chain, *i.e.* the digitizer, the preamplifiers, and anything else coming from the experimental setup.

The so-called "pixelation technique" was implemented according to the experimental condition of the CHIFAR experiment. Some experimental constraints on the multiplicity, the deposited energy and the fired strips were initially imposed; then, a timing analysis, based on the detection time variable, was useful to exclude spurious coincidences and noise in the selected events. Finally, the method allowed to assign a unique spatial position to each detected particle by the DSSSDs, in terms of coordinates, namely the polar angle θ and the azimuthal angle ϕ. The angular coverage of each FARCOS telescopes was reconstructed, in a $\phi\ vs.\theta$ plane matrix, obtaining a polar coverage between 13°-30° in the laboratory frame system, and a total azimuthal coverage of 2π, according to the coupling of the ten FARCOS telescopes around the CHIMERA sphere.

Data analysis involved the identification of the IMFs detected by the FARCOS correlator. The ΔE-E technique was applied to the two DSSSDs of each telescope as interaction layers of the IMFs. Based on the Bethe-Bloch, the CHIMERA Collaboration has developed an identification algorithm, which provided a good identification in charge up to $Z \approx 16$; furthermore, an unambiguous

isotopic identification for IMFs with atomic number up to $Z \approx 9$ and atomic mass up to $A \approx 20$ was achieved. In the perspective of a future analysis, LCPs will be identified by specific methods applied to the data collected from the CsI(Tl) crystals.

Preliminary results about the isospin role in HICs at low energy beam was reported. Comparisons of mass distributions obtained from the IMFs identification phase permitted to highlight the effect of neutron enrichment, for the ^{124}Sn+^{64}Ni colliding system. Concerning the investigation of the dynamical emission process of the IMFs, from the distribution of the perpendicular velocity as a function of the parallel velocity, the emission of the IMFs resulted centred in the PLF velocity region, in the laboratory frame system, towards the mid-velocity. Some isotopes were chosen to study their N/Z distributions, as a function of the parallel velocity: the comparisons between the different reactions analyzed showed an effect of neutron enrichment, according to the respective isospin ratio of the projectile and the target. Furthermore, the IMFs isospin distribution seems to follow the initial isospin content of the colliding nuclei.

The merging of the data collected by FARCOS and CHIMERA was fundamental: the selection of the events with the constraints imposed by some global variables, such as total charged multiplicity, reaction plane, total kinetic energy of all particles emitted in the reaction, etc., are mandatory to characterize the reaction mechanism of the nuclear collisions. From the data collected by both CHIMERA and FARCOS, preliminary observations of the obtained distribution of the atomic mass as a function of the parallel velocity have confirmed the dynamical effects and the good identification of the phase space between $2 < Z < 16$ in the region between the center of

mass velocity and the beam velocity, thanks to the high resolution of the FARCOS correlator.

Preliminary results confirmed the trend already observed in the experimental results of the same reactions studied at higher bombarding energy of $35\ AMeV$. Anyway, future analyses should implement additional constraints on CHIMERA global variables, to filter the data based on the features of the experimental setup, which could lead to more accurate and qualitative results. The final objective of the research activity is to compare the experimental results with some theoretical models: to do this, high statistics are needed. The preliminary results suggest that a broader statistic could be needed. If confirmed, this is a good motivation for a PAC requirement for a new experiment, to study the neutron-rich and neutron-poor systems under better experimental conditions.

ACKNOWLEDGEMENTS

I would like to express my deepest gratitude to the people who made this doctoral journey possible.

Above all, I wish to thank my two outstanding supervisors for their invaluable guidance and support throughout this research, a journey that began with my undergraduate thesis and continued with my master's thesis.

Thanks to Professor Francesca Rizzo, for your intellectual guidance and for trusting my ability to pursue this complex topic. Your rigor, enthusiasm, and dedication to the Nuclear Physics have been a constant source of inspiration and have fundamentally shaped the quality of this dissertation. Your door was always open, and your advice was always constructive and encouraging.

I would like to thank Dr. Emanuele Vincenzo Pagano, for your technical expertise and meticulous attention to detail. Your timely feedback on the analysis of experimental data and your calm thoughtful approach have ensured the progress of this project, step by step, with rigor, renewing daily interest and enthusiasm.

My sincere thanks also go to those who provided crucial technical and analytical support. I am deeply grateful to Dr. Paolo Russotto, for his insightful contributions to the methodology and data interpretation in developing the custom scripts, and to Dr. Enrico De Filippo for his technical assistance in transforming raw data into meaningful results. Their constant availability to discuss challenging outcomes was greatly appreciated.

Finally, my sincere appreciation goes to Dr. Sara Pirrone and all the members of the CHIMERA Collaboration. Since my master's thesis, which continued with my doctoral project, the regular meetings have stimulated my thinking and have been essential to perfecting this research. Thank you for creating an intellectually stimulating, humanly respectful, and always supportive environment.

BIBLIOGRAPHY

[ABB18] B. P. Abbott *et al.*, Phys. Rev. Lett. **121**, 161101 (2018).

[ACO17] L. Acosta *et al.*, 2017 IEEE Nuclear Science Symposium (NSS) and Medical Imaging Conference (MIC), pp. 1– 4 (2017).

[ACO19] L. Acosta *et al.*, 2019 IEEE Nuclear Science Symposium (NSS) and Medical Imaging Conference (MIC), pp. 1– 4 (2019).

[ADA23] J. Adamczewski-Musch *et al.*, Eur. Phys. J. A. **59**, 80 (2023).

[ALD04] M. Alderighi *et al.*, Nucl. Phys. **A734**, E88-E91 (2004).

[ALD04b] M. Alderighi *et al.*, 2004 IEEE Nuclear Science Symposium (NSS) and Medical Imaging Conference (MIC), pp. 269–273 (2004).

[ALD05] M. Alderighi *et al*., IEEE Transactions on Nuclear Science, Vol. 52 (5), pp. 1624-1629, (2005).

[ALD06] M. Alderighi *et al.*, IEEE Transactions on Nuclear Science, Vol. 53 (1), pp. 279-285, (2006).

[AMO09] F. Amorini *et al.*, Phys. Rev. Lett. **102**, 112701 (2009).

[BAR04] V. Baran, M. Colonna and M. Di Toro, Nucl. Phys. **A730**, 329 (2004).

[BAR05] V. Baran *et al.*, Phys. Rev. C **72**, 064620 (2005).

[BOC00] F. Bocage *et al.*, Nucl. Phys. **A676**, 391 (2000).

[BOR21] K. Boretzsky *et al.*, Nucl. Instr. And Meth. A **1014**, 165701 (2021).

[BOR83] V. Borrel *et al.*, Z. Phys. A **314**, 191 (1983).

[BOW93] D. R. Bowman *et al.*, Phys. Rev. Lett. **70**, 3534 (1993).

[CAM15] P. Cammarata *et al.*, EPJ Web of Conferences **88**, 00019 (2015).

[CAR24] G. Cardella, N. S. Martorana *et al.*, Nucl. Instr. And Meth. A **1069**, 169961 (2024).

[CAR25] G. Cardella, N.S. Martorana *et al.*, Il Nuovo Cimento C **48**, 36 (2025).

[CAS18] A. Castoldi, C. Guazzoni, T. Parsani, Il Nuovo Cimento C **41**, 168 (2018).

[CHA05] R. J. Charity *et al.*, Phys. Rev. C **71**, 044602 (2005).

[COL03] J. Colin *et al.*, Phys. Rev. C **67**, 064603 (2003).

[COL93] M. Colonna *et al.*, Prop. Part. Nucl. Phys. **30**, 17 (1993).

[COL95] M. Colonna *et al.*, Nucl. Phys. A **589**, 160 (1995).

[DEF05] E. De Filippo *et al.*, Phys. Rev. C **71**, 064604 (2005).

[DEF05b] E. De Filippo *et al.*, Phys. Rev. C **71**, 044602 (2005).

[DEF12] E. De Filippo *et al.*, Phys. Rev. C **86**, 014610 (2012).

[DEF14] E. De Filippo and A. Pagano, Eur. Phys. J. A **50**, 32 (2014), and ref. therein.

[DEF16] E. De Filippo *et al.*, EPJ Web of Conf. **117**, 07017 (2016).

[DEF25] E. De Filippo *et al.*, Il Nuovo Cimento C **48**, 42 (2025).

[DEFprop] E. De Filippo, E. V. Pagano. P. Russotto *et al.*, Experimental Proposal of CHIFAR approved by the 2017 LNS-PAC.

[EVP16] E. V. Pagano *et al.*, EPJ Web of Conferences **117**, 10008 (2016).

[EVP22] E. V. Pagano *et al.*, Front. Phys. **10**, 1051058 (2022).

[FAT18] F. J. Fattoyev *et al.*, Phys. Rev. Lett. **120**, 172702 (2018).

[GLA83] P. Glässel *et al.*, Z. Phys. A **310**, 189 (1983).

[GOL99] F. Goldenbaum *et al.*, Phys. Rev. Lett. **82**, 5012 (1999).

[GUA20] C. Guazzoni and V. L. Sicari, 2020 IEEE Nuclear Science Symposium (NSS) and Medical Imaging Conference (MIC), pp. 1–4 (2020).

[GUA21] C. Guazzoni and V. L. Sicari, Il Nuovo Cimento C **44**, 49 (2021).

[GUE83] D. Guerreau *et al.*, Phys. Lett. **131B**, 293 (1983).

[GUE85] D. Guerreau, Nucl. Phys. A **447**, 37C (1985).

[HEI22] M. Heil *et al.*, Eur. Phys. J. A. **58**, 248 (2022).

[HIL92] D. Hilscher and H. Rossner, Ann. Phys. (Paris) **17**, 471 (1992).

[HOR14] C. J. Horowitz *et al.*, J. Phys. G.: Nucl. Part. Phys. **41**, 093001 (2014).

[HUT22] S. Huth *et al.*, Nature **606**, 276 (2022).

[KNO] G. F. Knoll, Radiation Detection and Measurement, John Wiley & Sons (3rd edition).

[LAC04] D. Lacroix *et al.*, Phys. Rev. C **69**, 054604 (2004).

[LEF18] A. Le Févre *et al.*, Phys. Rev. C **98**, 034901 (2018).

[LEG21] I. Legred *et al.*, Phys. Rev. D **104**, 063003 (2021).

[LEO87] W. R. Leo, Techniques for Nuclear and Particle Physics Experiment, Springer-Verlag (1987).

[LI08] B. A. Li *et al.*, Phys. Rep. **464**, 113 (2008).

[LISE] http://lise.nscl.msu.edu/lise.html

[LOM10] I. Lombardo *et al.*, Phys. Rev. C **82**, 014608 (2010).

[LOM11] I. Lombardo *et al.*, Nucl. Phys. B **215**, 272 (2011).

[LUK18] J. Łukasik, Il Nuovo Cimento C **41**, 182 (2018).

[LYN22] W. G. Lynch and M. B. Tsang, Phys. Lett. B **830**, 137098 (2022).

[LYN95] W. G. Lynch, Nucl. Phys. A **583**, 471-480 (1995).

[MAR20] T. Marchi *et al.*, Jour. Of Phys.: Conf. Ser. **1643** 012036 (2020).

[MAR22] N. S. Martorana *et al.*, Front. Phys. **10**, 1058419 (2022).

[MEN83] A. Menchaca-Rocha *et al.*, Phys. Lett. **131B**, 31 (1983).

[NAT81] J. B. Natowitz *et al.*, Phys. Rev. Lett. **47**, 1114 (1981).

[PAG01] A. Pagano *et al.*, Nucl. Phys. A **681**, 331c (2001).

[PAG04] A. Pagano *et al.*, Nucl. Phys. **A734**, 504 (2004).

[PAG12] A. Pagano *et al.*, Nucl. Phys. News **22**, 28 (2012).

[PAG12b] A. Pagano, EPJ Web of Conf. **31**, 00005 (2012).

[PAG20] A. Pagano *et al.*, Eur. Phys. J. A. **56**, 102 (2020).

[PAP01] M. Papa *et al.*, Phys. Rev. C **64**, 024612 (2001).

[PAP07] M. Papa *et al.*, Phys. Rev. C **75**, 054616 (2007).

[PIR11] S. Pirrone *et al.*, EPJ Web of Conf. **17**, 16010 (2011).

[POC95] J. Pochodzalla *et al.*, Phys. Rev. Lett. **75**, 1040 (1995).

[POL05] G. Politi *et al.*, IEEE Nuclear Science symposium Conference Record, Vol. 2, pp.1140-1144 (2005).

[POL12] E. Pollacco *et al.*, Phys. Procedia, **37**, 1799 (2012).

[POL18] E. C. Pollacco *et al.*, Nucl. Instr. And Meth. A **887**, 81 (2018).

[RAM84] F. Rami *et al.*, Z. Phys. A **318**, 239 (1984).

[RAM85] F. Rami *et al.*, Nucl. Phys. A **444**, 325 (1985).

[RIL21] T. E. Riley *et al.*, Astron. J. Lett. **918**, 27 (2021).

[RIS25] F. Risitano *et al.*, Il Nuovo Cimento C **48**, 54 (2025).

[RIZ14] C. Rizzo *et al*., Phys. Rev. C90, 054618 (2014).

[RUS10] P. Russotto *et al.*, Phys. Rev. C **81**, 064605 (2010).

[RUS11] P. Russotto *et al.*, Phys. Lett. B **697**, 471 (2011).

[RUS14] P. Russotto *et al.*, Jour. Of Phys.: Conf. Ser. **515** 012020 (2014).

[RUS15] P. Russotto *et al.*, Phys. Rev. C **91**, 014610 (2015).

[RUS16] P. Russotto *et al.*, Phys. Rev. C **94**, 034608 (2016).

[RUS20] P. Russotto *et al.*, Eur. Phys. J. A. **56**, 12 (2020).

[RUS23] P. Russotto *et al.*, Nucl. Instr. And Meth. A **1056**, 168593 (2023).

[RUSprop] A. Le Fèvre, J. Łukasik, P. Russotto, Experimental Proposal of ASY-EOS II (G-22-00122) approved by the 2022 GSI G-PAC.

[SAC25] G. Saccà *et al.*, Il Nuovo Cimento C **48**, 74 (2025).

[SAN95] T. C. Sangster *et al.*, Phys. Rev. C **51**, 1280 (1995).

[SCO83] D.K. Scott, Nucl. Phys. A **409**, 291C (1983).

[SOR24] A. Sorensen *et al.*, Progr. Part. Nucl. Phys. **134**, 104080 (2024).

[SOU90] R. T. De Souza *et al.*, NIM A **295**, 109 (1990).

[STA96] P. Staszel *et al.*, Phys. Lett. B **368**, 26-31 (1996).

[STE95] A. A. Stefanini *et al.*, Z. Phys. A **351**, 167 (1995).

[TSA24] C. Y. Tsang *et al.*, Nat. Astron. **8**, 328 (2024).

[VAN73] R. Vandenbosh and J. R. Huizenga, Nuclear Fission (Academic Press, New York, 1973).

[VIO85] V. E. Viola , V. E. Viola, K. Kwiatkowski, and M. Walker, Phys. Rev. C **31**, 1550 (1985).

[WAT16] A. Watts *et al.*, Rev. Mod. Phys. **88**, 021001 (2016).

[webCHI] https://web.infn.it/CHIMERA/index.php/it/rivelatori.

[WIL10] J. Wilczyński *et al.*, Phys. Rev. C **81**, 024605 (2010).

[XIA09] Z. Xiao, B. A. Li *et al.*, Phys. Rev. Lett. **102**, 062502 (2009).

[ZAG24] C. Zagami *et al.*, Il Nuovo Cimento C **47**, 62 (2024).

[ZAG25] C. Zagami, Il Nuovo Cimento C **48**, 165 (2025).

[ZAG25b] C. Zagami *et al.*, Il Nuovo Cimento C **48**, 49 (2025).

[ZAG25c] C. Zagami *et al.*, Il Nuovo Cimento C **48**, 35 (2025).